Computational Methods and Measurements for Direct and Inverse Scattering of Microwaves

Wingren, Niklas

2024

Document Version:
Publisher's PDF, also known as Version of record

[Link to publication](#)

Citation for published version (APA):
Wingren, N. (2024). *Computational Methods and Measurements for Direct and Inverse Scattering of Microwaves*. Department of Electrical and Information Technology, Lund University.

Total number of authors:
1

Computational Methods and Measurements for Direct and Inverse Scattering of Microwaves

Niklas Wingren

Doctoral Dissertation

Lund University
Lund, Sweden
2024

DON'T PANIC

Abstract

Electromagnetic waves are widely used in society today for a multitude of applications. Design of electromagnetic devices and applications requires accurate methods for evaluating performance, which often means modern computational methods. While these methods have seen tremendous development in recent decades, it is still very important to perform measurements to validate the performance of devices and software. This dissertation contains work on the computational side as well as validating measurements.

The dissertation consists of two parts. Part I is an introduction to the subject, and Part II consists of five scientific papers. The introduction gives an overview of the topics which are important for understanding the scientific papers of Part II and puts the research in a wider context. Of the scientific papers in Part II, two are published in peer-reviewed international journals, one is accepted for publication, and two are under review.

The problem of electromagnetic scattering has long been important in radar, where it is the mechanism for detection. This is often called the direct scattering problem, where a known object is illuminated by an incident wave and the scattered wave is computed. In Paper I, a computational code implementing the finite element-boundary integral method is presented. The code, which is publicly available at https://www.github.com/nwingren/fe2ms, was developed using open-source software to accelerate the development process. While this code is verified in Paper I, there were no comparisons to measurements. In Paper II, a complete design process was performed using the code from Paper I, with manufacturing using 3D printing and measurements of the performance to validate the computations. This acted both as a demonstration of using the code practically, and as a validation. One advantage of the finite element-boundary integral method used in the code is that problems with highly complex media can be solved. This was utilized in Paper III where characteristic modes were computed for a an inhomogeneous, bianisotropic, and nonreciprocal object.

A different problem is that of inverse scattering, for which the scattered wave is known but the object or incident wave is unknown. This is a more complicated problem which requires the modern computational methods available today, and can be used to discern properties of an object, for example for nondestructive testing. In Paper IV, a method for nondestructive testing of singly curved composite panels using millimeter waves is presented together with measurements of real panels. The method is based on computational electromagnetics and was designed specifically for detection of sparsely distributed flaws in such panels. Microwaves and millimeter waves are relatively new in nondestructive testing compared to other methods like ultrasound. One possible development would be to combine the new and the old by utilizing interaction between acoustic and electromagnetic waves. As a way to demonstrate that this might be possible, microwaves scattered by ultrasound were measured in Paper V in air, where the interaction would be much weaker than in nondestructive testing settings.

Populärvetenskaplig sammanfattning

Elektromagnetiska vågor och deras tillämpningar utgör en viktig del av våra liv även om många av oss kanske inte tänker på det. Våra mobiltelefoner innehåller ett stort antal antenner för att kunna koppla upp sig mot internet, hitta vår position via GPS eller spela upp musik via Bluetooth. Vi använder en antenn inuti vårt bankkort när vi ska betala trådlöst, och våra bilar håller ständig uppsikt för hinder med inbyggda radarsensorer. En viktig förutsättning för denna utveckling är de verktyg för elektromagnetiska beräkningar som är tillgängliga för dagens ingenjörer.

En huvuddel av avhandlingen täcker just elektromagnetiska beräkningar. Utvecklingen av nya tillämpningar inom elektromagnetismen ställer höga krav på en motsvarande utveckling av verktyg som används vid beräkningar för nya system. Ingenjörer som designar nya system använder sig främst av kommersiella datorprogram, men dessa bygger i sin tur på nya metoder från akademisk forskning. Metoden för elektromagnetiska beräkningar jag använt mig av lämpar sig vid problem med komplicerade materialstrukturer. Mitt arbete har fokuserat på öppen källkod, vilket innebär att datorprogram görs fritt tillgängliga för andra att använda och modifiera. Då jag använt andras program som byggblock har utvecklingen av mitt program kunnat accelereras, och jag hoppas att andra kan få liknande hjälp av mitt arbete. Utöver att jag har utvecklat ett öppet tillgängligt beräkningsprogram har jag även visat hur det kan användas för olika typer av beräkningsproblem. I ett av dessa har jag kunnat använda mitt beräkningsprogram för att designa en ny typ av elektromagnetisk struktur där en prototyp senare uppmättes med god överenstämmelse. Programmet har även kunnat användas för en ny typ av teoretisk beräkning som kommersiella datorprogram inte klarar av.

En annan del av avhandlingen handlar om tillämpningar inom avbildning för industriell produktion. Utvecklingen av exempelvis trådlös kommunikation har gjort att tekniken som används blivit billigare och mer kraftfull. Detta är något som öppnar möjligheter att använda tekniken inom områden som inte tidigare varit praktiska. Ett exempel är att vi idag effektivt kan använda mikrovågor för att avbilda föremål på sätt som inte vanligt ljus kan göra. Detta sker på stor skala i säkerhetskontroller på flygplatser, men stora möjligheter finns även inom bland annat industriell kvalitetskontroll och medicinsk avbildning. Som del av den här avhandlingen har jag arbetat med avbildning med mikrovågor för att kunna utföra oförstörande provning av kompositmaterial som används i flygplan. Oförstörande provning är ett samlingsnamn för olika metoder som används för att hitta defekter i en produkt utan att påverka dess funktion. Detta är viktigt inom många olika industrier, men särskilt inom flygindustrin är oförstörande provning en nödvändighet för alla strukturella delar. Ofta används ultraljud för detta, men mikrovågor är känsliga för andra typer av defekter och kan därför vara av intresse. Tidigare metoder utvecklade i samma forskargrupp fokuserade på plana paneler, men jag utvecklade metoden till att även kunna användas på

krökta paneler. I flygplan är många ytor krökta för att få till rätt aerodynamik och därför är detta ett viktigt steg.

Då ultraljud används ofta inom oförstörande provning är det nära till hands att försöka kombinera ultraljud med mikrovågor och dra nytta av båda metodernas fördelar. Växelverkan mellan elektromagnetiska vågor och akustiska vågor har undersökts tidigare, men inte för de våglängder som är aktuella inom oförstörande provning. För att undersöka hur väl det skulle fungera testade jag att mäta detta, men i luft i stället för typiska material för flygplan. Detta gjorde det möjligt för mig att mäta växelverkan i vår labbmiljö med befintlig utrustning. Växelverkan i luft är väldigt svag, men jag lyckades trots det detektera växelverkan mellan de två typerna av vågor. Detta bådar gott för mätningar i andra material än luft där effekten väntas vara starkare.

Preface

This dissertation summarizes the research I have carried out at the Department of Electrical and Information Technology, Lund University, Sweden. The dissertation starts with a research overview followed by the scientific papers as listed below. The papers are not ordered chronologically, but rather according to their general topics.

List of Included Papers

I. N. Wingren and D. Sjöberg, "Using Open Source to Accelerate Development of a Finite Element-Boundary Integral Code," *IEEE Open Journal of Antennas and Propagation*, 2024, accepted.

   Contributions of the author: I developed the computational software, performed the numerical tests and wrote the paper.

II. N. Wingren and D. Sjöberg, "Demonstrating Reconfigurability in Water-based Electromagnetic Devices using a 3D-printed Siphon," *Microwave and Optical Technology Letters*, 2024, submitted.

   Contributions of the author: I designed and manufactured the device, performed the numerical simulations and measurements, processed the data and wrote the paper.

III. N. Wingren, D. Sjöberg, M. Gustafsson, J. Lundgren, M. Capec, L. Jelinek, and K. Schab, "Characteristic Modes of Nonreciprocal Systems," *IEEE Antennas and Wireless Propagation Letters*, 2023, submitted.

   Contributions of the author: I performed the numerical simulations of the third example, analyzed the corresponding data and wrote parts of the paper.

IV. N. Wingren and D. Sjöberg, "Nondestructive Testing Using mm-Wave Sparse Imaging Verified for Singly Curved Composite Panels," *IEEE Transactions on Antennas and Propagation*, Vol. 71, No. 1, pp. 1185–1189, 2022.

   Contributions of the author: I extended the algorithm to singly curved structures, performed the measurements, post-processed the data and wrote the paper.

V. N. Wingren and D. Sjöberg, "Measurements of microwave scattering by ultrasound in air at oblique incidence," *Europhysics Letters*, Vol. 131, No. 5, 2020.

   Contributions of the author: I designed the experimental setup, performed the measurements and wrote the paper.

Other Scientific Work by the Author

The author of this dissertation is also the author or co-author of the following publications and scientific work which are related to but not considered part of the dissertation:

VI. N. Wingren and D. Sjöberg "Simulating Magnetized Plasma using an Accelerated Finite Element-Boundary Integral Code" *XXXVth URSI General Assembly and Scientific Symposium (URSI GASS),* Sapporo, Japan, 2023.

VII. N. Wingren and D. Sjöberg "An Accelerated Finite Element-Boundary Integral Code Developed using Open Source Software" *Swedish Microwave Days,* Stockholm, Sweden, 2023.

VIII. N. Wingren and D. Sjöberg "Investigating Low-Rank Approximations for the Finite Element-Boundary Integral Method" *17th European Conference on Antennas and Propagation (EuCAP),* Florence, Italy, 2023.

IX. N. Wingren and D. Sjöberg "Finite Element-Boundary Integral Simulation of Icing Effects on a Marine Radar Reflector" *3rd URSI Atlantic and Asia Pacific Radio Science Meeting (AT-AP-RASC),* Gran Canaria, Spain, 2022.

X. N. Wingren, D. Sjöberg, and M. Gustafsson "Conformal Sparse Image Reconstruction on Singly Curved Surfaces" *15th European Conference on Antennas and Propagation (EuCAP),* Düsseldorf, Germany, 2021.

XI. N. Wingren and D. Sjöberg, "Analytical Modeling and Multiphysics Simulation of Acousto-Electromagnetic Interaction" *14th European Conference on Antennas and Propagation (EuCAP),* Copenhagen, Denmark, 2020.

Acknowledgments

First, I would like to thank my main supervisor Daniel Sjöberg for guiding me throughout my PhD studies. When I started my master's thesis you were a great supervisor, and this played an important role in my decisions as we started discussing possible PhD studies. Even during the initial time when you were head of department, you would always find time for discussion regardless of how many meetings were in your calendar. I would also like to thank my assistant supervisor Mats Gustafsson. There are many times I have walked into your office with a problem and left with a new perspective and a clear path forward. To have two supervisors who make themselves available for discussions and who are as supporting as you are has been invaluable as a PhD student.

As the projects I have worked in during my studies have been collaborations with industrial partners, there are people who have helped me from the industrial side of things. Tomas Lundin, Torleif Martin, Christer Larsson, and Erik Söderström have all been involved in my two main projects and have helped me understand questions and problems from the industrial perspective.

I would like to thank my predecessor in the EKAS 2 project, Jakob Helander, for handing over your code to me and helping me understand it in the beginning of my studies. I would also like to thank Johan Lundgren for introducing me to mm-wave near-field scanning, and for being my co-assistant in teaching many courses. This includes the ever exciting task of grading lab reports, which I also thank Ben Nel for sharing with me. Another thank you goes to Zhongyunshen Zhu who, together with Mats, Ben, and me, shared the confusing experience of figuring out remote teaching in March 2020. There are also many people who I may not have worked much with, but who still have made the office a nice place to be. So thank you Casimir, Alexandros, Anton, Abinaya, Heera, Saketh, Navya, Gautham, Patrik, Robin, Marcus, Hannes, Philipp, Anette, Louise, André, Duc, Karthik, Paula, Lars-Erik, Lars, Erik, Mattias, and Johannes.

I want to thank my friends who have made the time as a PhD student easier by giving me time *not* to be a PhD student. I hope that the progress I have made in the research field of "building airplanes" is clear in this dissertation! Finally, I would like to thank my family who have always supported me and who have made this journey possible.

Lund, March 2024
Niklas Wingren

Acronyms and Abbreviations

2G	second generation of cellular networks
5G	fifth generation of cellular networks
6G	sixth generation of cellular networks
ACA	adaptive cross approximaiton
AIM	adaptive integral method
API	application programming interface
BI	boundary integral
BSD	Berkeley software distribution
CAD	computer-aided design
CEM	computational electromagnetics
CFIE	combined field integral equation
COCOMO	constructive cost model
DUT	device under test
DFT	discrete Fourier transform
EDUT	example device under test
EFIE	electric field integral equation
EM	electromagnetic
EPS	expanded polystyrene
FDTD	finite-difference time-domain
FE	finite element
FEM	finite element method
FFCx	FEniCSx form compiler
FFT	fast Fourier transform
GPL	general purpose license
HEM	hybrid electromagnetic
IF	intermediate frequency
JIT	just-in-time

MFIE	magnetic field integral equation
MLFMA	multilevel fast multipole algorithm
mm-wave	millimeter wave
MoM	method of moments
NDT	nondestructive testing
NEC	numerical electromagnetic code
PDE	partial differential equation
PEC	perfect electric conductor
PET	polyethylene terephthalate
PETG	polyethylene terephthalate glycol
PMC	perfect magnetic conductor
PML	perfectly matched layer
RCS	radar cross section
RWG	Rao-Wilton-Glisson
RASS	radio acoustic sounding system
Rx	receive
SAR	synthetic aperture radar
SLOC	source lines of code
SNR	signal-to-noise ratio
SVD	singular value decomposition
STL	stereolithography
TE	transverse electric
TM	transverse magnetic
Tx	transmit
UFL	unified form language

Contents

Part I: Introduction and Research Overview

1   Background and Motivation

Electromagnetic waves are widely used in all areas of modern society. Broadcasting like radio, terrestrial television and satellite television have been part of society for a long time, with radio broadcasting being widely available in many parts of the world a century ago [153]. In recent decades, however, other types of wireless communications have changed our world profoundly. While various analog forms of mobile communication technologies had been available earlier, the release of the digital second generation of cellular networks (2G) in 1991 [6] made wireless communications widely available and adopted by the public. Development since then has been rapid with the latest release being 5G in 2019 [164], and 6G currently under development [164]. During the same time, other wireless communication technologies like WiFi and Bluetooth have been developed as well, and today we find all these technologies neatly packaged in small cell phones together with other wireless technologies like satellite navigation and near-field communication. All these require antennas, and the design of these hidden away in a small package is not an easy task. One major reason why it is even possible to design a smartphone with all its electromagnetic capability is the use of modern electromagnetic computations [153].

Another application of electromagnetic waves is radar and remote sensing. Radar is originally an acronym for radio detection and ranging, and this essentially describes the technology which uses electromagnetic waves to determine position, velocity and possibly other properties of objects remotely. The first large-scale development of radar was for military applications before and during World War II [78, 153]. For much of the time since then, radar has been widely applied in various military systems as well as in aviation, meteorological, and marine applications [115]. However, with the rise of wireless communication since the 1990s, radio-frequency hardware has seen much technical development and as a consequence it became cheaper and more energy efficient. As radar uses similar hardware, the civilian applications of radar have become much more numerous with radar today being used widely in automotive applications [155], civilian surveillance [9], and low-cost, low-power sensors [1, 67, 140]. An example of a low-cost, low-power radar sensor is the Acconeer A121 sensor shown in Figure 1. Radar is widely used in the field of remote sensing to determine properties of an environment and produce large scale images of certain properties. This includes monitoring of various environmental properties of our planet using satellite-based radar system, which is an application that has become very important in Earth and climate science [12, 114]. Such a satellite-based radar system is seen in Figure 1. It has a very different size compared to the small Acconeer sensor, showing how radar systems can be useful at different scales. In most radar applications, it is important to understand how different targets react to illumination by electromagnetic waves from the radar transmitter. This is a complex task as this response can only be analytically computed for a few special geometries. It is possible to use various approximations, but for high-fidelity re-
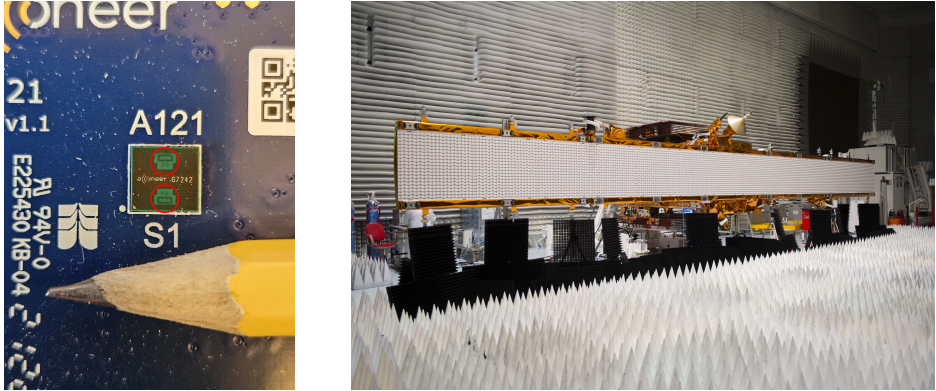
Figure 1: Two examples of radar systems. Left: Acconeer A121 radar sensor mounted on a circuit board with transmitting and receiving antennas encircled in red. Right: Sentinel-1A radar imaging satellite seen with its large radar antenna facing the camera (Photo: ©ESA–S. Corvaja, 2014).

sults it is necessary to use electromagnetic computations. Much of the efforts in electromagnetic computations have been in search of lowering the response of an object to radar in, for example, stealth aircraft [71, 78, 153]. These applications can set very high demands on the capability of the computational methods used, and many advances in such methods and software can be related back to uses in military applications. For example, an early computational code called the numerical electromagnetic code (NEC) was developed primarily to solve problems for the US air force and navy, but also laid much of the groundwork for development of methods and software which is widely used today in all electromagnetic applications [24, 25].

Electromagnetic computations have now been mentioned as an important enabling tool for our modern use of electromagnetic waves, and there is an interest in its continued development to support the general development in electromagnetics. In all fields of engineering, it is crucial to be able to compute and predict the capabilities of a designed object before manufacturing it. In some cases, this can be done analytically and that was the way most engineering was done before modern computers. For electromagnetics, there are generally few problems that can be solved analytically, and this limited engineering designs for much of the time since the first applications of electromagnetic waves in the early 1900s [153]. With the advent of computers, however, new types of methods using numerical computations became possible. This is a development seen in most areas of engineering, and many of the methods which are used in electromagnetics have their origin in methods used in other areas of physics. This is understandable since the methods themselves solve mathematical equations, and these equations are not necessarily tied to any particular branch of physics. The most accurate numerical methods used in electromagnetics are typically based on reformulating the basic equations of Maxwell's equations to other equations which are suit-

able for numerical solution, often categorized as differential equations or integral equations [35]. These two types of equations lead to different characteristics of the numerical methods, and in this dissertation methods from both types of equations are used. While the improved performance of computers was a large part of why numerical methods became popular, improvements of the numerical methods themselves have certainly played a role. The way that the numerical cost of popular methods scale with larger problem sizes means that increased computational power might not give much improvement in actual performance of a method. With development of algorithms to reduce this scaling of numerical cost, often referred to as acceleration or compression methods, the usefulness of computational methods in electromagnetics has been improved [35, 71].

With this great applicability of electromagnetic computations, it is important to consider the way methods are implemented. In most user settings, commercial software packages for computations are used. This is not strange, as such software is typically easy to use, well-tested, and optimized in its performance [35]. For academic research into the methods themselves, on the other hand, the use of such software is not ideal since it is generally not possible to modify. Instead, researchers develop the software themselves to be able to access all of the constituent parts. This is not without its drawbacks though, as development can be very time-consuming and much work might be necessary to implement basic methods from which to build upon. One way to reduce these issues is by using an open-source approach, *i.e.*, developing software which is freely distributed for others to use. It is not always easy to have a unified approach though, as there are different programming languages used, different conventions for implementing methods, and the fact that not everyone will want to distribute their software freely. Nevertheless, it is possible to accelerate the development of computational software by using freely available open-source packages, as was the case for computational software developed for work in this dissertation.

The development of various computational methods were often originally prompted by a need to solve a direct scattering problem, *i.e.*, finding the scattered electromagnetic wave for a known object illuminated by a known incident wave. This can also be applied to antenna problems, where the antenna feed can be formulated as the incident wave. Another important, but typically much more difficult, problem is the inverse scattering problem. Here, the scattered wave is known, but either the scattering object or the incident wave is unknown [56]. To make matters worse, in practical settings the scattered wave is measured and will include noise and other measurement errors. To be able to solve the inverse problem, methods used in the direct problem are typically applied, but with additions to ensure that the inverse solution is accurate. This often comes in the form of optimization formulations where the direct problem, or problems similar to it, may need to be solved many times for different source distributions [56, 98]. Solutions of inverse problems, for this reason, often require efficient direct solvers. With the development of faster methods in computational electromagnetics (CEM), as well as improved performance on the computer hardware side, the solution of inverse problems have become increasingly attainable in recent decades. One
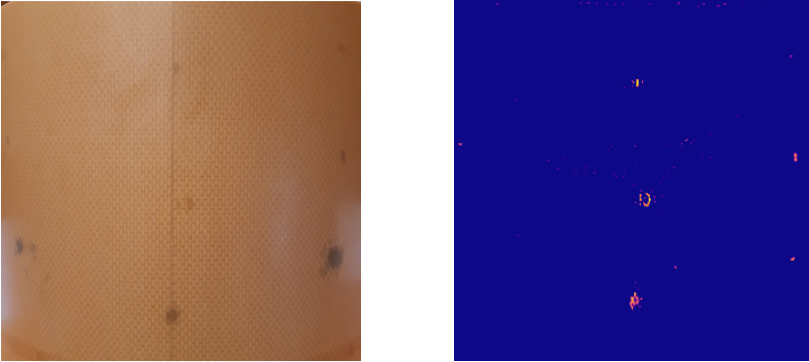
Figure 2: Example of an industrially manufactured composite panel (left) and an image indicating flaws (right).

use of inverse scattering is for nondestructive testing (NDT) in industrial settings. This is an area in which other physical phenomena like ultrasound and x-rays have been used for many decades, while the use of microwaves is relatively new [131, 168]. The typical use case is to detect flaws in a manufactured product without affecting it negatively [131]. In many cases, it can also be interesting to do this by generating an image, showing the possible locations of flaws as seen in Figure 2. For microwaves, such imaging has been performed with a wide range of methods which are not related to inverse scattering [2, 98]. Often, these methods are computationally cheaper than the alternatives based on inverse scattering, but with less information regarding the physical characteristics of the sample. Furthermore, methods in inverse scattering can use prior knowledge of the sample to improve images in ways not possible using traditional methods [98].

For NDT, as in similar areas like medical imaging, an interesting idea is the simultaneous use of multiple physical phenomena [42]. In particular, the wide use of ultrasound makes for an interesting possible combination with the newer microwave methods, especially since there are well-known interaction mechanisms for the interaction between acoustic and electromagnetic waves. This interaction has been known for over a century [22], but has found most of its use in the optical frequency range of electromagnetic waves. This field of acousto-optics has led to the development of many devices in photonics [79, 123], but there are also some applications where radar systems have been enhanced with acoustic transmitters for detection of atmospheric phenomena otherwise undetectable [88, 89]. In acousto-optics, the two waves essentially travel perpendicular to each other, while in the radar setting they travel in parallel. For a possible NDT application, it might be interesting to have an oblique incidence to limit the region in which possible flaws could interact with the waves. Study of this type of interaction based on possible use in NDT is included in this dissertation.

1.1   Structure

The structure of this introduction is as follows. Section 2 gives a brief overview of the electromagnetic theory necessary for the work in this dissertation, and particularly for the other sections of this introduction. Section 3 describes the computational methods used in this dissertation, methods of accelerating computations, and issues related to implementing computational methods in software. Section 4 introduces the topic of imaging using electromagnetic waves, and describes two different methods of doing so. Section 5 describes some techniques for measuring electromagnetic waves, issues that arise and how to solve them, and how these techniques were used in the included papers. Section 6 describes the contributions of different parts of this dissertation and how they fit together, and finally section 7 concludes this introduction and provides an outlook on possible future work.

1.2   Notation

In this introduction, the notation is as follows

- Scalars are written in italic as A.

- Vectors are written in bold italic as $\boldsymbol{A}$.

- Matrices are written in bold upright as $\mathbf{A}$.

- The entry on row m, column n of a matrix $\mathbf{A}$ is written as A_{mn}.

- Tensors are written with double overlines as $\overline{\overline{A}}$.

Matrix notation is generally used for numerical matrices in a fixed basis. Tensor notation, however, is used for physical properties where there may not be a reference to a particular basis. Vector notation is the same for both numerical vectors and physical vectors though. This is consistent within the introduction, but not in the included papers.

2   Basic Electromagnetic Theory

Maxwell's equations are a set of coupled partial differential equations (PDE) which are the basis of all classical electromagnetics. A general, time-dependent form of Maxwell's equations is [68, 80]

$$\nabla \times \boldsymbol{\mathcal{E}}(\boldsymbol{r}, t) = -\frac{\partial \boldsymbol{\mathcal{B}}(\boldsymbol{r}, t)}{\partial t} \tag{2.1}$$

$$\nabla \times \boldsymbol{\mathcal{H}}(\boldsymbol{r}, t) = \boldsymbol{\mathcal{J}}(\boldsymbol{r}, t) + \frac{\partial \boldsymbol{\mathcal{D}}(\boldsymbol{r}, t)}{\partial t} \tag{2.2}$$

$$\nabla \cdot \boldsymbol{\mathcal{D}}(\boldsymbol{r}, t) = \rho_{\mathrm{e}}(\boldsymbol{r}, t) \tag{2.3}$$

$$\nabla \cdot \boldsymbol{\mathcal{B}}(\boldsymbol{r}, t) = 0 \tag{2.4}$$

where $\boldsymbol{\mathcal{E}}$ is the electric field (unit V/m), $\boldsymbol{\mathcal{H}}$ is the magnetic field (unit A/m), $\boldsymbol{\mathcal{D}}$ is the electric flux density (unit As/m^2), $\boldsymbol{\mathcal{B}}$ is the magnetic flux density (unit Vs/m^2), $\boldsymbol{\mathcal{J}}$ is the electric current density (unit A/m^2) and ρ_{e} is the electric charge (unit As). In free space, the fields are also connected as $\boldsymbol{\mathcal{D}} = \varepsilon_0 \boldsymbol{\mathcal{E}}$ and $\boldsymbol{\mathcal{B}} = \mu_0 \boldsymbol{\mathcal{H}}$ where ε_0 and μ_0 are the permittivity and permeability of free space, respectively (other cases are discussed in section 2.2). These constants have numerical values [143]

$$\varepsilon_0 \approx 8.854 \cdot 10^{-12}\,\mathrm{F/m} \tag{2.5}$$

$$\mu_0 \approx 1.257 \cdot 10^{-6}\,\mathrm{H/m}. \tag{2.6}$$

It is noticeable that Maxwell's equations are not fully symmetric in the sense that there are only electric currents and charges. A more symmetric version would be [68, 71]

$$\nabla \times \boldsymbol{\mathcal{E}}(\boldsymbol{r}, t) = -\boldsymbol{\mathcal{M}}(\boldsymbol{r}, t) - \frac{\partial \boldsymbol{\mathcal{B}}(\boldsymbol{r}, t)}{\partial t} \tag{2.7}$$

$$\nabla \times \boldsymbol{\mathcal{H}}(\boldsymbol{r}, t) = \boldsymbol{\mathcal{J}}(\boldsymbol{r}, t) + \frac{\partial \boldsymbol{\mathcal{D}}(\boldsymbol{r}, t)}{\partial t} \tag{2.8}$$

$$\nabla \cdot \boldsymbol{\mathcal{D}}(\boldsymbol{r}, t) = \rho_{\mathrm{e}}(\boldsymbol{r}, t) \tag{2.9}$$

$$\nabla \cdot \boldsymbol{\mathcal{B}}(\boldsymbol{r}, t) = \rho_{\mathrm{m}}(\boldsymbol{r}, t). \tag{2.10}$$

where the magnetic current density $\boldsymbol{\mathcal{M}}$ and charge ρ_{m} have been introduced. These new quantities have never been observed in nature, but they can be useful as theoretical sources in certain applications. They will, for example, make an appearance in this dissertation with the discussion of the surface equivalence theorem, which in turn is a crucial building block for many of the computational methods presented later.

An alternative to the time-domain formulation above is to express the equations in the frequency domain, by utilizing the Fourier transform. The electric field in frequency and time domain respectively are connected to each other

as [71, 80]

$$\boldsymbol{E}(\boldsymbol{r},\omega) = \int_{-\infty}^{\infty} \boldsymbol{\mathcal{E}}(\boldsymbol{r},t)\mathrm{e}^{-\mathrm{j}\omega t}\,\mathrm{d}t \tag{2.11}$$

$$\boldsymbol{\mathcal{E}}(\boldsymbol{r},t) = \frac{1}{2\pi}\int_{-\infty}^{\infty} \boldsymbol{E}(\boldsymbol{r},\omega)\mathrm{e}^{\mathrm{j}\omega t}\,\mathrm{d}\omega \tag{2.12}$$

and similarly for all other quantities. The quantity $\boldsymbol{E}(\boldsymbol{r},\omega)$ is a complex quantity for the electric field in the frequency domain. For many applications, it is practical to assume a time-harmonic behavior of the electromagnetic fields, i.e.

$$\boldsymbol{\mathcal{E}}(\boldsymbol{r},t) = \boldsymbol{E}_0(\boldsymbol{r})\cos(\omega t + \phi) \tag{2.13}$$

where ϕ is a phase factor contained within $\boldsymbol{E}(\boldsymbol{r},\omega)$ in the frequency domain. The relation between time and frequency domain quantities then simplifies to

$$\boldsymbol{\mathcal{E}}(\boldsymbol{r},t) = \mathrm{Re}\{\boldsymbol{E}(\boldsymbol{r},\omega)\mathrm{e}^{\mathrm{j}\omega t}\}, \tag{2.14}$$

again exemplified by the electric field. Maxwell's equations are often used in a form given by time-harmonic fields, i.e. [71]

$$\nabla \times \boldsymbol{E}(\boldsymbol{r},\omega) = -\boldsymbol{M}(\boldsymbol{r},\omega) - \mathrm{j}\omega\boldsymbol{B}(\boldsymbol{r},\omega) \tag{2.15}$$
$$\nabla \times \boldsymbol{H}(\boldsymbol{r},\omega) = \boldsymbol{J}(\boldsymbol{r},\omega) + \mathrm{j}\omega\boldsymbol{D}(\boldsymbol{r},\omega) \tag{2.16}$$
$$\nabla \cdot \boldsymbol{D}(\boldsymbol{r},\omega) = \rho_{\mathrm{e}}(\boldsymbol{r},\omega) \tag{2.17}$$
$$\nabla \cdot \boldsymbol{B}(\boldsymbol{r},\omega) = \rho_{\mathrm{m}}(\boldsymbol{r},\omega) \tag{2.18}$$

where magnetic current density and charge were again included. The ω is typically not written explicitly further in this introduction, unless there is some dependence on frequency or other reason to specify it. It should be noted that fields in the frequency domain can be defined in different ways. In this thesis, the definition follows (2.14), but it is common in the literature to define it using the exponential $\mathrm{e}^{-\mathrm{i}\omega t}$ instead. For the time-harmonic fields, and other complex quantities, this time convention can be changed by substituting the imaginary unit j for $-$i anywhere it appears [80].

2.1   Electromagnetic Waves

For time-varying electromagnetic fields, the concept of electromagnetic waves arises. Here, this is exemplified using the time-harmonic formulation, but it holds for any time variation as this can be transformed to the frequency domain (as seen in (2.11)). In the simplest case, we consider electromagnetic fields in free space with purely electric currents $\boldsymbol{J}$ acting as sources. If the curl is applied to (2.15), one obtains

$$\nabla \times \nabla \times \boldsymbol{E}(\boldsymbol{r}) = -\mathrm{j}\omega\mu_0\nabla \times \boldsymbol{H}(\boldsymbol{r}) = \omega^2\mu_0\varepsilon_0\boldsymbol{E}(\boldsymbol{r}) - \mathrm{j}\omega\mu_0\boldsymbol{J}(\boldsymbol{r}) \tag{2.19}$$

where $\nabla \times \boldsymbol{H}$ was identified with the left-hand side of (2.16). Cleaning this up gives

$$\nabla \times \nabla \times \boldsymbol{E}(\boldsymbol{r}) - k_0^2 \boldsymbol{E} = -\mathrm{j}k_0\eta_0 \boldsymbol{J}(\boldsymbol{r}) \qquad (2.20)$$

which is often called the curl-curl equation or the vector wave equation. In the equation, the wave number k_0 was introduced as $k_0 = \omega/c_0$ where c_0 is the propagation speed of the wave as

$$c_0 = \frac{1}{\sqrt{\varepsilon_0\mu_0}} = 299\,792\,458\,\mathrm{m/s} \qquad (2.21)$$

otherwise known as the speed of light in vacuum. The wave impedance of free space $\eta_0 = \sqrt{\mu_0/\varepsilon_0}$ was also introduced. Solutions to (2.20) are electromagnetic waves with frequency f and wavelength λ given by

$$f = \frac{\omega}{2\pi} \qquad (2.22)$$

$$\lambda = \frac{c_0}{f}. \qquad (2.23)$$

The exact solution to (2.20) of course depends on the problem, but there are some canonical wave solutions that are particularly important. Two of them are illustrated here: plane waves and spherical waves. For simplicity, only the scalar complex amplitudes $A = |\boldsymbol{E}|$ are considered at first. Plane waves can be expressed as [80]

$$A(\boldsymbol{r}) = A_0\mathrm{e}^{-\mathrm{j}k_0\hat{\boldsymbol{k}}\cdot\boldsymbol{r}} \qquad (2.24)$$

where A_0 is a complex amplitude of the wave and $\hat{\boldsymbol{k}}$ is a unit vector in the direction of propagation. The plane wave is what many might think of when they hear the word wave, as flat wavefronts propagating in a single direction. Plane waves are simple to analyze, and they can act as good approximations in many applications such as scattering. Spherical waves, on the other hand, can be expressed as [80]

$$A(r) = F_0\frac{\mathrm{e}^{-\mathrm{j}k_0 r}}{r} \qquad (2.25)$$

where r is the radial coordinate from an origin and F_0 is an amplitude (unit V). The appearance of the spherical wave is shown to the left in Figure 3. In contrast to the plane wave, the spherical wave has a clear source at $r = 0$ and a diminishing amplitude as it propagates further from its source, which in terms of power scales as $1/r^2$. This is the well-known inverse square law. As indicated in Figure 3, spherical waves can be approximated as plane waves if the distance from the source becomes large enough, and within a small enough angular region.

While plane wave approximations is a useful concept for observations far from a radiator, a more general one is that of near fields and far fields. This is related to how an electromagnetic wave radiated by a source evolves with increasing range. Far enough away from the source, the electric field can be expressed on the particular form [80]

$$\boldsymbol{E}(\boldsymbol{r}) = \frac{\mathrm{e}^{-\mathrm{j}k_0 r}}{r}\boldsymbol{F}(\hat{\boldsymbol{r}}) \qquad (2.26)$$
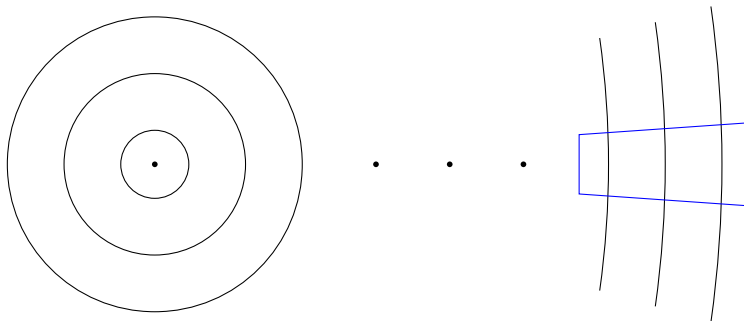
Figure 3: Spherical wave propagating from a source. Within a small angular region far from the source (marked in blue) it is approximately a plane wave.

where $\boldsymbol{F}(\hat{\boldsymbol{r}})$ is called the far-field amplitude and only depends on the direction $\hat{\boldsymbol{r}}$, and not the distance r from the source. By comparing (2.26) to (2.25), it is clear that electromagnetic waves in the far field behave as spherical waves, but with an amplitude that depends on the direction. The far-field amplitude is always perpendicular to the propagation direction $\hat{\boldsymbol{k}}$ (transverse), and the fields in this region behave as $\boldsymbol{E} = \eta_0 \boldsymbol{H} \times \hat{\boldsymbol{k}}$. The polarization of ideal spherical waves in (2.25) and plane waves in (2.24) follow this. Closer to the source, *i.e.*, in the near field, the electric field can have more complicated forms. It is not clear, however, from (2.26) where the cutoff between near and far fields occurs. There is no exact, universally agreed upon definition of this, but a common rule for the cutoff range between near and far fields is the Fraunhofer distance given by [11, 147]

$$r > \frac{2D^2}{\lambda} \tag{2.27}$$

where D is introduced as the largest dimension of the radiating source, though it is often also added that $r \gg \lambda$ and $r \gg D$ [80].

2.2   Constitutive Relations of Different Media

While Maxwell's equations as presented in (2.1)–(2.4) hold for any medium, they do not provide any information on how charges and currents in the medium behave. This is described by the constitutive relations of a medium, which connect the fields $\boldsymbol{\mathcal{E}}$ and $\boldsymbol{\mathcal{H}}$ to $\boldsymbol{\mathcal{D}}$ and $\boldsymbol{\mathcal{B}}$. The work presented in this dissertation is limited to linear media, which limits the types of relations which are possible. In the time domain, general linear constitutive relations can be expressed using convolutions

on the form [80]

$$\boldsymbol{\mathcal{D}}(t) = \varepsilon_0 \left(\bar{\bar{\varepsilon}} \cdot \boldsymbol{\mathcal{E}}(t) + \int\limits_{-\infty}^{t} \bar{\bar{\chi}}_{\mathrm{ee}}(t - t') \cdot \boldsymbol{\mathcal{E}}(t')\, \mathrm{d}t' + \eta_0 \int\limits_{-\infty}^{t} \bar{\bar{\chi}}_{\mathrm{em}}(t - t') \cdot \boldsymbol{\mathcal{H}}(t')\, \mathrm{d}t' \right)$$

(2.28)

$$\boldsymbol{\mathcal{B}}(t) = \mu_0 \left(\frac{1}{\eta_0} \int\limits_{-\infty}^{t} \bar{\bar{\chi}}_{\mathrm{me}}(t - t') \cdot \boldsymbol{\mathcal{E}}(t')\, \mathrm{d}t' + \bar{\bar{\mu}} \cdot \boldsymbol{\mathcal{H}}(t) + \int\limits_{-\infty}^{t} \bar{\bar{\chi}}_{\mathrm{mm}}(t - t') \cdot \boldsymbol{\mathcal{H}}(t')\, \mathrm{d}t' \right)$$

(2.29)

where $\bar{\bar{\varepsilon}}$, $\bar{\bar{\mu}}$ describe the so-called optical response of the medium, which is the response to the fields $\boldsymbol{\mathcal{E}}$ and $\boldsymbol{\mathcal{H}}$ on a shorter time frame than the other terms. The four different $\bar{\bar{\chi}}_{\mathrm{xy}}$ are susceptibilities describing the response of the medium to electric and magnetic fields. The subscript xy indicates that the susceptibility describes response on field x due to field y, where they can be e (electric) and m (magnetic). The double overline indicates that the quantity is a tensor (specifically a dyadic tensor). This type of constitutive relation containing nonzero $\bar{\bar{\chi}}_{\mathrm{em}}$ and $\bar{\bar{\chi}}_{\mathrm{me}}$ is often called magnetoelectric.

Commonly, however, constitutive relations are expressed in the frequency domain. As the Fourier transform of a convolution is a regular product, the relations become mathematically simpler in this case. The general linear constitutive relations can then be expressed as [80]

$$\boldsymbol{D}(\omega) = \varepsilon_0 \left(\bar{\bar{\varepsilon_{\mathrm{r}}}}(\omega) \cdot \boldsymbol{E}(\omega) + \eta_0 \bar{\bar{\xi}}(\omega) \cdot \boldsymbol{H}(\omega) \right) \tag{2.30}$$

$$\boldsymbol{B}(\omega) = \mu_0 \left(\frac{1}{\eta_0} \bar{\bar{\zeta}}(\omega) \cdot \boldsymbol{E}(\omega) + \bar{\bar{\mu_{\mathrm{r}}}}(\omega) \cdot \boldsymbol{H}(\omega) \right). \tag{2.31}$$

In this, new quantities for the constitutive relations have been introduced from Fourier transformation of the previous ones. $\bar{\bar{\varepsilon_{\mathrm{r}}}}$ is called the relative permittivity and $\bar{\bar{\mu_{\mathrm{r}}}}$ is called the relative permeability. The quantities for the magnetoelectric coupling from $\boldsymbol{H}$ to $\boldsymbol{D}$ and $\boldsymbol{E}$ to $\boldsymbol{B}$ do not have similar universal names. This type of magnetoelectric relation is often called bianisotropic since both electric and magnetic fields are connected (bi) by tensors (anisotropic). However, most applications do not require these kinds of constitutive relations and there are simpler ones that are often seen. Media without magnetoelectric interaction is described using only relative permittivity and relative permeability as

$$\boldsymbol{D}(\omega) = \varepsilon_0 \bar{\bar{\varepsilon_{\mathrm{r}}}}(\omega) \cdot \boldsymbol{E}(\omega) \tag{2.32}$$

$$\boldsymbol{B}(\omega) = \mu_0 \bar{\bar{\mu_{\mathrm{r}}}}(\omega) \cdot \boldsymbol{H}(\omega). \tag{2.33}$$

Commonly, there are no magnetic effects ($\mu_0 \bar{\bar{\mu_{\mathrm{r}}}}(\omega) = \mu_0$) in which case the medium is called dielectric. As expressed above, it is still an anisotropic medium since the relative permittivity is a tensor, but an even simpler variety is the isotropic dielectric where it also holds that $\bar{\bar{\varepsilon_{\mathrm{r}}}}(\omega) = \varepsilon_{\mathrm{r}}(\omega) \bar{\bar{I}}$ where $\bar{\bar{I}}$ is the identity

tensor. In the constitutive relations presented above, a frequency dependence has been implied. This is generally the case, and such media are called dispersive [80]. Often in this dissertation, problems are considered only at a single frequency which means that dispersion does not play a role in the results. This often holds for small changes in frequency as well, where the dispersion is relatively small.

In general, medium parameters in the frequency domain constitutive relations are allowed to be complex-valued, and the properties determine the nature of losses in the medium. A medium can be lossless, meaning that waves propagating there do not lose or gain power, for which it holds that [80]

$$\overline{\overline{\varepsilon_{\mathrm{r}}}} = \overline{\overline{\varepsilon_{\mathrm{r}}}}^{\mathrm{H}} \tag{2.34}$$

$$\overline{\overline{\mu_{\mathrm{r}}}} = \overline{\overline{\mu_{\mathrm{r}}}}^{\mathrm{H}} \tag{2.35}$$

$$\overline{\overline{\xi}} = \overline{\overline{\zeta}}^{\mathrm{H}} \tag{2.36}$$

with $^{\mathrm{H}}$ indicating a Hermitian transpose. For a medium which is not lossless, waves propagating there can either lose or gain power, and they are called passive and active, respectively. For a passive medium (including the lossless case) it holds that [80]

$$\omega \operatorname{Im} \overline{\overline{\varepsilon_{\mathrm{r}}}} \leq 0 \tag{2.37}$$

$$\omega \operatorname{Im} \overline{\overline{\mu_{\mathrm{r}}}} \leq 0 \tag{2.38}$$

$$\omega \left\{ 4 \operatorname{Im} \overline{\overline{\mu_{\mathrm{r}}}} - \left(\overline{\overline{\xi}} - \overline{\overline{\zeta}}^{\mathrm{H}} \right)^{\mathrm{H}} \cdot \left(\operatorname{Im} \overline{\overline{\varepsilon_{\mathrm{r}}}} \right)^{-1} \cdot \left(\overline{\overline{\xi}} - \overline{\overline{\zeta}}^{\mathrm{H}} \right) \right\} \leq 0. \tag{2.39}$$

These inequalities should be interpreted to be valid for all Hermitian quadratic forms over the matrices in the left-hand side. Furthermore, the imaginary parts of dyadic tenors are interpreted as $\operatorname{Im} \overline{\overline{A}} = (\overline{\overline{A}} - \overline{\overline{A}}^{\mathrm{H}})/2\mathrm{j}$. If the conditions for a passive medium are simplified for the commonly used isotropic media, they become

$$\omega \operatorname{Im} \varepsilon_{\mathrm{r}} \leq 0 \tag{2.40}$$

$$\omega \operatorname{Im} \mu_{\mathrm{r}} \leq 0. \tag{2.41}$$

For isotropic dielectric media fulfilling Ohm's law $\boldsymbol{J} = \sigma \boldsymbol{E}$ with a real-valued permittivity $\varepsilon_{\mathrm{r}}'$ and electric conductivity σ, a direct relation between conductivity and losses is found by rewriting (2.16) as

$$\nabla \times \boldsymbol{H} = \boldsymbol{J} + \mathrm{j}\omega \boldsymbol{D} = \sigma \boldsymbol{E} + \mathrm{j}\omega \varepsilon_0 \varepsilon_{\mathrm{r}}' \boldsymbol{E} = \mathrm{j}\omega \varepsilon_0 \varepsilon_{\mathrm{r}} \boldsymbol{E} \tag{2.42}$$

with

$$\varepsilon_{\mathrm{r}} = \varepsilon_{\mathrm{r}}' - \mathrm{j}\frac{\sigma}{\omega \varepsilon_0}. \tag{2.43}$$

Another property that can be seen in the constitutive relations is reciprocity. Reciprocity is easier to understand if a one-dimensional network model is considered, as shown in Figure 4. This model contains an object (network) which
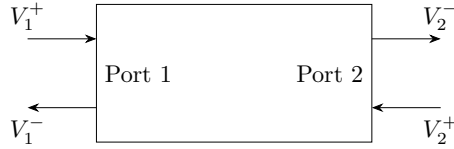
Figure 4: One-dimensional waves in a two-port network.

has two ports from which waves can enter and leave. Such a network can be described using the scattering parameters defined as the scattering matrix [110]

$$\begin{pmatrix} V_1^- \\ V_2^- \end{pmatrix} = \begin{bmatrix} S_{11} & S_{12} \\ S_{21} & S_{22} \end{bmatrix} \begin{pmatrix} V_1^+ \\ V_2^+ \end{pmatrix} \tag{2.44}$$

with in-going waves V^+ and out-going waves V^- as indicated in Figure 4. In a reciprocal network, the scattering matrix is symmetrical, which holds for a network with any number of ports [110]. What this means in our two-port network is that if we have in-going waves $V_1^+ = V_a$, $V_2^+ = 0$ and an out-going wave $V_2^- = V_b$, the situation can be reversed as $V_1^+ = 0$, $V_2^+ = V_a$ and $V_1^- = V_b$. Note that the reflected waves (V_1^- in the first case, V_2^- in the second) do not need to be the same. The property of reciprocity can also be defined more generally for media with constitutive relations instead of S-parameters and electromagnetic fields instead of voltages. For a medium to be reciprocal, its constitutive relations must be such that [80]

$$\overline{\overline{\varepsilon_{\mathrm{r}}}} = \overline{\overline{\varepsilon_{\mathrm{r}}}}^{\mathrm{T}} \tag{2.45}$$

$$\overline{\overline{\mu_{\mathrm{r}}}} = \overline{\overline{\mu_{\mathrm{r}}}}^{\mathrm{T}} \tag{2.46}$$

$$\overline{\overline{\xi}} = -\overline{\overline{\zeta}}^{\mathrm{T}}. \tag{2.47}$$

While these relations make consequences more complex to define than in the two-port network example, the same general property holds in that sources (currents) and effects (fields) in two points can be interchanged for the same result in a reciprocal medium. There are many examples of nonreciprocal media and situations that have important effects.

A nonreciprocal medium used in practical applications is the magnetized ferrite, which is used in many microwave devices such as the circulator which is a multi-port device in which signals can only propagate in one direction (*e.g.*, $1 \to 2 \to 3 \to 1$ for three ports) [110]. Another important nonreciprocal medium is magnetized plasma, which is found naturally in the ionosphere and causes polarization rotation of electromagnetic waves in different directions depending on the direction of travel [71, 147]. Finally, nonreciprocal artificial materials have been popular recently, with examples as nonreciprocal metamaterials obtaining nonreciprocity in new ways like modulation of the surface in space and time [27, 137].

2.3   Boundary Conditions

Maxwell's equations together with suitable constitutive relations describe the physics of classical electromagnetism within a certain medium. However, they do not describe what happens at the boundary between different media. For this reason, additional conditions are required at each such instance. These are commonly described as boundary conditions, although the fact that they appear at interfaces within problem domain means that they might not be so in a strict mathematical sense. The conditions are defined at any surface with a normal vector $\hat{\boldsymbol{n}}$ pointing from region 2 to region 1 are given by [71]

$$\hat{\boldsymbol{n}} \times (\boldsymbol{E}_1 - \boldsymbol{E}_2) = -\boldsymbol{M}_{\mathrm{s}} \tag{2.48}$$

$$\hat{\boldsymbol{n}} \cdot (\boldsymbol{D}_1 - \boldsymbol{D}_2) = \rho_{\mathrm{e,s}} \tag{2.49}$$

$$\hat{\boldsymbol{n}} \times (\boldsymbol{H}_1 - \boldsymbol{H}_2) = \boldsymbol{J}_{\mathrm{s}} \tag{2.50}$$

$$\hat{\boldsymbol{n}} \cdot (\boldsymbol{B}_1 - \boldsymbol{B}_2) = \rho_{\mathrm{m,s}}. \tag{2.51}$$

$\boldsymbol{J}_{\mathrm{s}}$ and $\boldsymbol{M}_{\mathrm{s}}$ are electric and magnetic surface currents and $\rho_{\mathrm{e,s}}$ and $\rho_{\mathrm{m,s}}$ are electric and magnetic surface charges. As previously stated, magnetic charges and currents are not physically shown to exist, but can be useful as fictitious quantities.

A commonly used boundary condition is for the boundary of a perfect electric conductor (PEC) object. PEC is an idealized model of an electric conductor in that it has an unlimited supply of electric charge which can perfectly oppose any fields on its interior, which can be seen as an electric conductivity $\sigma \to \infty$ [80]. Furthermore, as it is a model for a physical medium only electric currents and charges are supported on its boundary. The PEC boundary conditions can thus be expressed as [80]

$$\hat{\boldsymbol{n}} \times \boldsymbol{E} = \boldsymbol{0} \tag{2.52}$$

$$\hat{\boldsymbol{n}} \cdot \boldsymbol{D} = \rho_{\mathrm{e,s}} \tag{2.53}$$

$$\hat{\boldsymbol{n}} \times \boldsymbol{H} = \boldsymbol{J}_{\mathrm{s}} \tag{2.54}$$

$$\hat{\boldsymbol{n}} \cdot \boldsymbol{B} = 0. \tag{2.55}$$

While electric conductors typically are lossy due to a finite conductivity, the PEC model works well for many metals in the microwave frequency range. However, as the frequency reaches the optical range, metals no longer behave as classical conductors and the PEC model is not accurate [147]. In computations, the model is very beneficial since bulk conductors can be replaced by a boundary condition, reducing the number of unknowns in the problem. Analogously to PEC, a perfect magnetic conductor (PMC) can be defined to only support magnetic currents and
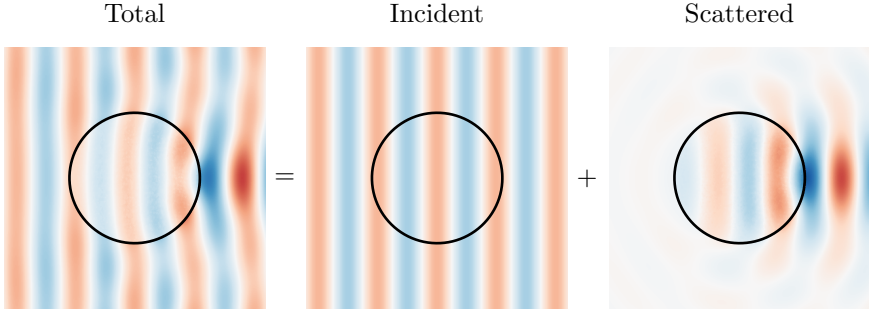
Figure 5: Scattering of an electromagnetic wave by a dielectric cylinder, shown for the component of $\boldsymbol{E}$ perpendicular to paper. The total electric field is considered a sum of the incident field and the scattered field.

charges on its boundary [71]. This PMC boundary condition can be expressed as

$$\hat{\boldsymbol{n}} \times \boldsymbol{E} = -\boldsymbol{M}_{\text{s}} \tag{2.56}$$

$$\hat{\boldsymbol{n}} \cdot \boldsymbol{D} = 0 \tag{2.57}$$

$$\hat{\boldsymbol{n}} \times \boldsymbol{H} = \boldsymbol{0} \tag{2.58}$$

$$\hat{\boldsymbol{n}} \cdot \boldsymbol{B} = \rho_{\text{m,s}}. \tag{2.59}$$

While the PMC does not resemble any physical medium as the PEC, it is possible to create artificial materials which act as PMC within certain limited conditions on, for example, frequency or propagation direction of a wave. This includes well-known structures like the mushroom high-impedance surface [132] and gaps in strip-based artificial soft/hard surfaces [76]. PEC and PMC boundary conditions can also be used in computations for problems with symmetries such that the fields are known *a priori* to act as if such surfaces were present, which reduces the number of unknowns.

2.4   Scattering

When electromagnetic waves encounter obstacles, typically in the form of a medium with different properties, interaction with the object causes scattering of the wave. An overview of how this problem is normally set up is shown in Figure 5 where the electric field of the wave is considered. The total electric field $\boldsymbol{E}$ is shown as a sum of the incident field $\boldsymbol{E}^{\text{inc}}$ and the scattered field $\boldsymbol{E}^{\text{sc}}$. The incident field is the field that would have been present without the obstacle, a plane wave in this case. The scattered field can be considered to be generated by sources on and in the obstacle to give the total field.

To compute the scattering of a general obstacle, it is almost always necessary to use numerical methods. In certain cases there are analytical solutions, with one of the most commonly known being the sphere. In the case of spherical symmetry, scattering problems are solved by the well-known Mie series solution [80, 94].

The simplest one is for a PEC sphere, but solutions are also possible for many other objects with spherical symmetry, including homogeneous dielectric, PEC coated by dielectric and multilayered spheres [41, 80]. The Mie series solution is particularly interesting for use in verification of numerical codes as it is well known and exact.

A quantity that is commonly used to quantify electromagnetic scattering by an obstacle is the radar cross section (RCS), which considers how an obstacle scatters an incident plane wave. This is typically specified to be monostatic or bistatic, where the former only considers the reverse of the incident wave direction while the latter considers scattering in all directions. The bistatic RCS σ is defined by an IEEE standard [141], but here it is introduced based on incident and scattered electric fields as [71, 115]

$$\sigma(\theta, \phi, \theta^{\mathrm{inc}}, \phi^{\mathrm{inc}}) = \lim_{r \to \infty} 4\pi r^2 \frac{|\boldsymbol{E}^{\mathrm{sc}}(r, \theta, \phi)|^2}{|\boldsymbol{E}^{\mathrm{inc}}(\theta^{\mathrm{inc}}, \phi^{\mathrm{inc}})|^2} \tag{2.60}$$

where $\boldsymbol{E}^{\mathrm{inc}}(\theta^{\mathrm{inc}}, \phi^{\mathrm{inc}})$ is the electric field of a plane wave incident in the direction $(\theta^{\mathrm{inc}}, \phi^{\mathrm{inc}})$ and $\boldsymbol{E}^{\mathrm{sc}}(r, \theta, \phi)$ is the scattered electric field in the point (r, θ, ϕ). The scattered electric field can be replaced by the far-field amplitude from (2.26) as

$$\sigma(\theta, \phi, \theta^{\mathrm{inc}}, \phi^{\mathrm{inc}}) = \lim_{r \to \infty} 4\pi r^2 \frac{|\mathrm{e}^{-\mathrm{j}k_0 r} \boldsymbol{F}^{\mathrm{sc}}(\theta, \phi)/r|^2}{|\boldsymbol{E}^{\mathrm{inc}}(\theta^{\mathrm{inc}}, \phi^{\mathrm{inc}})|^2} = 4\pi \frac{|\boldsymbol{F}^{\mathrm{sc}}(\theta, \phi)|^2}{|\boldsymbol{E}^{\mathrm{inc}}(\theta^{\mathrm{inc}}, \phi^{\mathrm{inc}})|^2}. \tag{2.61}$$

It is seen that this expression has the advantage that dependence on r and the limit are eliminated from the expression, and the RCS on this form is fairly simple to compute.

While not necessarily exact, many scattering problems can be solved approximately if the object is very large or small compared to the wavelength. For very small objects, Rayleigh scattering dominates and this can be solved analytically, though it is an approximation [80]. For very large objects, the classical laws of ray optics become useful and the RCS of PEC objects approach the geometrical cross section [80, 115]. It is generally in the region between where the scattering problem can be the most difficult to solve, and this is where full numerical solutions can be necessary. An indication of this can be seen by looking at the monostatic RCS of a PEC sphere computed from the Mie series for increasing sphere radius. This is shown in Figure 6, where three different scattering regimes can be seen. For very small radii the RCS increases monotonically, which is followed by significant variation, and finally at very large radii the RCS approaches a constant value. These are called the Rayleigh, resonance and optical scattering regimes, respectively [115].
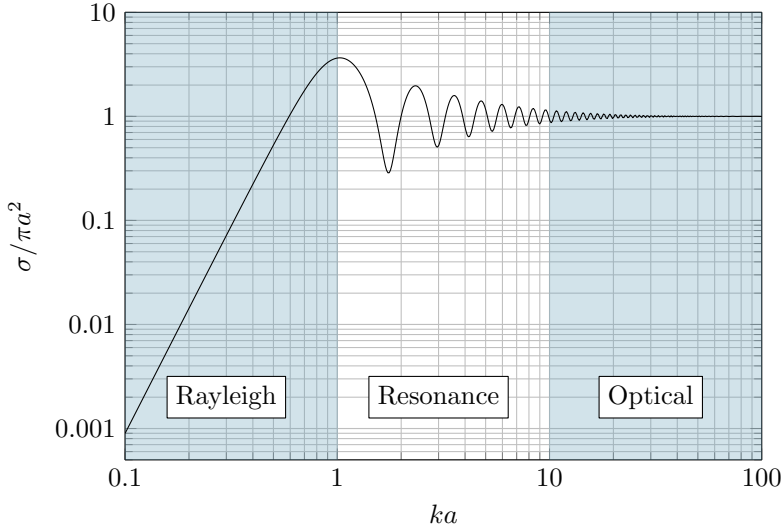
Figure 6: Monostatic RCS normalized to geometric cross-section for a PEC sphere of increasing radius. Rough ka ranges of different scattering regimes are indicated.

2.5 Mechanical Perturbations of the Medium

In many cases, a medium can change its electromagnetic properties due to other physical phenomena. In this dissertation there are two examples that deserve special focus: acoustic waves, which is relevant in Paper V, and rotating media, which is relevant in Paper III. Both of these phenomena are based on mechanical perturbations which are time-harmonic in their nature, and this time-harmonic nature affects how electromagnetic waves interact with them. Recently, there has been a large interest in phenomena similar to these, where properties of a system are time-modulated to introduce new interesting effects, as already mentioned with respect to nonreciprocal effects at the end of section 2.2.

2.5.1 Acoustic Waves

The possibility for interaction between acoustic and electromagnetic waves has been known since at least 1922 [22], and the theory of acousto-optics developed in the following decades [79]. Following the invention of the laser, acousto-optics has been applied to photonic devices used to modify properties of laser beams like modulators and filters [79, 123]. While most development has been in acousto-optics, interaction between acoustic and electromagnetic waves is not limited to optical frequencies. An application at other electromagnetic frequencies is radio-acoustic sounding which uses collocated radar and acoustic transmitters to measure atmospheric properties like temperature profiles [88, 89], but with other

possible uses including forest fire detection [122] or aircraft wake vortices [119].

In its most basic form, interaction between electromagnetic and acoustic waves can be understood as the acoustic wave modulating the density of a medium, which in turn affects its dielectric properties and causes the electromagnetic wave to scatter [79, 123]. In fluids, this is a fairly correct picture as acoustic waves directly correspond to changes in density in this case. In solids, the picture becomes more difficult since more modes of acoustic, or rather elastic, waves are possible. For example, acoustic waves based on pressure are still supported as so called p-waves, but so are s-waves which are waves based on shear strain in the solid [118].

Photoelasticity provides the theory for how elastic phenomena affect electromagnetic properties of a medium. In solids, it is generally the case that both elastic and electromagnetic properties are tensors, which makes for somewhat complicated relations between them [79]. A relation for small perturbations in a mechanically and electromagnetically isotropic medium is [157]

$$\varepsilon = \varepsilon_0(\varepsilon_\mathrm{r} + \varepsilon_1) \tag{2.62}$$

$$\varepsilon_1 = \frac{\varepsilon_\mathrm{r}\mathfrak{p}}{K}p \tag{2.63}$$

where $\mathfrak{p}$ is a scalar photoelastic constant, K is the bulk modulus and p is the acoustic pressure. For fluids, an expression for the scalar photoelastic constant can be found using the Lorentz-Lorenz relations as [79, 157]

$$\mathfrak{p} = \frac{(\varepsilon_\mathrm{r} - 1)(\varepsilon_\mathrm{r} + 2)}{3\varepsilon_\mathrm{r}^2}. \tag{2.64}$$

From this, it can be understood that interaction in air, or other media with ε_r close to 1, is very weak.

Depending on the wavelengths of the acoustic and electromagnetic waves, and the overlap of the waves, strong scattering is due to different mechanisms. This can be quantified by the Klein-Cook parameter defined as [77, 79]

$$Q = \frac{2\pi\lambda L}{\Lambda^2} \tag{2.65}$$

where λ is the electromagnetic wavelength, Λ is the acoustic wavelength and L is the length of the overlap between the waves. The main scattering mechanism is Raman-Nath diffraction if $Q \ll 1$, and Bragg diffraction if $Q \gg 1$ [77]. The typical case where Raman-Nath diffraction is important is in acousto-optics for thin beams where $\lambda \ll \Lambda$ and waves have perpendicular incidence [123]. In cases where $\lambda \sim \Lambda$ it is not immediately clear which mechanism is most relevant, but L only needs to be a small number of wavelengths for Bragg diffraction to dominate [77]. For the work presented in Paper V of this dissertation, Bragg diffraction dominates, and as such this will be the focus here.

Bragg diffraction as a general concept has its base in X-ray crystallography where the X-ray wavelength is phase matched to the separation between planes
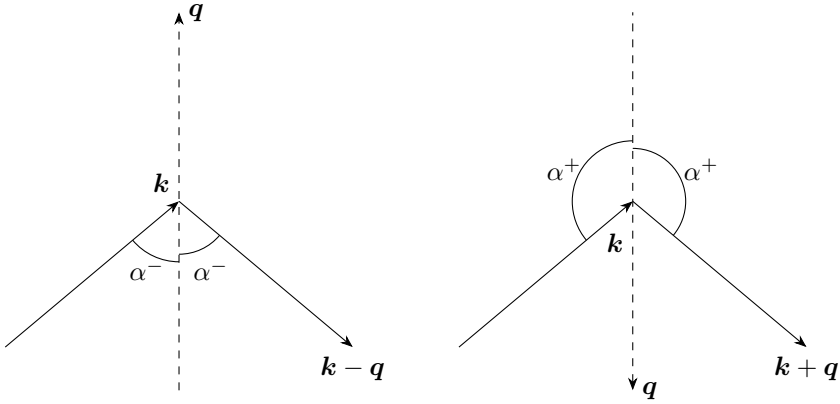
Figure 7: Incident acoustic (q) and electromagnetic (k) wave vectors, as well as scattered electromagnetic wave vector with the angle α shown. Both (-) and (+) cases of (2.66) are shown.

of atoms in a crystal lattice [20]. In interaction between acoustic and electromagnetic waves, the mechanism is similar but the planes of atoms are replaced by the acoustic wavefront which is moving, as opposed to the crystal lattice. The condition given by Bragg's law for strong scattering due to phase matching is essentially the same though, with crystal parameters exchanged for acoustic ones. It is usually expressed using the angle of incidence of the electromagnetic wave on the acoustic wave [79, 123], but here is expressed using the angle between the electromagnetic and acoustic propagation directions α as [157]

$$\cos \alpha = \mp \frac{\lambda}{2\Lambda}. \tag{2.66}$$

The angle α for the two cases shown in Figure 7 for the acoustic wave vector q, the electromagnetic wave vector k for the incident wave, and the electromagnetic wave vector $k \pm q$ for the scattered wave [123]. While the condition for strong scattering is the same in X-ray crystallography and acousto-electromagnetic interaction, the moving acoustic wave introduces some differences. Most prominently, the scattered electromagnetic wave exhibits a positive or negative frequency shift by the acoustic frequency, which can be understood by looking at the wave vectors for the scattered electromagnetic wave. As seen in Figure 7, sign of the frequency shift is the same as the sign in (2.66), and as such coupled to the angle α. This frequency shift can be crucial in measurements involving the interaction as it clearly indicates that a measured electromagnetic wave was scattered by the acoustic wave and not some other mechanism. In Paper V, for example, measurements would not have been possible without the existence of this frequency shift as the power scattered by the acoustic wave was significantly lower than even the leakage between transmitting and receiving antennas.

2.5.2   Rotating Media

Rapidly rotating dielectric media exhibit interesting electromagnetic properties. In the general case, it needs to be considered under the framework of the micro-Doppler effect, which considers objects under motion like rotation and vibration [31]. In the case of a rotating circular cylinder, the radial velocities which typically cause effects such as the micro-Doppler effect vanish. For sufficiently rapid rotations though, typically near 1 % of the speed of light, other effects become apparent, and it can be found that the object acts as if it were fully bianisotropic to a first order approximation [145]. While the problem is fairly exotic, it is interesting to study as it is bianisotropic, nonreciprocal and inhomogeneous by no other cause than mechanical rotation. The derivation of effective constitutive relations for moving media starts with the relations for a linear isotropic medium at rest, but are transformed to the laboratory frame. For non-relativistic speeds and to a first order approximation, the constitutive relations become [145, 147]

$$\boldsymbol{D} = \varepsilon_0 \varepsilon_{\mathrm{r}} \boldsymbol{E} + \frac{n^2 - 1}{c_0^2} \boldsymbol{v} \times \boldsymbol{H} \tag{2.67}$$

$$\boldsymbol{B} = \mu_0 \mu_{\mathrm{r}} \boldsymbol{H} - \frac{n^2 - 1}{c_0^2} \boldsymbol{v} \times \boldsymbol{E} \tag{2.68}$$

where $n = \sqrt{\varepsilon_{\mathrm{r}} \mu_{\mathrm{r}}}$ is the refractive index and $\boldsymbol{v}$ is the velocity vector at a particular point. For a circular cylinder rotating with angular frequency Ω around z, the velocity vector is

$$\boldsymbol{v} = \Omega \hat{\boldsymbol{z}} \times \boldsymbol{r} = \Omega(x\hat{\boldsymbol{y}} - y\hat{\boldsymbol{x}}) \tag{2.69}$$

in a Cartesian coordinate system. If this velocity is inserted in (2.67), the constitutive relations can be written using the bianisotropic parameters defined in (2.30)–(2.31) as

$$\overline{\overline{\varepsilon_{\mathrm{r}}}} = \varepsilon_{\mathrm{r}} \overline{\overline{I}} \tag{2.70}$$

$$\overline{\overline{\mu_{\mathrm{r}}}} = \mu_{\mathrm{r}} \overline{\overline{I}} \tag{2.71}$$

$$\overline{\overline{\xi}} = \Omega \frac{n^2 - 1}{c_0} \begin{bmatrix} 0 & 0 & x \\ 0 & 0 & y \\ -x & -y & 0 \end{bmatrix} \tag{2.72}$$

$$\overline{\overline{\zeta}} = -\overline{\overline{\xi}} \tag{2.73}$$

from which the inhomogeneous, bianisotropic, and nonreciprocal nature of the model is clear.
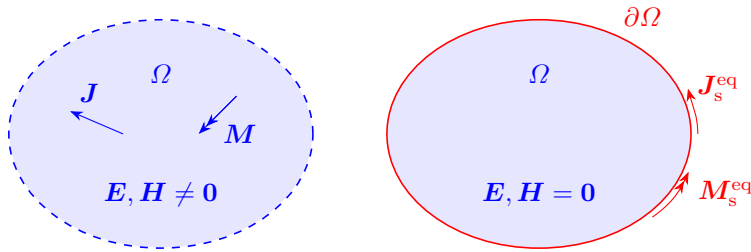
Figure 8: Illustration of the surface equivalence theorem with sources in Ω (left) replaced by equivalent surface currents on $\partial\Omega$ (right).

2.6   The Surface Equivalence Theorem

A powerful result from electromagnetic theory is the surface equivalence theorem, or surface equivalence principle. This states that sources within a volume Ω can be replaced by equivalent currents on the boundary $\partial\Omega$ and still give the same solution in the region outside Ω [58]. This is illustrated in Figure 8. While the solution outside Ω is the same after replacing the sources by equivalent currents, this is not the case for the solution inside of Ω. In fact, there is an infinite number of valid equivalent currents, and they result in different solutions inside Ω. There are some common choices though, with the most common one being the zero field, or Love condition. This sets the fields inside Ω to zero, which means that the equivalent currents can be found from the boundary conditions (2.48) and (2.50) to be

$$J_s^{\text{eq}} = \hat{n} \times H \tag{2.74}$$

$$M_s^{\text{eq}} = E \times \hat{n}. \tag{2.75}$$

This direct relationship between currents and fields can be very practical, as is seen in section 3.3 of this introduction.

   One issue that can arise in numerical applications of the equivalence theorem is the use of both electric and magnetic currents. In such applications, currents represent unknowns, and having both types would double the number of unknowns for a problem as compared with only one type of current. There are some ways of using either electric or magnetic currents in the equivalence theorem. One way of doing this is to consider the volume Ω filled with PMC, and electric currents on the surface $\partial\Omega$. This gives the same equivalent currents as in (2.74), and a dual method uses PEC and magnetic currents to give (2.75) instead [58]. However, this can be troublesome in numerical applications as the use of PMC or PEC require other methods than in the standard zero field case [111]. One exception is if the region Ω is a half space, meaning that $\partial\Omega$ is an infinite plane. In that case, the method of images can be used to eliminate the PMC/PEC and instead give equivalent currents as twice those in (2.74) and (2.75) [58]. Other methods for using only one of the electric and magnetic

currents exist, with some able to use the same methods as for free space. Typically they do not give the same simple relationships between currents and fields as in (2.74) and (2.75) though [111].

2.7   Integral Equations

Integral equations are important in many different electromagnetic problems. In particular, there are many numerical methods based on integral equations, some of which are described in more detail later in this dissertation.

The integral equations of interest in this work are based on the equivalence theorem. This enables the replacement of all electromagnetic phenomena within a closed object by equivalent surface currents on its boundary.

An important concept for integral equations is that of Green's functions, which is a general concept in mathematics with great applicability in electromagnetics. It can be likened to the impulse response in dynamical systems theory, but applied to differential operators. Generally, a Green's function is similar to the fundamental solution E which is [66]

$$LE = \delta \tag{2.76}$$

for a differential operator L and the Dirac delta distribution δ. As for impulse responses in dynamical systems theory, other problems involving L and a source term f can be solved by a convolution $E * f$ [66]. The Green's function is similar, but also take boundary conditions into account [134]. In electromagnetics, a Green's function can be obtained for the magnetic vector potential $\boldsymbol{A}$ (in the Lorenz gauge) in free space as the solution to [80]

$$\nabla^2 G_0(\boldsymbol{r}, \boldsymbol{r}') + k_0^2 G_0(\boldsymbol{r}, \boldsymbol{r}') = -\delta(\boldsymbol{r} - \boldsymbol{r}') \tag{2.77}$$

which is

$$G_0(\boldsymbol{r}, \boldsymbol{r}') = \frac{\mathrm{e}^{-\mathrm{j}k_0|\boldsymbol{r}-\boldsymbol{r}'|}}{4\pi|\boldsymbol{r} - \boldsymbol{r}'|}. \tag{2.78}$$

This Green's function can then be used to find vector potentials due to current sources, and this can in turn be used to find the electric and magnetic fields. Such a relation for the electric field can be written as [71]

$$\boldsymbol{E}(\boldsymbol{r}) = -\mathrm{j}k_0\eta_0 \int_\Omega \left[\boldsymbol{J}(\boldsymbol{r}')G_0(\boldsymbol{r}, \boldsymbol{r}') + \frac{1}{k_0^2}\boldsymbol{J}(\boldsymbol{r}') \cdot \nabla\nabla G_0(\boldsymbol{r}, \boldsymbol{r}') \right] \mathrm{d}V'$$
$$+ \int_\Omega \boldsymbol{M}(\boldsymbol{r}') \times \nabla G_0(\boldsymbol{r}, \boldsymbol{r}') \, \mathrm{d}V' \tag{2.79}$$

where both electric and magnetic currents inside a volume Ω are included.

To simplify notation of different integral equations, it is useful to introduce the integral operators [71]

$$\mathscr{L}(\boldsymbol{X})(\boldsymbol{r}) = \mathrm{j}k_0 \oint_{\partial\Omega} \left[\boldsymbol{X}(\boldsymbol{r}')G_0(\boldsymbol{r},\boldsymbol{r}') + \frac{1}{k_0^2}\nabla'\cdot\boldsymbol{X}(\boldsymbol{r}')\nabla G_0(\boldsymbol{r},\boldsymbol{r}') \right] \mathrm{d}S' \quad (2.80)$$

$$\mathscr{K}(\boldsymbol{X})(\boldsymbol{r}) = \oint_{\partial\Omega} \boldsymbol{X}(\boldsymbol{r}') \times \nabla G_0(\boldsymbol{r},\boldsymbol{r}')\,\mathrm{d}S' \quad (2.81)$$

defined for the closed surface $\partial\Omega$. The magnetic field and electric current are also scaled as $\bar{\boldsymbol{H}} = \eta_0\boldsymbol{H}$, $\bar{\boldsymbol{J}} = \eta_0\boldsymbol{J}$ for compactness. The integral equations considered here appear from a scattering problem where a volume Ω is illuminated by incident fields $\boldsymbol{E}^{\mathrm{inc}}$, $\bar{\boldsymbol{H}}^{\mathrm{inc}}$. To obtain the scattered field, the surface equivalence theorem can be applied using the zero field condition inside Ω, giving [32, 71]

$$\boldsymbol{E}^{\mathrm{inc}}(\boldsymbol{r}) - \mathscr{L}(\bar{\boldsymbol{J}}_{\mathrm{s}})(\boldsymbol{r}) + \mathscr{K}(\boldsymbol{M}_{\mathrm{s}})(\boldsymbol{r}) = \begin{cases} \boldsymbol{E}(\boldsymbol{r}) & \boldsymbol{r}\notin\Omega \\ \boldsymbol{0} & \boldsymbol{r}\in\Omega \end{cases} \quad (2.82)$$

$$\bar{\boldsymbol{H}}^{\mathrm{inc}}(\boldsymbol{r}) - \mathscr{L}(\boldsymbol{M}_{\mathrm{s}})(\boldsymbol{r}) - \mathscr{K}(\bar{\boldsymbol{J}}_{\mathrm{s}})(\boldsymbol{r}) = \begin{cases} \bar{\boldsymbol{H}}(\boldsymbol{r}) & \boldsymbol{r}\notin\Omega \\ \boldsymbol{0} & \boldsymbol{r}\in\Omega \end{cases}. \quad (2.83)$$

Classic integral equations are obtained in the limit of $\boldsymbol{r} \to \partial\Omega$, and by taking a cross product by $\hat{\boldsymbol{n}}$ as [71]

$$-\hat{\boldsymbol{n}} \times \mathscr{L}(\bar{\boldsymbol{J}}_{\mathrm{s}})(\boldsymbol{r}) + \hat{\boldsymbol{n}} \times \mathscr{K}(\boldsymbol{M}_{\mathrm{s}})(\boldsymbol{r}) = -\hat{\boldsymbol{n}} \times \boldsymbol{E}^{\mathrm{inc}}(\boldsymbol{r}) \quad (2.84)$$

$$\hat{\boldsymbol{n}} \times \mathscr{L}(\boldsymbol{M}_{\mathrm{s}})(\boldsymbol{r}) + \hat{\boldsymbol{n}} \times \mathscr{K}(\bar{\boldsymbol{J}}_{\mathrm{s}})(\boldsymbol{r}) = \hat{\boldsymbol{n}} \times \bar{\boldsymbol{H}}^{\mathrm{inc}}(\boldsymbol{r}) \quad (2.85)$$

where the first is the electric field integral equation (EFIE) and the second is the magnetic field integral equation (MFIE).

The equations written on this form are not fully usable as the integral operators contain a singularity which needs to be extracted, which can be done analytically as shown in many reference books [71, 80, 146, 152]. This treatment only affects the $\mathscr{K}$ operator as the extracted term vanishes for $\mathscr{L}$. For the $\mathscr{K}$ operator then, the extracted term depends on if the operator acts on the inside or outside of the volume enclosed by $\partial\Omega$. This is due to the extraction technique which depends on deformation of $\partial\Omega$ by a small region such that the singular point is excluded from the region of interest. The operator as modified by this extraction, $\tilde{\mathscr{K}}$, is given by [71]

$$\hat{\boldsymbol{n}} \times \mathscr{K}(\boldsymbol{X})(\boldsymbol{r}) = \hat{\boldsymbol{n}} \times \tilde{\mathscr{K}}(\boldsymbol{X})(\boldsymbol{r}) \pm \frac{1}{2}\boldsymbol{X}(\boldsymbol{r}) \quad (2.86)$$

if the surface $\partial\Omega$ is smooth. Here $+$ corresponds to evaluation on the outside of Ω and $-$ to evaluation on the inside. The integral equations in (2.84) and (2.85) are now written as

$$\frac{1}{2}\boldsymbol{M}_{\mathrm{s}}(\boldsymbol{r}) - \hat{\boldsymbol{n}} \times \mathscr{L}(\bar{\boldsymbol{J}}_{\mathrm{s}})(\boldsymbol{r}) + \hat{\boldsymbol{n}} \times \tilde{\mathscr{K}}(\boldsymbol{M}_{\mathrm{s}})(\boldsymbol{r}) = -\hat{\boldsymbol{n}} \times \boldsymbol{E}^{\mathrm{inc}}(\boldsymbol{r}) \quad (2.87)$$

$$\frac{1}{2}\bar{\boldsymbol{J}}_{\mathrm{s}}(\boldsymbol{r}) + \hat{\boldsymbol{n}} \times \mathscr{L}(\boldsymbol{M}_{\mathrm{s}})(\boldsymbol{r}) + \hat{\boldsymbol{n}} \times \tilde{\mathscr{K}}(\bar{\boldsymbol{J}}_{\mathrm{s}})(\boldsymbol{r}) = \hat{\boldsymbol{n}} \times \bar{\boldsymbol{H}}^{\mathrm{inc}}(\boldsymbol{r}) \quad (2.88)$$

with evaluation on the outside of Ω.

2.8   Characteristic Modes

Characteristic modes are an example of a set of orthogonal solutions to a scattering problem which can be useful in many design problems [53, 82]. Here, the characteristic modes are introduced from the perspective of a pure PEC object, which is a commonly used formulation [57]. For a PEC medium, the boundary supports electric but not magnetic currents. This makes the EFIE in (2.84) take on the form

$$\hat{\boldsymbol{n}} \times \mathscr{L}(\bar{\boldsymbol{J}})(\boldsymbol{r}) = \hat{\boldsymbol{n}} \times \boldsymbol{E}^{\mathrm{inc}}(\boldsymbol{r}). \tag{2.89}$$

This can be written in a different form as

$$\mathcal{Z}(\boldsymbol{I}) = \boldsymbol{V} \tag{2.90}$$

where $\mathcal{Z}$ corresponds to the $\mathscr{L}$-operator acting on current densities represented as $\boldsymbol{I}$ for an incident field represented as $\boldsymbol{V}$. The notation is chosen to resemble concepts from circuit theory, and consequently $\mathcal{Z}$ is called the impedance operator, $\boldsymbol{I}$ the current vector, and $\boldsymbol{V}$ the voltage vector. This notation is commonly used in the method of moments (MoM) computational method which is based on integral equations, and which is further discussed in section 3.2. In that case, discretization of the problem means that $\mathcal{Z}$, $\boldsymbol{I}$, and $\boldsymbol{V}$ are represented by matrices and vectors, but here the problem is considered from a pure operator point of view. Looking at the $\mathscr{L}$-operator defined in (2.80), it is clear that it is complex and as such the impedance operator is rewritten as

$$\mathcal{Z} = \mathcal{R} + \mathrm{j}\mathcal{X} \tag{2.91}$$

with $\mathcal{R}$ and $\mathcal{X}$ called resistance and reactance, respectively, following the theme from circuit theory. These new operators can in turn be used to define a generalized eigenvalue problem as

$$\mathcal{X}(\boldsymbol{I}_n) = \lambda_n \mathcal{R}(\boldsymbol{I}_n) \tag{2.92}$$

where the solutions are called characteristic modes with eigenvectors $\boldsymbol{I}_n$ and eigenvalues λ_n [57].

Characteristic modes have been known for a significant time [44, 95], but were not widely used until more recently with the emergence of many applications in antenna design [26, 82]. The recent work has mostly been based on the eigenvalue decomposition (2.92) described in [57], which limits applications to solvers and formulations based on an impedance operator. Recent work has shown how a formulation based on scattering problems, as originally proposed in [44], can be used more generally [28, 53, 54]. This formulation is in many ways more versatile than (2.92) in that the characteristic modes can be computed by solving a scattering problem independent of the underlying operator. Characteristic modes can then be computed using arbitrary solvers for electromagnetic scattering problems [28, 85].

3 Computational Methods

Much of the success of modern electromagnetic applications can be attributed to the development of increasingly capable computational methods together with the growth in available computational power in recent decades. While the theory based on Maxwell's equations is highly descriptive of electromagnetic phenomena, there are few problems which can be computed analytically. For this reason, computational methods are indispensable to the modern electromagnetic designer. Computational methods in electromagnetics can be organized in many different ways. One common way to group them is by their theoretical accuracy, which results in the grouping into full wave solvers and asymptotic solvers. Full wave solvers attempt to solve electromagnetic problems without any approximations to Maxwell's equations themselves. This should not be confused with exact solutions as approximations do appear in later stages. Asymptotic solvers, on the other hand, approximate the equations to be solved as the first step and, as a result, they can become computationally more efficient compared to full wave solvers. However, they can only be used if the original assumptions behind the approximations hold.

While asymptotic solvers have very clear cases where the original assumptions break down, it is important to remember that all computational methods have limitations. With full wave solvers it can be easy to think that the solution should be accurate regardless of what electromagnetic problem it is applied to. As will be seen in this section, there are still many approximations that are done in full wave solvers. An example of this is the very step of generating a mesh for a problem geometry, which is an important step in many computational methods. This can be seen as an approximation of the original geometry, but in a way it is rather a replacement of one geometry by another. A typical idea in numerical methods is that increasingly small mesh elements should result in a numerical solution converging to the actual solution. This, however, is not always the case. Many of the most useful computational methods in electromagnetics suffer from the so-called low-frequency breakdown if the mesh size becomes too small. If, in the original problem, Maxwell's equations were considered at a high frequency for the problem size, the selected method may seem very suitable. After meshing, however, Maxwell's equations should be considered for each mesh element, which is essentially a different problem. For very small mesh elements, Maxwell's equations behave in a very different way, closer to electro- and magnetostatics, and this is the basic issue which causes the low-frequency breakdown [32]. Of course, there are remedies to this problem, but its existence is a good reminder that even full wave solvers are not universally applicable without considering the basic assumptions.

When implementing a computational method, another element of uncertainty enters in the form of errors and bugs in the implementation. To ensure that solutions are accurate, verification is crucial. This can take on many different forms, from verification of individual subroutines to comparison of full solutions

to benchmark solutions. Ideally, verification should take place at every level of the computational code, but at the end it is the comparison of full solutions that is most often used to convince others that the code is accurate. The most common example for this is likely the solution of scattering by a sphere, where a comparison can be made to the analytical Mie solution. However, this is not without its drawbacks, as there can be errors in a code which are not visible for that particular problem. Confidence in the accuracy of a particular code should increase with the number of correctly computed benchmark solutions, and a single sphere should not be sufficient for generalizing that a code is correct for all problems. The benchmark which is offered by the Mie solution should not be ignored though, as it provides an excellent first benchmark which is easy to obtain.

In this dissertation, the focus of computational methods is on full wave solvers, with the finite element method (FEM), the method of moments (MoM) and the finite element-boundary integral (FE-BI) method which is a hybrid combining the two. The FE-BI method is implemented in the FE2MS computational code described in Paper I and used in Papers II and III, and the theoretical background to that code is given in this section. The code uses not only FE-BI, but also the adaptive cross approximation (ACA) which is introduced here. Furthermore, Paper IV presents an imaging method with similarities to MoM, and an acceleration method for matrix-vector products which is introduced in this section. The topic of computational methods is, of course, very large and this section focuses only on the methods important to the rest of this dissertation. For a more general overview, the reader is directed to some of the many textbooks on the topic [35, 71, 120].

3.1   The Finite Element Method

The finite element method (FEM) is a versatile computational method which has seen use in a wide range of applications for different branches of physics. It is a method which solves PDEs with suitable boundary conditions using the idea of a subdivision of the computational domain into finite elements: small, regularly shaped subdomains where the solution can be approximated to be on a simple form, typically based on polynomial functions [21, 38]. The subdivided geometry is called a mesh, with individual subdomains called mesh elements, and the functions for approximating the solution called basis functions. The mathematical foundation of FEM rests on calculus of variations and the problem of minimizing functionals, which in physical terms corresponds to minimizing the energy of a particular solution [38]. The variational formulation which is central to this requires the PDE to be reformulated on a weak form which takes into account both the function corresponding to the unknown, and a test function [21]. An alternative, but equivalent, way to motivate a FEM formulation is using the weighted residual method. Typically, this introduces the expansion in basis functions at an earlier stage, and the derivations are generally more direct than using calculus

of variations [35, 71]. For a PDE, the typical procedure for obtaining its weak form is multiplication of the equation by a test function, integration over the full domain, and integration by parts [38].

In electromagnetics, FEM is typically used to solve a PDE similar to (2.20) (possibly with other constitutive relations) for either the electric field $\boldsymbol{E}$ or the magnetic field $\boldsymbol{H}$. The way the weak form is discretized, material parameters are local to the finite elements, which makes FEM particularly suitable to problems that are highly inhomogeneous. As shown in the following parts of this section, it is also possible to use very general constitutive relations in FEM, although the weak forms do change. If there is no magnetoelectric coupling, the corresponding parameters in the constitutive relations (2.30)–(2.31) are $\overline{\overline{\xi}} = \overline{\overline{\zeta}} = \overline{\overline{0}}$. If these relations are inserted in Maxwell's equations (2.15)–(2.16), we obtain

$$\nabla \times \boldsymbol{E} = -\mathrm{j}\omega\mu_0\overline{\overline{\mu_\mathrm{r}}} \cdot \boldsymbol{H} \tag{3.1}$$

$$\nabla \times \boldsymbol{H} = \boldsymbol{J} + \mathrm{j}\omega\varepsilon_0\overline{\overline{\varepsilon_\mathrm{r}}} \cdot \boldsymbol{E}. \tag{3.2}$$

By taking the curl of the first equation, they can be combined into a vector wave equation on the form

$$\nabla \times \left(\overline{\overline{\mu_\mathrm{r}}}^{-1} \cdot \nabla \times \boldsymbol{E}\right) - k_0^2\overline{\overline{\varepsilon_\mathrm{r}}} \cdot \boldsymbol{E} = -\mathrm{j}k_0\eta_0\boldsymbol{J}. \tag{3.3}$$

A weak form based on this equation can be written as (see A.1 for details)

$$\int_\Omega \left[(\nabla \times \boldsymbol{W}_m) \cdot \left(\overline{\overline{\mu_\mathrm{r}}}^{-1} \cdot \nabla \times \boldsymbol{E}\right) - k_0^2\boldsymbol{W}_m \cdot \overline{\overline{\varepsilon_\mathrm{r}}} \cdot \boldsymbol{E} \right] \mathrm{d}V$$

$$+ \oint_{\partial\Omega} \boldsymbol{W}_m \cdot \left[\hat{\boldsymbol{n}} \times \left(\overline{\overline{\mu_\mathrm{r}}}^{-1} \cdot \nabla \times \boldsymbol{E}\right)\right] \mathrm{d}S = -\mathrm{j}k_0\eta_0 \int_\Omega \boldsymbol{W}_m \cdot \boldsymbol{J}\,\mathrm{d}V. \tag{3.4}$$

In the case where full magnetoelectric coupling is considered, the situation is more complicated. Inserting the full constitutive relations (2.30)–(2.31) in Maxwell's equations (2.15)–(2.16) gives

$$\nabla \times \boldsymbol{E} = -\mathrm{j}\omega\mu_0 \left(\frac{1}{\eta_0}\overline{\overline{\zeta}} \cdot \boldsymbol{E} + \overline{\overline{\mu_\mathrm{r}}} \cdot \boldsymbol{H} \right) \tag{3.5}$$

$$\nabla \times \boldsymbol{H} = \boldsymbol{J} + \mathrm{j}\omega\varepsilon_0 \left(\overline{\overline{\varepsilon_\mathrm{r}}} \cdot \boldsymbol{E} + \eta_0\overline{\overline{\xi}} \cdot \boldsymbol{H} \right). \tag{3.6}$$

These can be combined into one equation (see A.2 for details)

$$\nabla \times \left(\overline{\overline{\mu_\mathrm{r}}}^{-1} \cdot \nabla \times \boldsymbol{E}\right) - k_0^2 \left(\overline{\overline{\varepsilon_\mathrm{r}}} - \overline{\overline{\xi}} \cdot \overline{\overline{\mu_\mathrm{r}}}^{-1} \cdot \overline{\overline{\zeta}} \right) \cdot \boldsymbol{E}$$

$$+ \mathrm{j}k_0 \left[\nabla \times \left(\overline{\overline{\mu_\mathrm{r}}}^{-1} \cdot \overline{\overline{\zeta}} \cdot \boldsymbol{E}\right) - \overline{\overline{\xi}} \cdot \overline{\overline{\mu_\mathrm{r}}}^{-1} \cdot \nabla \times \boldsymbol{E} \right] = -\mathrm{j}k_0\eta_0\boldsymbol{J} \tag{3.7}$$

and a corresponding weak form

$$\int_\Omega (\nabla \times \boldsymbol{W}_m) \cdot \left(\overline{\overline{\mu_{\mathrm{r}}}}^{-1} \cdot \nabla \times \boldsymbol{E}\right) \mathrm{d}V - k_0^2 \int_\Omega \boldsymbol{W}_m \cdot \left(\overline{\overline{\varepsilon_{\mathrm{r}}}} - \overline{\overline{\xi}} \cdot \overline{\overline{\mu_{\mathrm{r}}}}^{-1} \cdot \overline{\overline{\zeta}}\right) \cdot \boldsymbol{E} \, \mathrm{d}V$$

$$+ \mathrm{j}k_0 \int_\Omega (\nabla \times \boldsymbol{W}_m) \cdot \overline{\overline{\mu_{\mathrm{r}}}}^{-1} \cdot \overline{\overline{\zeta}} \cdot \boldsymbol{E} \, \mathrm{d}V - \mathrm{j}k_0 \int_\Omega \boldsymbol{W}_m \cdot \left(\overline{\overline{\xi}} \cdot \overline{\overline{\mu_{\mathrm{r}}}}^{-1} \cdot \nabla \times \boldsymbol{E}\right) \mathrm{d}V$$

$$+ \oint_{\partial\Omega} \boldsymbol{W}_m \cdot \left[\hat{\boldsymbol{n}} \times \left(\overline{\overline{\mu_{\mathrm{r}}}}^{-1} \cdot \nabla \times \boldsymbol{E}\right)\right] \mathrm{d}S - \mathrm{j}k_0 \oint_{\partial\Omega} \hat{\boldsymbol{n}} \cdot \left[\boldsymbol{W}_m \times \left(\overline{\overline{\mu_{\mathrm{r}}}}^{-1} \cdot \overline{\overline{\zeta}} \cdot \boldsymbol{E}\right)\right] \mathrm{d}S$$

$$= -\mathrm{j}k_0\eta_0 \int_\Omega \boldsymbol{W}_m \cdot \boldsymbol{J} \, \mathrm{d}V. \quad (3.8)$$

In general, the PDE that FEM is solving needs suitable boundary conditions to be well posed. In the previous sections these have not been considered and as such, the weak forms in (3.4) and (3.8) cannot be expected to be used as they are. Modification of the weak forms would be necessary, and this depends on the type of boundary condition used. Additionally, there could be different boundary conditions on different parts of the boundary $\partial\Omega$ which further affects the weak forms. The PEC boundary condition defined in (2.52)–(2.55) is one of the most useful boundary conditions in practical applications due to the ubiquity of conducting materials. In the electric field FEM formulation used here, it is simple to define using only (2.52) which sets the tangential electric field to zero on the PEC boundary. With some of the most common FEM basis functions this is simple to implement as it only corresponds to setting certain unknowns to zero [72].

Another type of boundary condition which is important is the class of absorbing boundary conditions. As FEM requires the full computational domain to be discretized, simulations with open boundaries, as in typical scattering, pose a problem. Absorbing boundary conditions aim to solve this by, ideally, being formulated such that all waves approaching such a boundary are absorbed perfectly. This emulates an open boundary where the wave propagates to infinity without further interactions. Many absorbing boundary conditions are based on enforcing a radiation condition at the boundary such that waves are absorbed at normal incidence, but reflected at oblique angles. To avoid reflections it can be necessary to place the boundary at a large distance from the simulated object, increasing the number of unknowns [71]. Another type of absorbing boundary condition is the perfectly matched layer (PML), which is technically not a boundary condition but rather an anisotropic medium specially designed to absorb waves that enter [71, 147]. This medium is placed as a layer surrounding the computational domain sufficiently thick to absorb all waves before they reach the outer boundary, at which a PEC boundary condition is often used [71]. One important consideration for all absorbing boundary conditions is the shape of the object to be simulated. Since all waves are absorbed at such a boundary it is critical that it is not placed in a way that interferes with the object. One example of this is shown in Figure 9 where an object exhibiting multiple reflections is shown with absorbing boundary conditions placed differently. To ensure that all characteristics of an object are captured, absorbing boundary conditions can often not be placed conformal to the object. In some cases, like for highly concave objects,
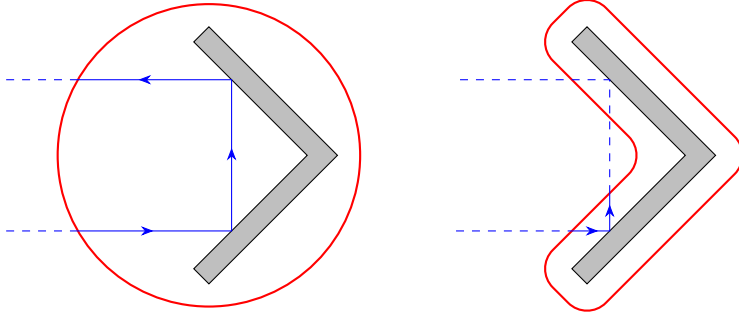
Figure 9: Object exhibiting multiple reflection with absorbing boundary condition (red) placed such that an incident wave (blue) is reflected correctly (left) or is absorbed prematurely (right).

this can lead to a large number of additional unknowns in the FEM problem. This is one of the reasons why other methods like the FE-BI method can be of interest, as will be discussed in section 3.3.

3.2   The Method of Moments

The method of moments (MoM), or boundary element method as it is commonly known outside of electromagnetics, is a computational method based on integral equations. For electromagnetics, this often means either of, or a combination of, the EFIE (2.84) and the MFIE (2.85). It has similarities to FEM, but where FEM is based on a PDE, the integral equations which MoM is based on lead to different characteristics. In FEM, the field solution is directly given by the unknown of the problem, for example $\boldsymbol{E}$ in the PDE (3.3), and is intrinsically linked to the discretization. To determine the solution in a larger region, that region needs to be discretized. In MoM, on the other hand, the solution to the integral equation is typically electric and magnetic currents, and $\boldsymbol{E}$ can be computed from these in arbitrary points of space using (2.79).

One of the most common uses of MoM is for problems involving PEC objects using the EFIE. As discussed in section 2.3, PEC objects only support electric currents and charges. The EFIE in (2.84) is then simplified to

$$\hat{\boldsymbol{n}} \times \mathscr{L}(\bar{\boldsymbol{J}}_{\mathrm{s}})(\boldsymbol{r}) = \hat{\boldsymbol{n}} \times \boldsymbol{E}^{\mathrm{inc}}(\boldsymbol{r}) \tag{3.9}$$

for $\boldsymbol{r}$ on a closed PEC surface $\partial\Omega$. In fact, this equation is valid even for open surfaces despite the fact that the EFIE is typically derived only for closed surfaces [32], and for this reason the surface is denoted S in the following. To solve this problem, the unknown current $\bar{\boldsymbol{J}}_{\mathrm{s}}$ is expanded in a finite set of N basis functions, which could be global or local functions on the surface S. This gives a
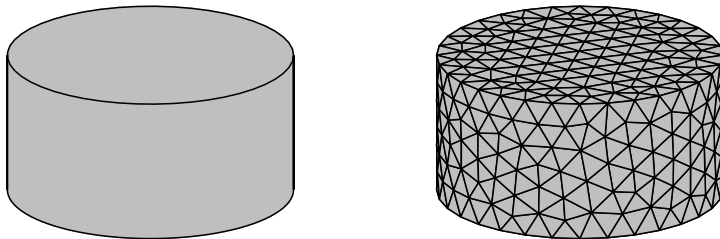
Figure 10: A surface and its triangular mesh representation.

representation

$$\bar{\boldsymbol{J}}_\text{s} = \sum_{n=0}^{N-1} \boldsymbol{\Lambda}_n(\boldsymbol{r})I_n \tag{3.10}$$

where $\boldsymbol{\Lambda}_n$ are basis functions and I_n unknown coefficients. Most commonly, local basis functions are used on a triangular mesh which approximates the surface as shown in Figure 10. The most commonly used basis functions are the linear Rao-Wilton-Glisson (RWG) basis functions [112] which are defined on pairs of triangles sharing an edge in triangular meshes. Expansion in basis functions is not sufficient for a unique solution though, as there will be N unknown coefficients and only one equation.

Furthermore, the discretization introduces an error (residual) due to the finite number of basis functions. The weighted residual method is used to produce a linear system while minimizing the errors introduced by the discretization. The way this is done is by introducing a set of test functions $\boldsymbol{T}_m$ and taking the inner product of these and the discretized equation of interest, in this case (3.9) with the expansion of unknowns in (3.10). The test functions can then be selected to minimize the error after inner product by the discretized equation. If the test functions are selected to be orthogonal to the residual, this error will be eliminated. This is the goal of the Galerkin method [21], typically leading to test functions being the same as the basis functions [32]. In this case it means $\boldsymbol{T}_m = \boldsymbol{\Lambda}_m$ which gives a linear system on the form [32]

$$\boldsymbol{Z}\boldsymbol{I} = \boldsymbol{V} \tag{3.11}$$

with

$$
\begin{aligned}
Z_{mn} &= \int_S \boldsymbol{\Lambda}_m(\boldsymbol{r}) \cdot \mathscr{L}(\boldsymbol{\Lambda}_n)(\boldsymbol{r}) \, \mathrm{d}S \\
&= \mathrm{j}k_0 \int_S \boldsymbol{\Lambda}_m(\boldsymbol{r}) \cdot \int_S \left[\boldsymbol{\Lambda}_n(\boldsymbol{r}')G_0(\boldsymbol{r},\boldsymbol{r}') + \frac{1}{k_0^2}\nabla' \cdot \boldsymbol{\Lambda}_n(\boldsymbol{r}')\nabla G_0(\boldsymbol{r},\boldsymbol{r}') \right] \mathrm{d}S' \, \mathrm{d}S
\end{aligned}
\tag{3.12}
$$

and

$$V_m = \int_S \boldsymbol{\Lambda}_m(\boldsymbol{r}) \cdot \boldsymbol{E}^\text{inc}(\boldsymbol{r}) \, \mathrm{d}S \tag{3.13}$$

where the $\hat{\boldsymbol{n}}\times$ operations originally in (3.9) were removed by noting that it is sufficient that the left- and right-hand sides of (3.9) are tangential to the PEC surface. After scalar products of this equation by tangential test functions, the resulting Z_{mn} and V_m are the same regardless of whether the terms in (3.9) are tangential or not.

The integrals making up the entries of $\mathbf{Z}$ are generally not possible to compute analytically (as opposed to many FEM integrals), and some numerical quadrature is typically performed to obtain the matrix entries [35, 71]. One issue stemming from the Galerkin testing is that some entries of $\mathbf{Z}$ become singular. This comes from the fact that if both $\boldsymbol{\Lambda}_m$ and $\boldsymbol{\Lambda}_n$ are nonzero on a mesh triangle, the inner integral will cover $\boldsymbol{r} = \boldsymbol{r}'$ where the Green's function is singular. One aspect of this singularity was handled in section 2.7, but that was only for the inner operator before Galerkin testing was introduced. It is possible to alter the testing and quadrature procedure such that $\boldsymbol{r} = \boldsymbol{r}'$ never occurs [35, 86], but other methods are typically more accurate [35]. Such methods include singularity subtraction which subtracts a singular part of the integrand that can be solved analytically [8, 40, 48], and singularity cancellation which introduces a coordinate transformation where the singularity is canceled out [39, 75]. For better accuracy, it is also necessary to consider the outer (test) integral when the basis and testing mesh elements are the same or adjacent [106, 108, 109, 150].

While the EFIE and MFIE are widely used in MoM, theory predicts a number of issues with them, with one of the more well known being the issue of interior resonances [32]. The effect of this issue is that the solution to the aforementioned integral equations become inaccurate at certain frequencies. To explain this, it is useful to look at the equivalence theorem while exchanging the volumes being the interior and exterior. If we let the fields be zero for $\boldsymbol{r} \notin \Omega$ in the right-hand sides of (2.82) and (2.83), the problem becomes that of a resonance cavity shaped as Ω with PEC at $\partial\Omega$. At precisely the resonance frequencies of this cavity, the problem of interior resonances will occur for the integral equations as the cavity solution is a valid solution to the equation. Mathematically, this means that there is a null-space of the EFIE/MFIE operator at these frequencies, which causes both issues with inaccurate solutions and an ill-conditioned problem [32]. The latter occurs for other frequencies near the resonance which is an issue for iterative solutions of the problem (this is further discussed in sections 3.3 and 3.4). A common way to remove the issue of interior resonances is by combining the EFIE and MFIE into the combined field integral equation (CFIE) [32].

3.3   The Finite Element–Boundary Integral Method

As hinted toward at the end of section 3.1, the hybridization of FEM and MoM could potentially be advantageous in certain situations, and a commonly used name for such a hybrid method is the finite element-boundary integral (FE-BI) method. The discussions on FEM and MoM by themselves have revealed some

ways the methods complement each other. While FEM is well-suited toward computations involving highly inhomogeneous or even complex media, this is much more difficult and computationally expensive in MoM where it typically requires a volumetric formulation instead of surface formulations similar to that in section 3.2. On the other hand, FEM has several difficulties when it comes to problems involving free space where absorbing boundary conditions need to be used and concave geometries can lead to a large number of unknowns, while the integral equations in MoM inherently handle free space outside the discretized region. These differences and the ways in which the methods complement each other were understood early in the development of FEM and MoM, and hybrid methods have a long history. Very early work on such hybrid methods was done for other types of problems than the electromagnetic wave problems of this dissertation, like scalar potential problems [90, 133]. For the electromagnetic wave problems considered here, the FE-BI method was first introduced as a way to implement free-space boundaries in FEM since modern absorbing boundary conditions like PML were not yet developed. Early methods for doing this included coupling FEM with spherical meshes to spherical harmonics at the free-space boundary [92, 96]. One of the earliest papers mentioning the term "finite element-boundary integral" for electromagnetic wave problems is actually related to a method based on spherical vector harmonics in the boundary integral part, and differs significantly from later methods which use the term [97]. Hybrid methods similar to the one described in this dissertation were later developed for wave propagation in tissue for medical applications [102], and for scattering more generally [70, 165, 166]. As new and faster methods for solving integral equations have been developed, they have typically also been employed for the BI part of the FE-BI method [49, 130, 154, 156]. As will be discussed later in this dissertation, the BI part of the hybrid method dominates in memory use, and as such it is the most important part to make more efficient. While much of the work in FE-BI methods was conducted in the 1990s, there are still developments up to this day. An important topic to handle is the ill-conditioned nature of the FE-BI system matrix. Work related to this includes developing better preconditioners [87, 160], ans alternative solution strategies using domain decomposition [10, 50, 161, 162] or $\mathcal{H}$-matrices [156].

In this section, the formulation of the FE-BI method used in the FE2MS computational code (discussed in Paper I) is introduced. The description roughly follows that in [71, 72], but with some differences and emphasis added to parts where it is important for understanding the work in this thesis. The FE-BI method as discussed in this dissertation uses FEM inside of a volume Ω with a weak form suitable for the media inside. A sketch of this geometry is seen in Figure 11 where it is seen that Ω can contain bianisotropic media, PEC, and current sources. Outside of Ω the medium is free space, though that could be changed to another isotropic medium, and there can be an incident wave. On the boundary $\partial\Omega$, an integral equation is used, for example the EFIE in (2.84). This means that the boundary condition on $\partial\Omega$ is not explicitly known, and instead a boundary condition enforcing Maxwell's equations, or more specifically, Faraday's
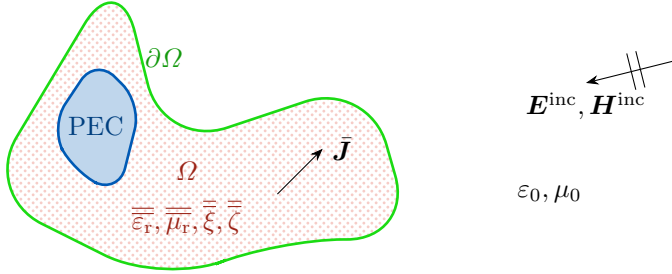
Figure 11: Problem geometry for the FE-BI method.

law is used. That is, a boundary condition equivalent to (2.15) written as

$$\hat{\boldsymbol{n}} \times \left(\overline{\overline{\mu_{\mathrm{r}}}}^{-1} \cdot \nabla \times \boldsymbol{E}\right) = -\mathrm{j}k_0 \hat{\boldsymbol{n}} \times \bar{\boldsymbol{H}}, \; \boldsymbol{r} \in \partial\Omega \qquad (3.14)$$

where the scaling of the magnetic field $\bar{\boldsymbol{H}} = \eta_0 \boldsymbol{H}$ and the electric current $\bar{\boldsymbol{J}} = \eta_0 \boldsymbol{J}$ that was used when introducing MoM is now extended to FEM parts. This condition is inserted in the weak forms, giving

$$\int_{\Omega} \left[(\nabla \times \boldsymbol{W}_m) \cdot \left(\overline{\overline{\mu_{\mathrm{r}}}}^{-1} \cdot \nabla \times \boldsymbol{E}\right) - k_0^2 \boldsymbol{W}_m \cdot \overline{\overline{\varepsilon_{\mathrm{r}}}} \cdot \boldsymbol{E} \right] \mathrm{d}V$$
$$+ \mathrm{j}k_0 \oint_{\partial\Omega} \hat{\boldsymbol{n}} \cdot \left(\boldsymbol{W}_m \times \bar{\boldsymbol{H}}\right) \mathrm{d}S = -\mathrm{j}k_0 \int_{\Omega} \boldsymbol{W}_m \cdot \bar{\boldsymbol{J}} \, \mathrm{d}V \quad (3.15)$$

for media without magnetoelectric coupling and

$$\int_{\Omega} (\nabla \times \boldsymbol{W}_m) \cdot \left(\overline{\overline{\mu_{\mathrm{r}}}}^{-1} \cdot \nabla \times \boldsymbol{E}\right) \mathrm{d}V - k_0^2 \int_{\Omega} \boldsymbol{W}_m \cdot \left(\overline{\overline{\varepsilon_{\mathrm{r}}}} - \overline{\overline{\xi}} \cdot \overline{\overline{\mu_{\mathrm{r}}}}^{-1} \cdot \overline{\overline{\zeta}}\right) \boldsymbol{E} \, \mathrm{d}V$$
$$+ \mathrm{j}k_0 \int_{\Omega} (\nabla \times \boldsymbol{W}_m) \cdot \overline{\overline{\mu_{\mathrm{r}}}}^{-1} \cdot \overline{\overline{\zeta}} \cdot \boldsymbol{E} \, \mathrm{d}V - \mathrm{j}k_0 \int_{\Omega} \boldsymbol{W}_m \cdot \left(\overline{\overline{\xi}} \cdot \overline{\overline{\mu_{\mathrm{r}}}}^{-1} \cdot \nabla \times \boldsymbol{E}\right) \mathrm{d}V$$
$$+ \mathrm{j}k_0 \oint_{\partial\Omega} \hat{\boldsymbol{n}} \cdot \left(\boldsymbol{W}_m \times \bar{\boldsymbol{H}}\right) \mathrm{d}S = -\mathrm{j}k_0 \int_{\Omega} \boldsymbol{W}_m \cdot \bar{\boldsymbol{J}} \, \mathrm{d}V \quad (3.16)$$

for media with magnetoelectric coupling (see A.1–A.2 for details). These weak forms contain two unknown fields $\boldsymbol{E}$ and $\bar{\boldsymbol{H}}$ on $\partial\Omega$ which are connected using an integral equation. When this connection is to be made, the unknowns need to be related to each other. In the FE part, the unknowns are the fields $\boldsymbol{E}$ and $\bar{\boldsymbol{H}}$ while in BI part they are the currents $\bar{\boldsymbol{J}}$ and $\boldsymbol{M}$. Using the surface equivalence theorem with the zero field condition in (2.74) and (2.75), these are related as $\bar{\boldsymbol{J}}_{\mathrm{s}} = \hat{\boldsymbol{n}} \times \bar{\boldsymbol{H}}$ and $\boldsymbol{M}_{\mathrm{s}} = \boldsymbol{E} \times \hat{\boldsymbol{n}}$. The use of the zero field equivalence theorem means that standard free space integral equations can be used to give the true solution without special regard to the medium inside Ω.
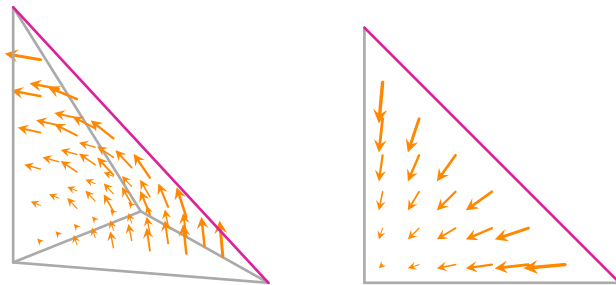
Figure 12: Basis functions used in the FE (left) and BI (right) parts. The triangle to the right is the same as the front face of the tetrahedron to the left. Adapted from [128] (CC-BY-4.0).

3.3.1   Basis Functions

Next, the solution in both FEM and MoM rests upon expanding the unknowns into a discrete set of basis functions, which means that they also need to be connected. In the FE part, the expansion uses curl-conforming basis functions $\boldsymbol{N}$, meaning that the functions are defined such that $\nabla \times \boldsymbol{N}$ is square integrable [46]. In the BI part, the expansion uses divergence-conforming basis functions $\boldsymbol{\Lambda}$, which instead are such that $\nabla \cdot \boldsymbol{\Lambda}$ is square integrable [46]. Essentially, the curl or divergence of such basis functions will not contain Dirac delta functions, making them suitable in expressions with curl or divergence (like the FE or BI expressions). Figure 12 shows an example of a lowest order Nédélec curl-conforming basis function on a tetrahedron and a lowest order Raviart-Thomas divergence-conforming basis function on a triangle (equivalent to RWG functions but often defined with a different normalization). As these are linear functions, the curl-or divergence-conforming property means that $\nabla \times \boldsymbol{N}$ or $\nabla \cdot \boldsymbol{\Lambda}$ is constant. Both types of basis functions are so called edge based, meaning that they are linked to edges in the mesh, as can be seen for the basis functions in Figure 12 which are linked to the highlighted edges. If the FE unknowns $\boldsymbol{E}$ and $\bar{\boldsymbol{H}}$ are expanded using curl-conforming basis functions, they can be written as

$$\boldsymbol{E}(\boldsymbol{r}) = \sum_{n=0}^{N_\mathrm{I}-1} \boldsymbol{N}_n^\mathrm{I}(\boldsymbol{r}) E_n^\mathrm{I} + \sum_{n=0}^{N_\mathrm{S}-1} \boldsymbol{N}_n^\mathrm{S}(\boldsymbol{r}) E_n^\mathrm{S} \tag{3.17}$$

$$\bar{\boldsymbol{H}}(\boldsymbol{r}) = \sum_{n=0}^{N_\mathrm{S}-1} \boldsymbol{N}_n^\mathrm{S}(\boldsymbol{r}) \bar{H}_n^\mathrm{S} \tag{3.18}$$

where N_I is the number of mesh edges on the interior of Ω and N_S is the number of mesh edges on the external boundary $\partial\Omega$. The superscripts I and S similarly indicate whether a basis function and its corresponding degree of freedom are based on an interior or boundary edge, respectively. If the BI unknowns $\bar{\boldsymbol{J}}_\mathrm{s}$ and $\boldsymbol{M}_\mathrm{s}$ are to be expanded in basis functions, it is important that they can be connected to the FE expansions. This is quite naturally done though, as a curl-

conforming basis function transforms into a divergence-conforming one under the rotation around a surface normal. This means that a suitable expansion is obtained for $\boldsymbol{r} \in \partial\Omega$ as

$$\bar{\boldsymbol{J}}_{\mathrm{s}}(\boldsymbol{r}) = \hat{\boldsymbol{n}} \times \bar{\boldsymbol{H}}(\boldsymbol{r}) = \sum_{n=0}^{N_{\mathrm{S}}-1} \left(\hat{\boldsymbol{n}} \times \boldsymbol{N}_n^{\mathrm{S}}(\boldsymbol{r})\right) \bar{H}_n^{\mathrm{S}} = \sum_{n=0}^{N_{\mathrm{S}}-1} \boldsymbol{\Lambda}_n(\boldsymbol{r}) \bar{H}_n^{\mathrm{S}} \tag{3.19}$$

$$\boldsymbol{M}_{\mathrm{s}}(\boldsymbol{r}) = \boldsymbol{E}(\boldsymbol{r}) \times \hat{\boldsymbol{n}} = -\sum_{n=0}^{N_{\mathrm{S}}-1} \left(\hat{\boldsymbol{n}} \times \boldsymbol{N}_n^{\mathrm{S}}(\boldsymbol{r})\right) E_n^{\mathrm{S}} = -\sum_{n=0}^{N_{\mathrm{S}}-1} \boldsymbol{\Lambda}_n(\boldsymbol{r}) E_n^{\mathrm{S}} \tag{3.20}$$

with the derived divergence-conforming basis functions $\boldsymbol{\Lambda}_n$. If $\boldsymbol{N}_n$ is a lowest order Nédélec basis function on a tetrahedron, the derived $\boldsymbol{\Lambda}_n$ is a lowest order Raviart-Thomas basis function on a triangle. By careful inspection of figure 12, it can be seen that the Raviart-Thomas function is obtained by rotating the Nédélec function 90° around the facet normal.

3.3.2 Finite Element Matrix Blocks

The finite element formulations can be separated into integrals involving $\boldsymbol{E}$ and integrals involving $\bar{\boldsymbol{H}}$. The expansions in (3.17) and (3.18) are used, and the test functions $\boldsymbol{W}_m$ in the weak forms are set to be equal to the basis functions. For media without magnetoelectric coupling, using the $\boldsymbol{E}$ integrals of the weak form in (3.15) results in a matrix $\mathbf{K}$ with entries

$$K_{mn}^{\mathrm{XY}} = \int_{\Omega} \left[(\nabla \times \boldsymbol{N}_m^{\mathrm{X}}) \cdot \left(\overline{\overline{\mu_{\mathrm{r}}}}^{-1} \cdot \nabla \times \boldsymbol{N}_m^{\mathrm{Y}}\right) - k_0^2 \boldsymbol{N}_m^{\mathrm{X}} \cdot \overline{\overline{\varepsilon_{\mathrm{r}}}} \cdot \boldsymbol{N}_m^{\mathrm{Y}} \right] \mathrm{d}V \tag{3.21}$$

where $\mathrm{X}, \mathrm{Y} \in \{\mathrm{I}, \mathrm{S}\}$ indicate if corresponding unknowns are on the interior of Ω or on the external boundary $\partial\Omega$. For media with magnetoelectric coupling as the weak form in (3.16), the matrix entries instead become

$$K_{mn}^{\mathrm{XY}} =$$
$$\int_{\Omega} (\nabla \times \boldsymbol{N}_m^{\mathrm{X}}) \cdot \left(\overline{\overline{\mu_{\mathrm{r}}}}^{-1} \cdot \nabla \times \boldsymbol{N}_m^{\mathrm{Y}}\right) \mathrm{d}V - k_0^2 \int_{\Omega} \boldsymbol{N}_m^{\mathrm{X}} \cdot \left(\overline{\overline{\varepsilon_{\mathrm{r}}}} - \overline{\overline{\xi}} \cdot \overline{\overline{\mu_{\mathrm{r}}}}^{-1} \cdot \overline{\overline{\zeta}}\right) \cdot \boldsymbol{N}_m^{\mathrm{Y}} \mathrm{d}V$$
$$+ \mathrm{j}k_0 \int_{\Omega} (\nabla \times \boldsymbol{N}_m^{\mathrm{X}}) \cdot \overline{\overline{\mu_{\mathrm{r}}}}^{-1} \cdot \overline{\overline{\zeta}} \cdot \boldsymbol{N}_m^{\mathrm{Y}} \mathrm{d}V - \mathrm{j}k_0 \int_{\Omega} \boldsymbol{N}_m^{\mathrm{X}} \cdot \left(\overline{\overline{\xi}} \cdot \overline{\overline{\mu_{\mathrm{r}}}}^{-1} \cdot \nabla \times \boldsymbol{N}_m^{\mathrm{Y}}\right) \mathrm{d}V. \tag{3.22}$$

The integrals involving $\bar{\boldsymbol{H}}$ are the same for both types of media, resulting in a matrix $\mathbf{B}$ with entries

$$B_{mn} = \mathrm{j}k_0 \oint_{\partial\Omega} \hat{\boldsymbol{n}} \cdot (\boldsymbol{N}_m^{\mathrm{S}} \times \boldsymbol{N}_n^{\mathrm{S}}) \, \mathrm{d}S. \tag{3.23}$$

Since this only contains basis functions evaluated on the boundary $\partial\Omega$, it can also be rewritten using divergence-conforming basis functions as

$$B_{mn} = jk_0 \oint_{\partial\Omega} \hat{\boldsymbol{n}} \cdot ([-\hat{\boldsymbol{n}} \times \boldsymbol{\Lambda}_m] \times [-\hat{\boldsymbol{n}} \times \boldsymbol{\Lambda}_n])\, dS = jk_0 \oint_{\partial\Omega} \hat{\boldsymbol{n}} \cdot (\boldsymbol{\Lambda}_m \times \boldsymbol{\Lambda}_n)\, dS. \tag{3.24}$$

The linear system built up by the matrices $\mathbf{K}^{\mathrm{XY}}$ and $\mathbf{B}$ can be expressed as

$$\begin{bmatrix} \mathbf{K}^{\mathrm{II}} & \mathbf{K}^{\mathrm{IS}} & \mathbf{0} \\ \mathbf{K}^{\mathrm{SI}} & \mathbf{K}^{\mathrm{SS}} & \mathbf{B} \end{bmatrix} \begin{pmatrix} \boldsymbol{E}^{\mathrm{I}} \\ \boldsymbol{E}^{\mathrm{S}} \\ \bar{\boldsymbol{H}}^{\mathrm{S}} \end{pmatrix} = \begin{pmatrix} b^{\mathrm{I}} \\ b^{\mathrm{S}} \end{pmatrix}. \tag{3.25}$$

This is underdetermined as the BI part has not yet been accounted for. The entries in the right-hand side are obtained as

$$b_m^{\mathrm{Y}} = -jk_0 \int_{\Omega} \boldsymbol{N}_m^{\mathrm{Y}} \cdot \bar{\boldsymbol{J}}\, dV \tag{3.26}$$

from the right-hand sides of (3.15) and (3.16).

3.3.3   Boundary Integral Matrix Blocks

The BI matrix blocks depend on the integral equation which is used. Starting with the EFIE from (2.84), a cross product by $\hat{\boldsymbol{n}}$ is first used to eliminate all occurrences of $\hat{\boldsymbol{n}}$ (the tangential nature of the equation is preserved since the basis functions $\boldsymbol{\Lambda}$ are tangential to the elements of their support). The expansions for currents in (3.19) and (3.20) are inserted and the equation is tested by the same functions as the basis functions. For test function m, the equation then becomes

$$\sum_{n=0}^{N_{\mathrm{S}}-1} \oint_{\partial\Omega} \boldsymbol{\Lambda}_m(\boldsymbol{r}) \cdot \left(\mathscr{L}\left[\boldsymbol{\Lambda}_n(\boldsymbol{r}')\bar{H}_n^{\mathrm{S}}\right] - \mathscr{K}\left[-\boldsymbol{\Lambda}_n(\boldsymbol{r})E_n^{\mathrm{S}}\right] \right) dS$$
$$= \oint_{\partial\Omega} \boldsymbol{\Lambda}_m(\boldsymbol{r}) \cdot \boldsymbol{E}^{\mathrm{inc}}(\boldsymbol{r})\, dS. \tag{3.27}$$

This gives a linear system on the form

$$\mathbf{P}\boldsymbol{E}^{\mathrm{S}} + \mathbf{Q}\bar{\boldsymbol{H}}^{\mathrm{S}} = \boldsymbol{b}^{\mathrm{inc}} \tag{3.28}$$

with entries given by

$$P_{mn} = P_{mn}^{\mathrm{E}} = \oint_{\partial\Omega} \boldsymbol{\Lambda}_m(\boldsymbol{r}) \cdot \mathscr{K}(\boldsymbol{\Lambda}_n(\boldsymbol{r}'))\, dS \tag{3.29}$$

$$Q_{mn} = Q_{mn}^{\mathrm{E}} = \oint_{\partial\Omega} \boldsymbol{\Lambda}_m(\boldsymbol{r}) \cdot \mathscr{L}(\boldsymbol{\Lambda}_n(\boldsymbol{r}'))\, dS \tag{3.30}$$

$$b_m^{\mathrm{inc}} = b_m^{\mathrm{E}} = \oint_{\partial\Omega} \boldsymbol{\Lambda}_m(\boldsymbol{r}) \cdot \boldsymbol{E}^{\mathrm{inc}}(\boldsymbol{r})\, dS. \tag{3.31}$$

As discussed in section 2.7, the $\mathscr{K}$-operator contains a singularity which gives an additional term when extracted. This term only appears for matrix entries with testing and basis functions within the same mesh triangle. Furthermore, the evaluation of matrix entries is done the same way as discussed for standard MoM in section 3.2, which means that certain entries will be singular and not possible to evaluate by numerical quadrature. Fortunately, the same methods of singularity subtraction and cancellation are also useful in the FE-BI case.

As for standard MoM, the use of the EFIE for closed surfaces like $\partial\Omega$ introduces the known issue of interior resonances. One common way to eliminate this issue is by using the CFIE instead. It is, however, important to test this equation with appropriate test functions for the interior resonance problem to fully disappear. One difficulty comes from the fact that versions of the CFIE which eliminate the interior resonance problem combine the EFIE and the MFIE with one of them having the rotating operation $\hat{\boldsymbol{n}}\times$ applied to it [130]. The suitable test functions for the rotated part of the CFIE are curl-conforming, and not simply the rotated basis functions. Instead, another type of test function, often called Buffa-Christiansen functions, can be used for that part of the CFIE to obtain an appropriately tested equation [7, 23]. These functions have been used to resolve issues with test functions for the MFIE [34], CFIE [163], and CFIE used in the FE-BI method [49].

A difficulty with the approaches using Buffa-Christiansen test functions for the CFIE is that implementations require significant amounts of additional work with such functions being defined on a different mesh. One CFIE formulation which is easy to implement with the exact same tools as for the EFIE formulation is the so called TETH formulation from [130]. This does not have any rotating operations for the EFIE or MFIE, and can use the same test functions as before. However, this formulation does not eliminate the interior resonances which was the main reason for using the CFIE. Nevertheless, it can be used to improve performance with essentially no additional effort compared to an EFIE implementation. If an iterative solver is used to solve a problem with interior resonances, the solver converges very slowly in a band around the resonance frequencies. With the TETH formulation, this band can be reduced so that solutions can be obtained with reasonable convergence at more frequencies than with the EFIE, although it is still not possible to obtain an accurate solution exactly at the resonance. The **P** and **Q** matrix blocks for the TETH formulation are obtained by linear combination of the ones for the EFIE as [130]
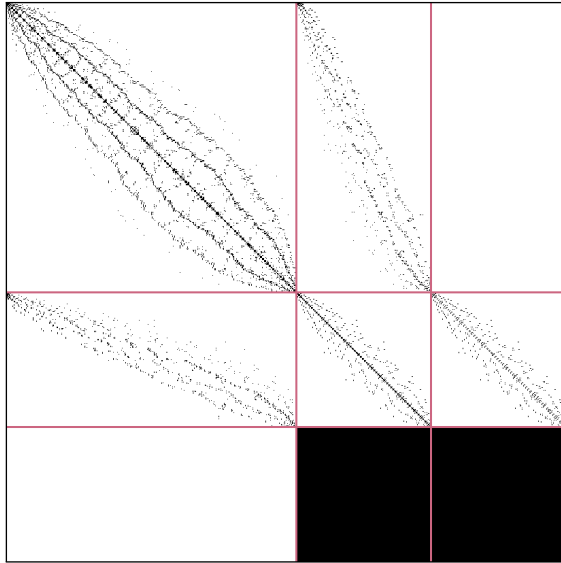
$$P_{mn} = \frac{1}{2}\left(P_{mn}^{\mathrm{E}} - Q_{mn}^{\mathrm{E}}\right) \tag{3.32}$$

$$Q_{mn} = \frac{1}{2}\left(P_{mn}^{\mathrm{E}} + Q_{mn}^{\mathrm{E}}\right) \tag{3.33}$$

$$b_m^{\mathrm{inc}} = \frac{1}{2}\left(b_m^{\mathrm{E}} + b_m^{\mathrm{M}}\right) \tag{3.34}$$

where

$$b_m^{\mathrm{M}} = \oint_{\partial\Omega} \boldsymbol{\Lambda}_m(\boldsymbol{r}) \cdot \bar{\boldsymbol{H}}^{\mathrm{inc}}(\boldsymbol{r})\,\mathrm{d}S. \tag{3.35}$$

Figure 13: Illustration of the nonzero entries of the FE-BI system matrix. Purple lines are used to indicate the block structure.

These are used in the same system as (3.28).

3.3.4 Combined Linear System

When the FE and BI formulations are decided, their linear systems in (3.25) and (3.28) can be combined into the complete FE-BI system

$$
\begin{bmatrix} \mathbf{K}^{\mathrm{II}} & \mathbf{K}^{\mathrm{IS}} & \mathbf{0} \\ \mathbf{K}^{\mathrm{SI}} & \mathbf{K}^{\mathrm{SS}} & \mathbf{B} \\ \mathbf{0} & \mathbf{P} & \mathbf{Q} \end{bmatrix} \begin{pmatrix} \boldsymbol{E}^{\mathrm{I}} \\ \boldsymbol{E}^{\mathrm{S}} \\ \bar{\boldsymbol{H}}^{\mathrm{S}} \end{pmatrix} = \begin{pmatrix} \boldsymbol{b}^{\mathrm{I}} \\ \boldsymbol{b}^{\mathrm{S}} \\ \boldsymbol{b}^{\mathrm{inc}} \end{pmatrix}. \tag{3.36}
$$

For the FE2MS FE-BI code presented and used in papers I–III, only scattering problems are considered, which means that $\boldsymbol{b}^{\mathrm{I}}$ and $\boldsymbol{b}^{\mathrm{S}}$ become zero. The system is partly sparse, and partly dense due to the structure of the FE and BI blocks, respectively. This is illustrated in Figure 13 for a small layered dielectric sphere with 624 FE unknowns and 198 BI unknowns.

3.4 Solution Methods

All computational methods discussed in previous sections result in linear systems of equations that are to be solved. Often, such methods are classified as direct methods or iterative methods.

The oldest direct methods use a complete matrix with all entries, including zeros, directly available. Most Gaussian elimination methods and LU decomposi-

tion methods are included here. While this can be acceptable for dense matrices with few zero entries, such methods are unsuitable for sparse matrices where the majority of matrix entries are zeros. For sparse matrices, there are ways of storage that do not require all zeros to be explicitly stored, meaning large memory compression when implemented. For these types of matrices, there are other direct methods available, often through specific software packages like UMF-PACK [36], SuperLU [83], MUMPS [5]. These are typically much more complex than the methods for full matrices though. Another type of direct method are fast direct methods like $\mathcal{H}$-matrix methods [17, 55]. These use underlying properties of the, typically dense, system matrix to rewrite it on a different form (the ACA method discussed in section 3.5.2 is often used as part of these methods to provide compression). This new form can then be used for a solution which can give a representation like the aforementioned LU decomposition. Similar to the methods for sparse matrices, the fast direct methods are more complex than the methods for full matrices.

Iterative methods work in very different ways compared to direct methods. While direct methods require matrices to have a certain structure, be it dense, sparse or $\mathcal{H}$-matrix, iterative methods require no knowledge of the matrix. They are instead based on matrix-vector products and can be used to solve any system for which such products can be performed. They are called iterative because they use a series of matrix-vector products with different vectors to find a solution for one right-hand side. This means that all of the matrix types described for direct methods can also be used for iterative methods without much work, as matrix-vector products are such essential building blocks for any implementation of linear algebra. It also means that combinations of different matrix types which do not easily work with direct solvers can use iterative methods. This includes the FE-BI system in (3.36) which typically is too sparse to be efficiently solved using methods for dense matrices, but too dense to be efficiently solved by methods for sparse matrices. One drawback of iterative methods compared to direct methods is that an iterative solution is only valid for one right-hand side. Direct methods like LU decomposition result in a matrix representation applicable to any right-hand side with low computational cost. In some cases, if solutions are similar, the performance of iterative methods for multiple right-hand sides can be improved by using the previous solution is as an initial guess. These considerations can be very important for electromagnetic problems with multiple excitations common in, for example, RCS computations.

One major consideration when working with iterative methods is that of convergence. The number of iterations required to solve a system can vary significantly, and depends strongly on the condition number of the matrix. Methods to reduce the condition number, or preconditioning, are highly useful to improve performance. Essentially, such methods aim to transform the system matrix to one with better convergence, and ensure that the result is still correct or can be made so with a simple transformation [121, 144]. In practice, preconditioning is typically not applied to the system matrix though, as that would be computationally expensive. Instead, the vectors in the matrix-vector products of the

iterative method are transformed by the preconditioning, achieving the same effect. Depending on which stage of the iteration the preconditioner is applied, different terms are used. In right preconditioning, the preconditioner is applied to the right of the system matrix, *i.e.*, on the vector going into the matrix-vector product. In left preconditioning, the preconditioner is instead applied to the left of the system matrix, *i.e.*, on the vector resulting from the matrix-vector product. It is also possible to combine the two [121]. There are many different preconditioning methods, some which are more general than others. Methods like Jacobian, successive over-relaxation and incomplete LU decomposition are examples of general-purpose preconditioning methods applicable to many different system matrices [121]. However, better performance is often possible if the preconditioning method is adapted to the system in question. As an example of specialized preconditioning, the FE-BI system in (3.36) based on the EFIE is considered. This system is typically very ill-conditioned and needs a good preconditioner for iterative methods to converge. The method used in the FE2MS FE-BI code described in Paper I (similar to that described in [49]) applies a sparsification procedure to the BI blocks in (3.36) to obtain a new matrix

$$\mathbf{M} = \begin{bmatrix} \mathbf{K}^{\mathrm{II}} & \mathbf{K}^{\mathrm{IS}} & \mathbf{0} \\ \mathbf{K}^{\mathrm{SI}} & \mathbf{K}^{\mathrm{SS}} & \mathbf{B} \\ \mathbf{0} & -2\mathrm{j}k_0\mathbf{P}' & -2\mathrm{j}k_0\mathbf{Q}' \end{bmatrix}. \tag{3.37}$$

The blocks $\mathbf{P}'$ and $\mathbf{Q}'$ are obtained by only considering interactions within single mesh elements, which together with the multiplication by $-\mathrm{j}k_0$ causes $\mathbf{M}$ to be both sparse and symmetric. The preconditioned vector is then obtained by solving the system

$$\mathbf{M}\boldsymbol{x} = \boldsymbol{y} \tag{3.38}$$

where $\boldsymbol{y}$ is the original vector and $\boldsymbol{x}$ the preconditioned vector. This system can be solved directly using efficient methods for sparse systems, or iteratively, though that typically requires another inner preconditioning step.

3.5 Acceleration and Compression Methods

There are many different ways to make computational codes faster, but certain methods exist that use mathematical properties of the underlying computational codes to dramatically improve performance. In this part the focus is going to be on a few methods applicable to the MoM and FE-BI computational methods, but there are many more methods that are not discussed here.

The main reason why MoM and FE-BI are discussed at the same time is that they both share the same bottleneck in performance, which is due to the use of integral equations. In the FE-BI system matrix (3.36), there are both sparse matrices coming from the FE part and dense matrices coming from the BI part. These matrix types have different complexities with regard to memory and computation times as shown in Table 1. The effect of these on the FE-BI

Table 1: Complexities for sparse and dense matrices with n unknowns. C is the number of iterations.

Resource	Sparse	Dense
Matrix storage	$O(n)$	$O(n^2)$
Matrix-vector product time	$O(n)$	$O(n^2)$
Iterative solution time	$O(Cn)$	$O(Cn^2)$

method is that the BI part dominates both in memory and time, even for small problem sizes. It is very beneficial if this complexity can be reduced.

One way of reducing the complexity is by obtaining a representation of the matrix which is significantly compressed as compared to the full matrix, and doing this in a way that is computationally efficient in its construction. Important mathematical operations like matrix-vector products also need to be possible to perform efficiently. Typically, the possibility to compress information indicates that the full representation contains redundant information [129], and this is also the case for the methods described here.

The first method described in section 3.5.1 compresses a matrix by exploiting translation invariance in the underlying operator. This means that the operator remains the same under specific translations in space, meaning that matrix entries are also unchanged for the same translations. Conceptually, it is easy to see that there is redundant information, and compression should be possible. The same properties allowing for compression as described here are also used in other methods like the conjugate gradient-FFT method [29, 104, 124] and the adaptive integral method [19]. The second method described in section 3.5.2 is the ACA which uses low-rank properties to compress a matrix, or sub-blocks of a matrix. The general property of a matrix having low rank means that it can be written using only a subset of its columns. That this allows for compression is also conceptually easy to understand. For both methods, however, the actual ways to obtain compressed representations efficiently and use them in mathematical operations take more work to understand. Of course, many other methods for compression and acceleration exist with one of the more important ones being the fast multipole method [33, 116, 117] in its multilevel implementation [135, 136]. While very important for MoM in general, it is not discussed in detail in this dissertation.

3.5.1 Acceleration of Translation Invariant Operators

This first type of acceleration is based on exploiting properties of the Green's function. Consider the free space Green's function as given by

$$G(\boldsymbol{r}, \boldsymbol{r}') = \frac{\mathrm{e}^{-\mathrm{j}k_0|\boldsymbol{r}-\boldsymbol{r}'|}}{4\pi|\boldsymbol{r}-\boldsymbol{r}'|}. \tag{3.39}$$

If the source and evaluation points $\boldsymbol{r}'$ and $\boldsymbol{r}$ are translated equally, there is no change in the function value, *i.e.*, $G(\boldsymbol{r}-\boldsymbol{r}_\mathrm{t}, \boldsymbol{r}'-\boldsymbol{r}_\mathrm{t}) = G(\boldsymbol{r}, \boldsymbol{r}')$. The Green's

function is translation invariant, which can be used to accelerate matrix-vector products for matrices based on it.

As a simple example, consider a regular rectangular grid with N_x nodes in x and N_y nodes in y such that the node coordinates are

$$\boldsymbol{r}_{m,n} = m\Delta x\hat{\boldsymbol{x}} + n\Delta y\hat{\boldsymbol{y}} \tag{3.40}$$

with grid spacing Δx and Δy. Let an identical grid, but translated in z by z_0, be defined with node coordinates

$$\boldsymbol{r}'_{m,n} = m\Delta x\hat{\boldsymbol{x}} + n\Delta y\hat{\boldsymbol{y}} + z_0\hat{\boldsymbol{z}}. \tag{3.41}$$

The Green's function for source points on one grid and observation points on the other is now expressed in a tensor form as

$$A_{m\,,n}^{m',n'} = G(\boldsymbol{r}_{m,n}, \boldsymbol{r}'_{m',n'}) \tag{3.42}$$

and due to translation invariance in the Green's function, it holds that

$$A_{m\,-m_0,n\,-n_0}^{m'-m_0,n'-n_0} = A_{m\,,n}^{m',n'} \tag{3.43}$$

if m_0 and n_0 are integers such that the resulting indices are not out of bounds for the grid in question. While the Green's function could have been written more traditionally as a two-dimensional matrix, the four-dimensional tensor form makes the translation invariance more explicit.

The way this translation invariance affects the tensor $A_{m\,,n}^{m',n'}$ is similar to how a Toeplitz matrix behaves. Such a matrix with dimensions $N \times N$ is defined to have elements as [47]

$$\mathbf{T} = \begin{bmatrix} T_0 & T_{-1} & T_{-2} & \dots & T_{-(N-1)} \\ T_1 & T_0 & T_{-1} & \dots & T_{-(N-2)} \\ T_2 & T_1 & T_0 & \dots & T_{-(N-3)} \\ \vdots & \vdots & \vdots & \ddots & \vdots \\ T_{N-1} & T_{N-2} & T_{N-3} & \dots & T_0 \end{bmatrix}. \tag{3.44}$$

This type of matrix can be rewritten as a circulant matrix by embedding it in a $2N \times 2N$ matrix as

$$\widetilde{\mathbf{T}} = \left[\begin{array}{cccc|cccc} T_0 & T_{-1} & \dots & T_{-(N-1)} & 0 & T_{N-1} & \dots & T_1 \\ T_1 & T_0 & \dots & T_{-(N-2)} & T_{-(N-1)} & 0 & \dots & T_2 \\ \vdots & \vdots & \ddots & \vdots & \vdots & \vdots & \ddots & \vdots \\ T_{N-1} & T_{N-2} & \dots & T_0 & T_{-1} & T_{-2} & \dots & 0 \\ \hline 0 & T_{N-1} & \dots & T_1 & T_0 & T_{-1} & \dots & T_{-(N-1)} \\ T_{-(N-1)} & 0 & \dots & T_2 & T_1 & T_0 & \dots & T_{-(N-2)} \\ \vdots & \vdots & \ddots & \vdots & \vdots & \vdots & \ddots & \vdots \\ T_{-1} & T_{-2} & \dots & 0 & T_{N-1} & T_{N-2} & \dots & T_0 \end{array} \right] \tag{3.45}$$

where the top left block is the same as $\mathbf{T}$ and the others contain the same entries. Looking at the columns of $\widetilde{\mathbf{T}}$, it is seen that each column is the same as the previous, but shifted one entry down. This means that $\widetilde{\mathbf{T}}$ is circulant, and such a matrix is diagonalized by the discrete Fourier transform (DFT) [47]. This is important as it enables fast matrix-vector products and linear system solution using the fast Fourier transform (FFT). If $\mathbf{F}_n$ is the matrix corresponding to the DFT of dimension n, the diagonalization of $\widetilde{\mathbf{T}}$ can be written as [47, 113]

$$\widetilde{\mathbf{T}} = \mathbf{F}_n^{-1}\mathrm{diag}(\mathbf{F}_n \boldsymbol{t})\mathbf{F}_n \tag{3.46}$$

where $\boldsymbol{t}$ is the first column of $\widetilde{\mathbf{T}}$. A matrix-vector product involving $\widetilde{\mathbf{T}}$ can thus be computed as

$$\widetilde{\mathbf{T}}\boldsymbol{v} = \mathbf{F}_n^{-1}\mathrm{diag}(\mathbf{F}_n \boldsymbol{t})\mathbf{F}_n \boldsymbol{v} = \mathbf{F}_n^{-1}\left(\mathbf{F}_n \boldsymbol{t} \circ \mathbf{F}_n \boldsymbol{v}\right) \tag{3.47}$$

where $\circ$ indicates a Hadamard (elementwise) product. Operations involving $\mathbf{F}_n$ and $\mathbf{F}_n^{-1}$ are computed fast using the FFT. Since $\widetilde{\mathbf{T}}$ contains the original matrix $\mathbf{T}$ in the first N rows and columns, a matrix-vector product $\mathbf{T}\boldsymbol{w}$ is easily obtainable by appending N zeros to $\boldsymbol{w}$, applying (3.47), and extracting the first N entries of the result. Due to the performance of the FFT and the fact that only a vector with $2N$ entries is used, this can dramatically improve performance.

Going back to the original problem with the tensor $A_{m,n}^{m',n'}$, the Topelitz and circulant structures become significantly harder to write out explicitly, but similar acceleration as for matrices is possible for tensors of arbitrary order [113]. In the four-dimensional tensor case of interest here, the acceleration analogous to (3.47) changes from using a one-dimensional DFT operating on vectors to a two-dimensional DFT operating on matrices. Although the generalization is more complicated to write out explicitly and implement in a code, the underlying theory is the same as for the circulant matrices. A different situation arises if the two grids in the Green's function example are changed to only be equal in one instead of two dimensions. That could be due to a curvature preventing translation invariance in one of the two grid dimensions. In this case, translation invariance still exists in one dimension, and with an appropriate formulation of the four-dimensional tensor a circulant structure can be obtained such that a one-dimensional DFT can be used in acceleration of matrix-vector products. Of course, this is not as computationally efficient as the previous case as entries in the other dimension need to be computed fully, but it still provides acceleration.

While there are many methods using translation invariance as described here to solve MoM problems, in particular for volumetric MoM [30, 43, 169], in this dissertation it is only used for computing electric fields due to electric currents in disjoint regions. This is similar to approaches which have been used in digital holography where the typical operators act on disjoint source and observation planes [37, 52]. This implementation is simpler than would be necessary in the full solution of a problem, but still adds additional complexity compared to the Green's function example. The Green's function example is in turn more complex than the pure Toeplitz matrix for which the DFT-based acceleration was shown.

The operator needed for computing the forward problem of electric fields due to electric current is the integral operator in (2.79) with $\boldsymbol{M} = \boldsymbol{0}$. While the operator is still translation invariant, it is more complex than the pure Green's function as it contains more different terms and is vector-valued in input and output. Furthermore, the currents $\boldsymbol{J}$ must be represented in an appropriate way which offers the same kind of translation invariance as between points in meshed as described in the Green's function case. This could, for example, be done by using rooftop basis functions defined for each edge in the source grid. If the source and observation grids are equal in x and y, the basis functions are not aligned with the observation points and they differ in number. The algorithm is still useful, but the enumeration of source and observation quantities can become quite cumbersome in implementations. As for Green's functions, it is also possible to use translation invariance in only one direction when using the operator in (2.79). This was done in Paper IV where such an operator was used in an imaging algorithm with sources on a singly curved surface and observations in a planar grid. That work was based on similar imaging techniques for planar surfaces with full translation invariance in [60, 61].

3.5.2 The Adaptive Cross Approximation

The adaptive cross approximation (ACA) is a method for compression of matrices based on low-rank approximations. For any matrix $\mathbf{A} \in \mathbb{C}^{m \times n}$, the rank r is given by its number of linearly independent columns. If $r < m, n$ the matrix can be written on the outer product form as

$$\mathbf{A} = \mathbf{U}\mathbf{V}^{\mathrm{H}}, \ \mathbf{U} \in \mathbb{C}^{m \times r}, \ \mathbf{V} \in \mathbb{C}^{n \times r}. \tag{3.48}$$

It is clear that in cases where $r \ll m, n$ this form provides a more efficient way to store $\mathbf{A}$. One way to achieve this form is by using the singular value decomposition (SVD) which reads

$$\mathbf{A} = \mathbf{U}\boldsymbol{\Sigma}\mathbf{V}^{\mathrm{H}}, \ \mathbf{U} \in \mathbb{C}^{m \times m}, \ \mathbf{V} \in \mathbb{C}^{n \times n}, \ \boldsymbol{\Sigma} \in \mathbb{C}^{m \times n} \tag{3.49}$$

and where $\boldsymbol{\Sigma}$ only has nonzero entries $\sigma_1, \ldots, \sigma_r$ on the diagonal. Any diagonal entries above r in $\boldsymbol{\Sigma}$ are zero, which directly means that the decomposition can be rewritten on the form in (3.48). However, the algorithm to compute the SVD has a memory complexity $O(n^2)$, and a computational complexity $O(n^3)$ if $m \sim n$ [144]. This offers no improvement over a direct method, so other algorithms are needed. One such algorithm is the ACA.

At its core, the ACA is an algorithm which constructs an approximate representation $\mathbf{U}\mathbf{V}^{\mathrm{H}}$ for $\mathbf{A}$ by using only a subset of its rows and columns [16, 17, 167]. Since not all of $\mathbf{A}$ is used by the algorithm, the necessary parts can be constructed as needed to greatly reduce the memory use compared to full storage of $\mathbf{A}$. An explicit description of the ACA algorithm for MoM computations can be found in [167], and readers are referred to this for details. Here, a brief overview of the algorithm, broadly based on [167], is provided. The starting point of the ACA

is before the matrix $\mathbf{A}$ is constructed. In the first step, a row is selected to be constructed, typically taken to be the first row of $\mathbf{A}$. This, normalized by its largest entry in absolute value, is saved as the first row of $\mathbf{V}^{\mathrm{H}}$. Next, a column is selected to be constructed, which is the column in $\mathbf{A}$ containing the largest entry in absolute value of the first row. This column is saved as the first column of $\mathbf{U}$. Following these two first selections, subsequent rows of $\mathbf{V}^{\mathrm{H}}$ and columns of $\mathbf{U}$ are constructed by a similar selection process, but with the entries already present subtracted. If this was the full algorithm, rows and columns would continue to be constructed until obtaining all entries, resulting in no compression. To avoid this, an estimate of the error $\left\| \mathbf{A} - \mathbf{U}\mathbf{V}^{\mathrm{H}} \right\|$ (in Frobenius norm) is computed at each iteration of the algorithm, and the iteration can be stopped when a desired error is reached. Crucially, this estimate is computed using only the information already used for the construction of $\mathbf{U}$ and $\mathbf{V}^{\mathrm{H}}$.

While the application of the ACA when constructing a matrix $\mathbf{A}$ results in a representation on outer product form, it is not optimal in the way that the SVD is, that is having $\mathbf{U}$ and $\mathbf{V}$ unitary and of minimal inner dimension. This can be remedied by using the QR decomposition and the SVD to recompress the representation from the ACA as follows [15]. The QR decompositions are written as

$$\mathbf{U} = \mathbf{Q}_{\mathrm{U}}\mathbf{R}_{\mathrm{U}}, \ \mathbf{U} \in \mathbb{C}^{m \times k}, \ \mathbf{Q}_{\mathrm{U}} \in \mathbb{C}^{m \times k}, \ \mathbf{R}_{\mathrm{U}} \in \mathbb{C}^{k \times k} \tag{3.50}$$

$$\mathbf{V} = \mathbf{Q}_{\mathrm{V}}\mathbf{R}_{\mathrm{V}}, \ \mathbf{V} \in \mathbb{C}^{n \times k}, \ \mathbf{Q}_{\mathrm{V}} \in \mathbb{C}^{n \times k}, \ \mathbf{R}_{\mathrm{V}} \in \mathbb{C}^{k \times k} \tag{3.51}$$

where the $\mathbf{Q}$ matrices are unitary and $\mathbf{R}$ matrices are upper triangular. The outer product form can be represented as

$$\mathbf{U}\mathbf{V}^{\mathrm{H}} = \mathbf{Q}_{\mathrm{U}}\mathbf{R}_{\mathrm{U}}\mathbf{R}_{\mathrm{V}}^{\mathrm{H}}\mathbf{Q}_{\mathrm{V}}^{\mathrm{H}}. \tag{3.52}$$

Now, the SVD can be computed for the product of the $\mathbf{R}$ matrices, which is only $k \times k$, as

$$\mathbf{R}_{\mathrm{U}}\mathbf{R}_{\mathrm{V}}^{\mathrm{H}} = \hat{\mathbf{U}}\hat{\boldsymbol{\Sigma}}\hat{\mathbf{V}}^{\mathrm{H}} \tag{3.53}$$

and a new outer product form is finally obtained as

$$\mathbf{U}\mathbf{V}^{\mathrm{H}} = \left(\mathbf{Q}_{\mathrm{U}}\hat{\mathbf{U}}\hat{\boldsymbol{\Sigma}} \right) \left(\mathbf{Q}_{\mathrm{V}}\hat{\mathbf{V}} \right)^{\mathrm{H}} \tag{3.54}$$

where both matrices are unitary and of minimal inner dimension. If $k \ll m, n$, both the QR and SVD are computed for matrices with significantly smaller dimensions than $\mathbf{A}$ and the recompression can therefore be applied without changing the complexity of the ACA algorithm [15].

An important question when it comes to the applicability of the ACA is if low rank matrices actually arise in the applications of interest. There are cases in CEM where this can happen naturally. One example is in MoM computations of large array antennas where the system matrix can be subdivided into blocks corresponding to self-interaction and coupling between array elements. In this
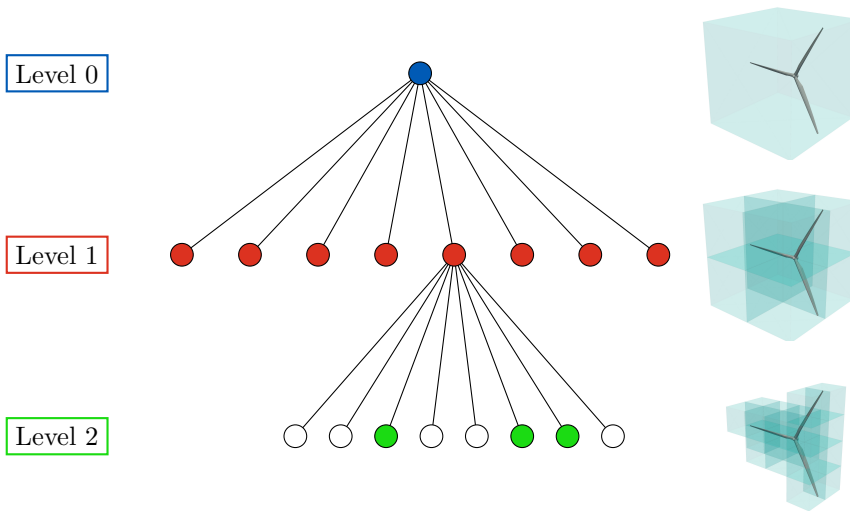
Figure 14: An octree shown as a tree data structure and geometrically at the three first levels. Note that there are several groups that are empty at level 2.

case, blocks which do not correspond to self-interaction are expected to have lower rank and can readily be compressed using the ACA [62, 63].

While the easily separable geometry in antenna arrays makes for simple ACA use, the same does not hold for general geometries. In a general mesh, it can typically not be assumed that the matrix is easily decomposed into clear blocks like array elements, but this can be achieved using an intermediate step. This step is a geometric clustering of the unknowns in the problem such that groups of unknowns are formed, which can be used similar to blocks in the array case. Typically, this is done by generating an octree, which is a hierarchical data structure originally developed for computer graphics [91]. It provides geometric clustering by creating a cubic bounding box around the geometry in question and splitting it into eight cubes. These smaller cubes are considered children to the original bounding box, and this is the start of a tree data structure of cubic groups of decreasing size as the tree deepens. The octree is refined by performing the same split into eights for each child until a stopping criterion, which could be a certain tree depth or a certain number of unknowns in a leaf node group, for example. An example of this clustering is shown in Figure 14 both as a tree and the corresponding geometrical groups.

The ACA can be applied to unknowns using the leaf groups of the octree in a similar way to that described for the array case. Typically this means that the ACA is applied to interactions between non-neighboring leaf groups. However, more improvements can be done by introducing a multilevel algorithm instead. This is similar to how the multilevel fast multipole method works, but simpler
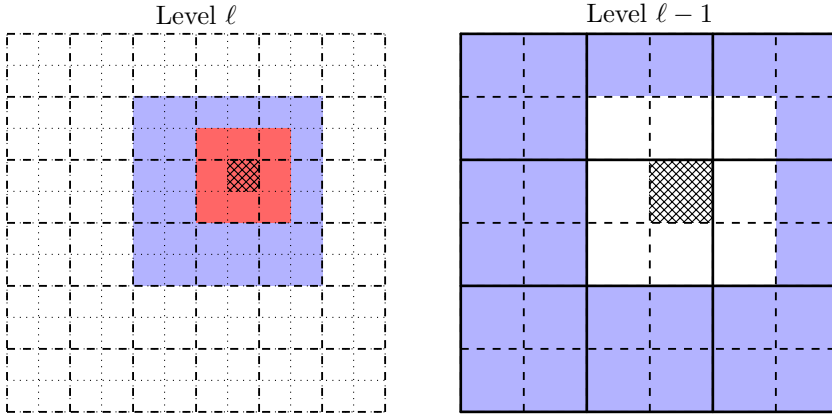
Figure 15: Near groups for full computations (red) and far interacting groups for ACA computations (blue) at two levels. The group marked with a crosshatch pattern is the source group. Boundary lines between groups are dotted for level ℓ, dashed for level $\ell - 1$ and solid for level $\ell - 2$.

to implement, which builds upon a more general concept for hierarchical computations [14, 65]. Multilevel ACA computations using an octree begin at the leaf level (level ℓ), where near interactions for sources in each group are considered first. Interactions between unknowns within the source group or this and neighboring groups are computed without the ACA as these unknowns are too close for reasonable compression. Since these interactions are few compared to the total number of system matrix entries, their entries are stored in a sparse matrix. Groups at level ℓ which are not neighbors with the source group, but whose parent groups at level $\ell-1$ are neighbors to the parent of the source group, are called "far interacting". Interactions between unknowns in these groups are computed using the ACA. After this is done for all groups at level ℓ, level $\ell - 1$ is considered. The far interacting groups at this level are identified for all groups at level $\ell - 1$, and interactions between them are computed using the ACA. In Figure 15, these group types are shown for a two-dimensional (quadtree) representation. It can be seen that the far interacting groups for the crosshatch patterned source group at level $\ell - 1$ are disjunct to those at level ℓ. As such, there is no duplication of interactions at different levels. As we travel toward the root of the octree, the group size increases as well as the separation between groups. The idea is that a larger separation results in a lower rank for a given group size, and as such the groups can contain more unknowns at higher levels.

While the ACA can be used for compression in many cases, it is optimal for use with integral operators whose kernels are smooth [17]. Unfortunately, this does not include the operators used in MoM for electrically large problems, like the scattering problems of interest to this dissertation. However, while the ACA should then be better for electrically small electromagnetic problems, the performance degradation with increasing electrical size is graceful and the ACA

can still be used with success for many problems where the kernel is not smooth, like said scattering problems [17, 71]. Typically though, it scales worse than the multilevel fast multipole method for an increasing electrical size [71]. Other methods similar to the ACA, but with better performance for kernels which are not smooth, have been developed like the butterfly decomposition [51, 93]. Nevertheless, there are certain geometries where low-rank approximations like the ACA perform particularly well like elongated and quasi-planar structures [51]. In this dissertation, the ACA was used to compress BI blocks for the FE2MS FE-BI code introduced in Paper I. One detail which can be noted is that this code is implemented using lowest order basis functions for both FE and BI parts. For the FE part in particular, the mesh tetrahedrons for these basis functions may need to be small in order to obtain sufficient accuracy, particularly if their face triangles are compared to typical sizes of BI mesh triangles. Furthermore, mesh sizes in the FE part are further reduced by scaling by the refractive index of the medium. Taken together, the BI mesh can often contain smaller mesh elements than typical sizes. These situations are well-adapted to the ACA though, as the high mesh density means that far interacting groups for lower levels in the octree are within electrically small regions where the kernel of the integral operator is comparatively smooth.

3.6   Implementing Computational Methods

While some methods for accelerating computational methods were described in section 3.5, details in how computational methods are implemented can also have dramatic consequences on performance. These are very general concepts like performance of different programming languages, optimization of code, general code architecture and the type of hardware that is used in computations.

One way to divide types of programming languages is in interpreted languages and compiled languages. In interpreted languages, each command in a program is executed directly on the machine, while in compiled languages the full program needs to be compiled into machine code that can in turn be executed on the machine. Interpreted languages are typically more flexible to use than compiled languages since commands can be executed one by one, and intermediate results are available at any point. However, compiled languages are typically much more efficient. Some examples of programming languages often used in scientific computations are the compiled languages C++ and Fortran, and the interpreted languages Python and MATLAB [18, 99]. More recently, another option called just-in-time (JIT) compilation has become more available. Languages with this feature can compile parts of a program when they are first executed, while possibly keeping features from interpreted languages for other parts. An example of a language used in scientific computations with native JIT compilation is Julia [18], but JIT compilation is also available for Python [81] and MATLAB [142].

A great aid when implementing computational methods from scratch is the availability of open-source software to use as a base. At some level, there is

always a base library of tools, regardless of what programming language is used. However, software packages with significantly higher levels of functionality may be available under open-source licenses, and what might be available depends on the programming language. One language with a large number of easily accessed open-source software packages is Python. There are many reasons for this, including, of course, Python's wide popularity and ease of use, but an important factor for the specific application of scientific computing is the common framework of efficient data structures, linear algebra functions and other utility given by the NumPy package [59].

The FE2MS FE-BI code described in Paper I is written mostly in Python, and combines many different open-source software packages for its functionality. The most important packages and some of the reasons for using them are described here, but a more in-depth discussion is available in Paper I. Before discussing packages used for computations, it is important to consider the geometry and mesh used for the code. Meshes used in the code are on the format produced by the Gmsh package [45], and since this package has a Python application programming interface (API) it is possible to handle meshing in the same Python scripts as the computations. As for the computational code itself, the FE and BI parts are considered somewhat separately, which makes sense when looking at the theory of the FE-BI method in section 3.3. The FE part is implemented using the FEniCSx package, which is a very versatile package for FEM which can handle general weak forms, many different mesh elements and basis functions, among others. FEniCSx consists of the components DOLFINx [13], FFCx [84], Basix [126,127] and UFL [3]. In addition to providing a complete implementation of the FE part, FEniCSx gives access to much of the infrastructure needed to implement the BI part. This includes data structures for mesh, basis functions and numerical quadrature. Furthermore, the connection between the two parts is facilitated by the use of FEniCSx data structures for both. Much of the BI part itself is written specifically for the FE2MS code with the lower-level computational framework from NumPy. Furthermore, JIT compilation using Numba [81] is used to dramatically improve performance of parts where standard Python performance is poor, like in assembly of system matrices. An often challenging part of integral equation methods is that of singularity handling. As described in section 3.2, singular integrals arise from typical Galerkin testing of the EFIE and MFIE, and they need to be handled appropriately. In the FE2MS code this is done using the DEMCEM package which offers efficient methods for solving singular integrals due to these equations for a triangular mesh [105–107, 109]. Since DEMCEM is implemented in C++, its use in a Python code required some additional work using the pybind11 package [69] for connecting code from the two different programming languages. To improve performance of the BI part of the FE2MS code, a multilevel ACA is used for compression of the BI blocks of the system matrix. The octrees used for geometric clustering of unknowns in this algorithm are created using the AdaptOctree package [73]. This combination of open-source software packages facilitated the development process and greatly accelerated it, especially since the development was from

scratch without an existing in-house codebase.

When working with open source, it is useful to understand some of the legal framework and licenses that are commonly used. This is especially true if publishing software based on many open-source packages which might use different licenses. Broadly, there are two types of licenses under the broader term open source: permissible licenses and copyleft licenses. Permissive licenses are, as indicated by the name, very permissive and put almost no restrictions on how the user might apply the software. A common example is the Berkeley Software Distribution (BSD) 3-clause license [100] which is, for example, used in NumPy and SciPy. Copyleft licenses, on the other hand, are more restrictive, mostly regarding distribution of derivative software. One of the most common such licenses is the general purpose license (GPL) which essentially states that software which uses GPL-licensed software can only be distributed if it is so under the same license [138]. The underlying reason is quite ideological in that it aims for open-source software to not be used in closed-source software at a later stage [138]. This license mechanism is a reason why the FE2MS FE-BI code described in Paper I is released under the GPLv3 license as opposed to, for example, BSD 3-clause.

4   Imaging Methods and Nondestructive Testing

Microwave imaging has been used in many different applications such as remote sensing, security scanners and NDT [2, 98]. Microwaves are defined as the frequencies 300 MHz–300 GHz, with a narrower region of mm-waves taken as the upper range starting at 30 GHz (corresponding to a wavelength of 1 mm). Microwave imaging has long been been performed for long-range applications such as remote sensing and radar imaging from satellites and aircraft [114, 115], but shorter-range systems have been feasible more recently [98]. These systems are lower in cost due to significant developments in hardware, and progress in signal processing means that there are more possibilities for what can be deduced from the data [2]. The decrease in cost and increase in capabilities has opened up for many new applications of microwave and mm-wave imaging [98].

In this dissertation, mm-wave imaging has been applied to NDT. NDT as a general field of study covers a vast amount of applications and physical phenomena, and as such it is difficult to give an all-encompassing introduction. The general idea behind any NDT, however, is to use some kind of physical phenomenon to learn about the properties of a device under test (DUT) without damaging its usefulness. The phenomenon used in testing should give some indication which can be connected to flaws in the DUT [131]. Depending on the property of the DUT which is to be investigated, different physical phenomena might be more or less useful. For example, mechanical properties are often evaluated using ultrasonic NDT methods since ultrasound is an acoustic wave whose propagation

properties are determined by mechanical properties of the medium [125]. A flaw, however, can have effects on many different properties. For example, hard metallic inclusions in a soft foam would result in high contrasts both for ultrasound and mm-waves.

The use of microwaves and mm-waves in NDT is relatively new compared to ultrasound, but has advantageous properties when testing many newer types of materials [74, 168]. It can be particularly interesting for applications where electromagnetic performance is one of the properties to be evaluated, in addition to mechanical flaws. One such application is radomes, where the full structure has been carefully designed for high transmission in the band of an enclosed antenna [103]. Another example may be aerospace structural elements, which can be designed for low radar cross section in some defense applications. In Paper IV, mm-wave imaging is applied to NDT of thin, low-permittivity, singly curved composite panels used in aerospace applications.

4.1   Fourier-Based Imaging

Many of the most widely used methods in microwave and mm-wave imaging are based on Fourier analysis [98]. Since Fourier analysis covers a wide range of methods focused on trigonometric functions, like time-harmonic electromagnetic waves, it is hardly surprising. The work presented in this dissertation, however, rather focuses on imaging methods based on inverse scattering as will be described in section 4.2. Nevertheless, Fourier-based imaging is always going to present itself as a natural comparison due to its prevalence. In this section, one such method is introduced as it is used as a method for comparison to the inverse scattering method in Paper IV.

The method in question is referred to as time reversal in Paper IV, but is also known as convolution-based reconstruction and migration, among others [98, 139]. The main idea of the method is related to the propagation of plane waves on the form given earlier in (2.24). The measurable signal of a single plane wave propagating in z can be described as

$$s(z) = Se^{-jk_z z} \tag{4.1}$$

where the complex amplitude S is typically not known. This means that if the signal is measured at a z-coordinate z_0, the signal at another z-coordinate $z_1 < z_0$ can be determined as

$$s(z_1) = Se^{-jk_z z_1} = Se^{-jk_z z_0}e^{jk_z(z_0-z_1)} = s(z_0)e^{jk_z(z_0-z_1)}. \tag{4.2}$$

This is not very useful on its own as the signal measured in imaging applications is not a plane wave, but if it is combined with the concept of plane wave expansions the imaging method becomes clear. Plane waves can be used as a basis to describe any type of wave. As such, a signal s can be described as [101]

$$s(x, y, z) = \frac{1}{(2\pi)^2} \int_{-\infty}^{\infty} \int_{-\infty}^{\infty} S(k_x, k_y)e^{-j(k_x x + k_y y)}e^{-jk_z z} \, dk_x \, dk_y \tag{4.3}$$

where S is the signal representation in a plane-wave basis or, as commonly expressed, in the spectral domain, and the wave number in z depends on the other wave numbers as $k_z = \sqrt{k^2 - k_x^2 - k_y^2}$. Equation (4.3) is identified as a two-dimensional Fourier transform in x and y, and the representation in the spectral domain for a single pair of k_x, k_y can be treated as a single plane wave propagating in z. This means that the same approach for changing to z-coordinate that was described for a single plane wave can be applied to each spectral-domain signal component as

$$S(k_x, k_y, z_1) = S(k_x, k_y)\mathrm{e}^{-\mathrm{j}k_z z_1} = S(k_x, k_y, z_0)\mathrm{e}^{\mathrm{j}k_z(z_0 - z_1)}. \tag{4.4}$$

A measured signal $s(x, y, z_0)$ can thus be time reversed to $s(x, y, z_1)$ by a sequence of Fourier transformation, multiplication of each component by $\exp(\mathrm{j}k_z(z_0 - z_1))$ for its computed k_z and inverse Fourier transformation of the result. This enables imaging if the coordinate z_1 is selected at appropriate values. Importantly though, the model used for the signal contains no sources, and as such it is not possible to propagate the signal beyond a region containing sources (such as a transmitting antenna).

In practice, the signal measured at z_0 is only sampled at a discrete set of points (x_m, y_n, z_0), $m = 0, 1, \ldots, N_x - 1$, $n = 0, 1, \ldots, N_y - 1$. If this is done in a uniform grid, the Fourier transforms can be replaced by standard discrete Fourier transforms (DFT) efficiently computed by fast Fourier transform (FFT) algorithms. An imaging algorithm can now be written down as:

1. Obtain measured signal as a matrix with entries $s_{mn} = s(x_m, y_n, z_0)$.

2. Compute matrix in spectral domain with entries $S_{mn} = S(k_{x,m}, k_{y,n}, z_0)$ as $\mathbf{S} = \mathrm{fft2}\,(\mathbf{s})$.

3. Generate wave number matrix with entries $k_{z,mn} = \sqrt{k^2 - k_{x,m}^2 - k_{y,n}^2}$.

4. Compute image in spectral domain as $\mathbf{S^i} = \mathbf{S} \circ \mathrm{e}^{\mathrm{j}\mathbf{k_z}(z_0 - z_1)}$ ($\circ$ denotes element-wise product, exponential taken element-wise).

5. Compute image as $\mathbf{s^i} = \mathrm{ifft2}\,(\mathbf{S^i})$

where fft2 and ifft2 are used to denote the two-dimensional FFT and inverse FFT, respectively.

The time reversal algorithm as described here generates images in planes parallel to a measurement plane, but it is easy to extend to images on other surfaces. By generating images for a set of z-coordinates increasingly far from z_0, volumetric data is obtained. From such data, an image can be generated on an arbitrary surface within the data volume. This is done in Paper IV where images are generated on the surface of singly curved composite panels.

4.2   Inverse Scattering

The second type of imaging methods are based on inverse scattering. The problem of electromagnetic scattering was introduced in section 2.4 as a problem where a known object is illuminated by a known incident wave and the scattered wave should be computed. Inverse scattering is, as might be deduced from the name, an inverse of that problem. The type of inverse problem relevant here is that an unknown object is illuminated by a known incident wave and the scattered wave is measured. From the knowledge of the incident and scattered waves, the properties of the unknown object should be determined. Inverse problems like this are generally significantly more challenging than the direct scattering problem as they are ill-posed [56]. An example of why this is can be seen if the inverse problem would be to determine equivalent currents on a known object using measurements of the scattered electric field. This can be modeled using (2.79) and a discretization procedure similar to that used for MoM as described in section 3.2. However, the resulting matrix is ill-conditioned, meaning that small measurement errors lead to large errors in the reconstructed currents, and this is a typical issue in all inverse problems [56, 151]. It is necessary to use additional methods to remove this problem, called regularization methods. These enforce that the solution to the inverse problem fulfill certain properties like smoothness, often by solving some kind of optimization problem [56].

In Paper IV, an inverse equivalent source formulation is used for mm-wave imaging. This is a method based on the concept of equivalent currents in section 2.6. From a set of electric and magnetic currents, as in the case of equivalent currents, the electric field can be computed using (2.79). The inverse problem is thus a computation of the currents using a measured electric field, as in the example from the previous paragraph. Earlier work in [60] and [61] performed imaging on planar composite panels. With regards to the use of equivalent currents, purely electric currents were used with a theoretical basis that such equivalent currents on an infinite plane are easily relatable to the tangential fields, as described in section 2.6. Of course, the infinite plane was truncated to only be large enough to contain all significant sources, since this surface would correspond to unknowns in the integral operator. In paper IV though, the planar composite panels were exchanged for singly curved ones. This change brought with it a number of theoretical issues. To use the equivalence theorem on a surface, it needs to be a closed surface. In the planar case, this is simply an infinite plane, but it is not as straight-forward in the singly curved case. In addition, the move away from a planar surface meant that the simple connection between equivalent currents and tangential fields would not be the same as before.

For the problem with closing the surface, it can be noted that the original planar imaging did not use a fully closed surface either but instead relied on using a sufficiently large open reconstruction surface. This is illustrated in Figure 16 where the equivalent currents for a radiating horn antenna are shown on a planar surface. It is seen that only a subset of the full (infinite) planar surface contains significant currents, and as such it is sufficient to reconstruct the currents there.
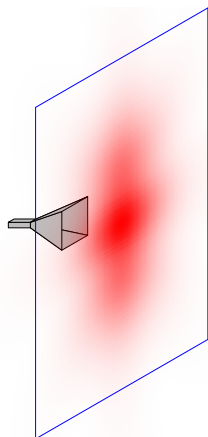
Figure 16: Horn antenna and $|\boldsymbol{M}_{\mathrm{s}}^{\mathrm{eq}}|$ on a planar surface in red. Reconstruction surface in blue covers a small region containing significant equivalent currents.

Of course, what is meant by "significant" depends on the application and how accurate the representation needs to be. The hypothesis for the singly curved surface was that the same approach could be used, even though the exact shape of the closed surface was unknown.

For the problem with the relation between equivalent currents and fields, a few solutions were already discussed in section 2.6. Of course, the use of both electric and magnetic currents with a standard zero field condition would give the usual relations in (2.74) and (2.75). This would, however, increase the number of unknowns by a factor 2, which was not desirable. Another solution would be to fill the interior with PMC/PEC and only have one type of current, but this would require custom Green's functions as opposed to the free space Green's function used previously. Finally, it is possible to simply use purely electric equivalent currents, but then the simple connection between equivalent currents and fields would be lost. However, the idea was that it would not be a critical issue for the application at hand.

One important consideration behind the choices in adapting the method for singly curved surfaces was that the intended use was primarily qualitative. In applications such as near-field-to-far-field transformations for antenna diagnostics, it is critical that equivalent currents are reconstructed correctly for the far-field computation to be correct. Our application, on the other hand, was in imaging directly on the DUT, which meant that the equivalent currents could not be used in any subsequent computation step. Furthermore, the application for the imaging was qualitative in that the goal of the NDT application is to determine whether flaws are present in a DUT or not. Reconstruction errors which might be critical in applications like antenna diagnostics can be irrelevant in such applications. However, it was necessary to test whether that actually was the case, which was one of the main points of Paper IV.
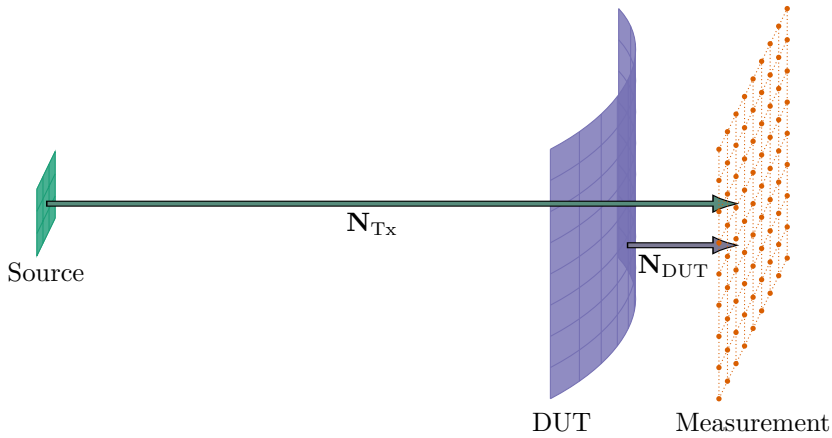
Figure 17: Geometry in transmission-based imaging. Operators $\mathbf{N}_{\mathrm{Tx}}$ and $\mathbf{N}_{\mathrm{DUT}}$ connect electric currents to electric fields.

The imaging geometry used in Paper IV is shown in Figure 17 together with operators which connect electric currents in one plane to electric fields in another. In the figure, the source and DUT surfaces are surfaces where electric currents can exist. In implementation, these are discretized as rectangular surface meshes where currents are represented using rooftop basis functions. The measurement surface does not contain any currents, but is discretized into a rectangular mesh matching the density of the DUT mesh. Electric fields due to currents on the source and DUT surfaces are computed in the node points of this measurement mesh.

4.2.1   Source Separation

To perform inverse scattering, the scattered wave is required. To obtain this, the typical procedure is to perform two measurements: one reference measurement without the DUT and one measurement with the DUT. The reference measurement is then subtracted, giving results for only the wave scattered by the DUT. However, this can be time-consuming if the measurement system is based on mechanical scanning, and it is also sensitive to changes between the measurements. Particularly in the case for mm-waves, mechanically small changes can still be significant electromagnetically due to the small wavelength. Another issue with the traditional method for the NDT application is that the scattered wave is due to the entire DUT and not just flaws.

To remove the need for two measurements, the incident electric field can be removed numerically. In Paper IV, this is done using a truncated SVD according to a method introduced in the earlier work from [60]. The method attempts to find equivalent currents for the smooth part of the measured electric field using only a single measurement of the DUT. As it is the smooth part of the electric

field that is found, it includes any such contributions from the DUT which are likely to be due to the larger structure of the DUT and not due to flaws.

The source separation algorithm attempts to perform a decomposition of the measured field $\boldsymbol{E}^{\mathrm{meas}}$ as

$$\boldsymbol{E}^{\mathrm{meas}} = \boldsymbol{E}^{\mathrm{inc}} + \boldsymbol{E}^{\mathrm{sc}} \tag{4.5}$$

where $\boldsymbol{E}^{\mathrm{inc}}$ is the incident field from the source and the homogeneous part of the DUT and $\boldsymbol{E}^{\mathrm{sc}}$ is the field scattered by flaws in the DUT, which is assumed to be orders of magnitude smaller than $\boldsymbol{E}^{\mathrm{inc}}$. A plane is constructed in front of the source antenna for equivalent currents to be placed. The incident electric field is related to electric currents $\boldsymbol{J}^{\mathrm{Tx}}$ in this source plane using a linear operator $\mathbf{N}_{\mathrm{Tx}}$ based on (2.79) as

$$\boldsymbol{E}^{\mathrm{inc}} = \mathbf{N}_{\mathrm{Tx}}\boldsymbol{J}^{\mathrm{Tx}}. \tag{4.6}$$

Insertion of this in (4.5) gives a system

$$\boldsymbol{E}^{\mathrm{meas}} = \mathbf{N}_{\mathrm{Tx}}\boldsymbol{J}^{\mathrm{Tx}} + \boldsymbol{E}^{\mathrm{sc}}. \tag{4.7}$$

Since the left-hand side is known and $\boldsymbol{E}^{\mathrm{sc}}$ is considered to be small, it is possible to estimate $\boldsymbol{J}^{\mathrm{Tx}}$ by considering a solution by truncated SVD regularization [56]. For this, the operator is expressed as the SVD

$$\mathbf{N}_{\mathrm{Tx}} = \mathbf{U}\boldsymbol{\Sigma}\mathbf{V}^{\mathrm{H}} \tag{4.8}$$

where $\mathbf{U}$ and $\mathbf{V}$ are unitary and $\boldsymbol{\Sigma}$ is diagonal with the reciprocal of singular values on the diagonal. The regularization is now performed by truncating the matrix $\boldsymbol{\Sigma}$. The elements corresponding to normalized singular values smaller than a threshold τ are set to zero. This threshold is traditionally set according to the L-curve criterion [56], but as discussed in [61] there are difficulties with this approach. Instead, the approach for selecting τ here combines analysis of the drop-off of the normalized singular values with inspection of the resulting solution $\widehat{\boldsymbol{J}}^{\mathrm{Tx}}$. The regularized solution $\widehat{\boldsymbol{J}}^{\mathrm{Tx}}$ is found using a Moore-Penrose pseudoinverse from the truncated SVD as [56]

$$\widehat{\boldsymbol{J}}^{\mathrm{Tx}} = \mathbf{V}\widetilde{\boldsymbol{\Sigma}}^{-1}\mathbf{U}^{\mathrm{H}}\boldsymbol{E}^{\mathrm{meas}} \tag{4.9}$$

where $\widetilde{\boldsymbol{\Sigma}}$ is the truncated diagonal matrix. The solution $\widehat{\boldsymbol{J}}^{\mathrm{Tx}}$ can now be used to compute an estimate $\widehat{\boldsymbol{E}}^{\mathrm{inc}}$ anywhere, which for this method primarily means at the DUT and the measurement plane. At the measurement plane, it is subtracted from $\boldsymbol{E}^{\mathrm{meas}}$ to render an estimate for the scattered field, $\widehat{\boldsymbol{E}}^{\mathrm{sc}}$, which is used in the next step of the imaging process. An example of the source separation is shown in Figure 18 for a singly curved dielectric DUT containing four small PEC squares. This data was synthetically generated using MoM in the solver Feko [4].

$$|\boldsymbol{E}^{\mathrm{meas}}|$$

$$|\widehat{\boldsymbol{E}}^{\mathrm{inc}}| \qquad \swarrow \qquad \searrow \qquad |\widehat{\boldsymbol{E}}^{\mathrm{sc}}|$$
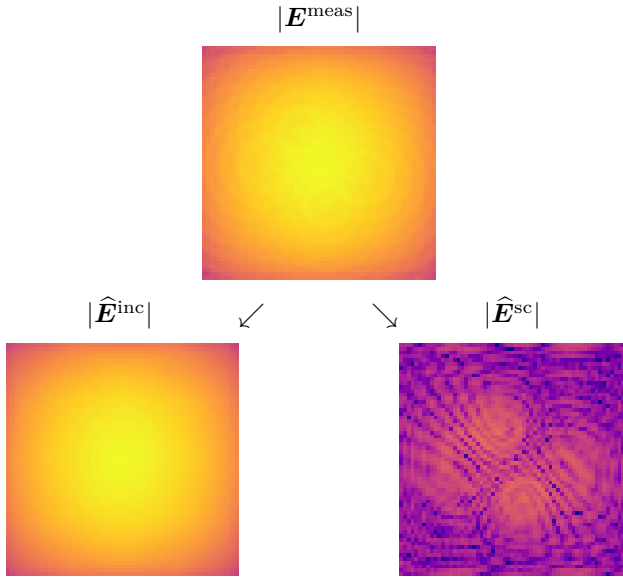
Figure 18: Images showing amplitudes of the measured field and the separation into estimated incident and scattered fields.

4.2.2 Sparse Image Reconstruction

The image reconstruction step uses the estimate for the scattered field $\widehat{\boldsymbol{E}}^{\mathrm{sc}}$ to compute electric currents on the DUT surface. Since the inverse scattering problem is generally ill-posed, some type of regularization is necessary. We use methods based on a forward operator $\mathbf{N}_{\mathrm{DUT}}$ from electric currents $\boldsymbol{J}^{\mathrm{DUT}}$ on the DUT surface to scattered electric fields using (2.79) on the form

$$\boldsymbol{E}^{\mathrm{sc}} = \mathbf{N}_{\mathrm{DUT}}\boldsymbol{J}^{\mathrm{DUT}}. \tag{4.10}$$

Due to uneven illumination of the DUT, though, the scattered electric field from different regions can vary in amplitude. To construct an image without this variation, the electric currents are normalized by the incident field on the DUT $\boldsymbol{E}^{\mathrm{DUT}}$, which is computed from the source separation currents $\widehat{\boldsymbol{J}}^{\mathrm{Tx}}$. Images are constructed from these scattering amplitudes $\boldsymbol{s}$ defined as

$$\boldsymbol{J}^{\mathrm{DUT}} = \boldsymbol{s} \circ \boldsymbol{E}^{\mathrm{DUT}} \tag{4.11}$$

where ∘ indicates a Hadamard (elementwise) product.

To construct images of $\boldsymbol{s}$ using the forward operator in (4.10), some properties specific to the NDT problem that are used, leading to a hypothesis of sparsity. Since the production methods where NDT is to be used are generally mature, it is assumed that any flaws are few and well separated such that high sparsity is achieved in a local basis. This is also dependent on the DUT being made from

low-permittivity composite materials with little scattering on its own, and further aided by the source separation removing this bulk scattering. The method for image reconstruction should therefore take sparsity into account and use only the forward operator in (4.10). As in [60,61] a method using basis pursuit denoising is used in Paper IV. This is an optimization method based on the L_1 norm which is suitable for finding sparse solutions [148]. What it amounts to is solving an optimization problem to find estimates $\hat{s}$ of scattering amplitudes as

$$\hat{s} = \arg\min_{s} \|s\|_1 \tag{4.12}$$

$$\text{s.t } \|\mathbf{N}_{\text{DUT}}(s \circ \widehat{\boldsymbol{E}}^{\text{DUT}}) - \widehat{\boldsymbol{E}}^{\text{sc}}\|_2 \leq \kappa\sigma \tag{4.13}$$

with $\kappa \leq 1$ being a user-defined parameter and σ is given by

$$\sigma = \|\mathbf{N}_{\text{DUT}}\mathbf{N}_{\text{DUT}}^{\text{H}}\widehat{\boldsymbol{E}}^{\text{sc}} - \widehat{\boldsymbol{E}}^{\text{sc}}\|_2. \tag{4.14}$$

Here, $\mathbf{N}_{\text{DUT}}^{\text{H}}\widehat{\boldsymbol{E}}^{\text{sc}}$ is the solution from a single phase conjugation of the estimated scattered field $\widehat{\boldsymbol{E}}^{\text{sc}}$ (the measured field subtracted by the estimated incident field). The bound in (4.13) thus leads to solutions with smaller residuals in L_2 than obtained by phase conjugation, with $\kappa < 1$ enabling even tighter bounds.

Implementation-wise, the optimization problem is solved using the SPGL-1 solver in basis pursuit denoise mode [148,149]. This solver applies the operator $\mathbf{N}_{\text{DUT}}$ and its Hermitian conjugate a large number of times before arriving at a solution. For this reason, acceleration of that particular operator can have a significant effect on the total performance. In [60,61] the imaging method used parallel DUT and measurement planes, and as such acceleration could be achieved by exploiting translation invariance in the Green's function as described in section 3.5.1. However, in Paper IV the DUT geometry is singly curved which means that this approach is no longer fully available. Instead, such acceleration is possible along one dimension but not the other to still provide some degree of acceleration. Another important computational detail is related to the resolution in the DUT mesh. It is possible to improve this from the original spatial sampling in the measurement plane by sub-sampling, i.e. dividing the mesh elements into smaller elements. Since equal discretization is necessary for acceleration though, the grid in the measurement plane needs to be extended to match the finer sampling in the DUT mesh. These additional points in the grid are only used for computational reasons and no additional measurement data is required.

5 Measurement Techniques

While much of this introduction has focused on computations, the papers in this dissertation include electromagnetic measurements as well. As such, a brief overview of such measurements is provided with emphasis on the issues particularly related to the measurements performed for the included papers. As this
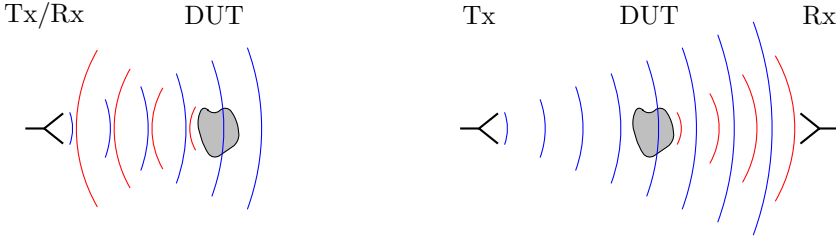
Figure 19: Monostatic (left) and bistatic (right) measurement setups. In both cases, a DUT is being measured. Note that the DUT scatters in many directions, and only the direction of interest is shown here.

dissertation focuses on electromagnetic scattering, this section focuses on scattering measurements in different forms. This typically means that there is a device under test (DUT) which is being subjected to an electromagnetic wave from a transmitting (Tx) antenna, and the waves affected by the DUT are measured using a receiving (Rx) antenna. The transmitting and receiving antennas can be in the same location, or even the same physical antenna, in which case the measurement is called monostatic. If they are in different locations, the measurement is called bistatic. This is illustrated in Figure 19.

Often the quantity of interest is the scattered electric field, but the measured quantity at the receiving end is the total electric field which is a combination of the incident and scattered waves as discussed in section 2.4. In a monostatic measurement this might not differ much from the scattered field, but in a bistatic measurement the incident field at the receiver may be significant, as seen in Figure 19. A commonly used method to obtain only the scattered field is to perform two measurements: one measurement with the DUT, and one reference measurement without the DUT. Since the situation is linear, the scattered field is obtained by subtracting the two received signals. This doubling of the number of measurements can be time-consuming though, especially if the measurement involves mechanical scanning of the receiving antenna to obtain the field in a certain region. To reduce the measurement time, the incident field can be numerically estimated using only one measurement with the DUT present. One way of doing this is by using the source separation technique described in section 4.2.1.

If a signal corresponding to the scattered wave has been measured, for example by subtracting a reference measurement, this is not sufficient for obtaining a quantity like the electric field or the RCS. The measured signal is typically a voltage which is not calibrated to the full measurement system, but is affected by the cables, the antennas, and in the case of RCS measurements, the free-space propagation. In measurements of microwave components, calibration can be done using known components to obtain accurate measurements at the ends of the cables. This type of calibration can be used in free-space measurements to remove effects of the cables, but further calibration is necessary to obtain a

calibration accurate for the electric field or the RCS. For some antennas, like open-ended waveguide probes, the effect of the antenna can be compensated for using theoretical expressions which makes them suitable for measurements in the near field [158, 159]. If measurements are done in the far field, calibration can be done by measuring a reference object with known properties and comparing measurements against that. For example, the DUT can be replaced by an object like a metallic sphere which has a well-known RCS to calibrate for [78].

5.1 Measurement Challenges and Solutions

One common problem in all measurements is the presence of random noise, which the signal of interest needs to exceed for it to be measurable. To quantify noise, the signal-to-noise ratio (SNR) which is the ratio between signal and noise power is used. This can, of course, be increased by using a larger signal power in the numerator, but there are also actions that can be performed to reduce the noise in the denominator. Noise can have many different origins, both from external sources and from within the measurement instruments, and this affects the steps which can be taken to reduce its influence. Noise sources external to the measurement instruments include other radiating devices, but also thermal radiation from surrounding objects with temperatures above 0 K [115]. One way to reduce external noise in particular is to perform measurements in a shielded chamber so that noise originating from outside the chamber is not received [78]. Significant noise also originates from within the measurement instruments, and this noise cannot be eliminated by external actions. Instead, the settings and setup of the instruments can be selected to reduce noise. Some of these settings act on noise in general, and not only instrument noise.

Due to the random nature of noise, a general action which reduces noise is averaging of the received signal over multiple samples [115]. Of course, this increases the measurement time as multiple samples are needed. Another action which is more related to the design of the receiver is to change settings for the so-called intermediate frequency (IF) filter in the receiver. How this is done in practice depends on the design of the receiver, but the result is a reduced bandwidth or increased selectivity of the filter with the bandwidth being the most important parameter. A decreased IF bandwidth increases the measurement time though, as more time is required to avoid transients of the reactive filter components [64].

Another problem in measurements is that of unwanted scattering and multi-path propagation. This is a problem that needs to be considered in all measurements of freely propagating electromagnetic waves. Ideally, a measurement setup would only include the transmitting and receiving antennas as well as the device under test (DUT) suspended in free space stretching out to infinity. This way, the received signal would only be affected by the (hopefully) characterized antennas and the unknown DUT. Unfortunately, the real world does not look like that, and the received signal is also affected by all other objects which scatter electromag-
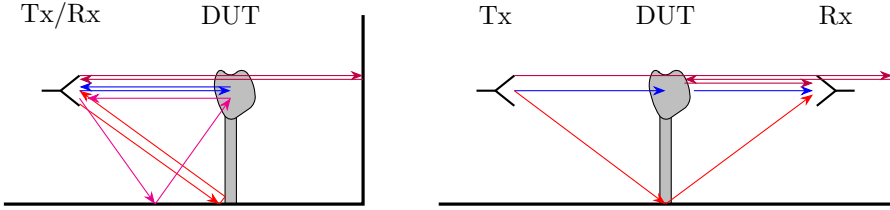
Figure 20: Examples of multipath propagation in monostatic (left) and bistatic (right) measurements.

netic waves. This is illustrated in Figure 20. If a reference measurement without the DUT is performed, much of this can be subtracted from the measurement. However, minor changes in the background between measurements can lead to significant signal components from unwanted scattering still being present after this subtraction. This is especially the case if the scattering from the DUT is weak in comparison to some of the possible scatterers.

One way to try to control this problem is by minimizing scattering from the measurement environment by using radiation-absorbent materials. These materials are engineered to absorb electromagnetic waves at certain frequencies of interest, and as such absorbers made from those materials can be used to reduce scattering by objects in the measurement setup [78]. A common use of absorbers is in anechoic chambers, where the floor, walls and ceiling are all covered by absorbers. With perfect absorbers, this environment would act as infinite free space (similar to the absorbing boundary conditions discussed in section 3.1). An example of an anechoic chamber is shown in Figure 21 where pyramidal absorbers can be seen covering most surfaces.

Other methods to reduce unwanted scattering are related to control over where waves are directed. One way to do this is by selecting transmitting and receiving antennas with narrow beamwidths such that only scattering by the DUT is captured [78]. The physical placement of the DUT is also important since a larger separation from surrounding objects means that fewer potential scatterers are visible within the beamwidth of the transmitting and receiving antennas. Objects can also be placed as to deliberately scatter waves, but in directions where they will not interfere with the measurement. This is the same idea as the concept in stealth technology where incident waves from a radar are redirected as to not return to the radar [78].

Finally, there are post-processing methods that can be used to separate the received signal into scattering by the DUT and scattering by other objects. As seen in Figure 22, the scattered waves that combine at the receiving antenna have different path lengths. These correspond to different propagation times which offers a way to remove unwanted signal components. If signals can be discriminated by the time between transmission and reception, with high enough temporal resolution, only the direct Tx-DUT-Rx signal component can be kept. This is called time gating as the unwanted components are "gated" out due to their too large
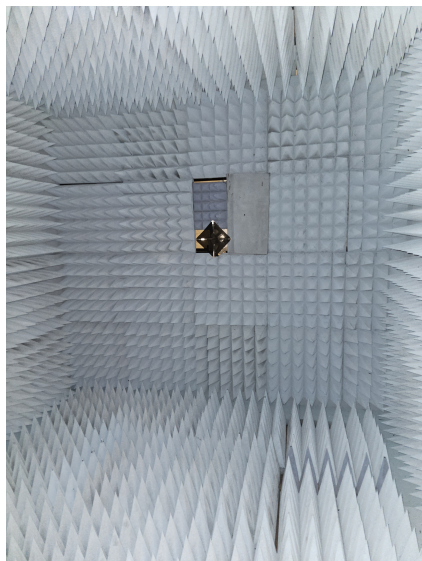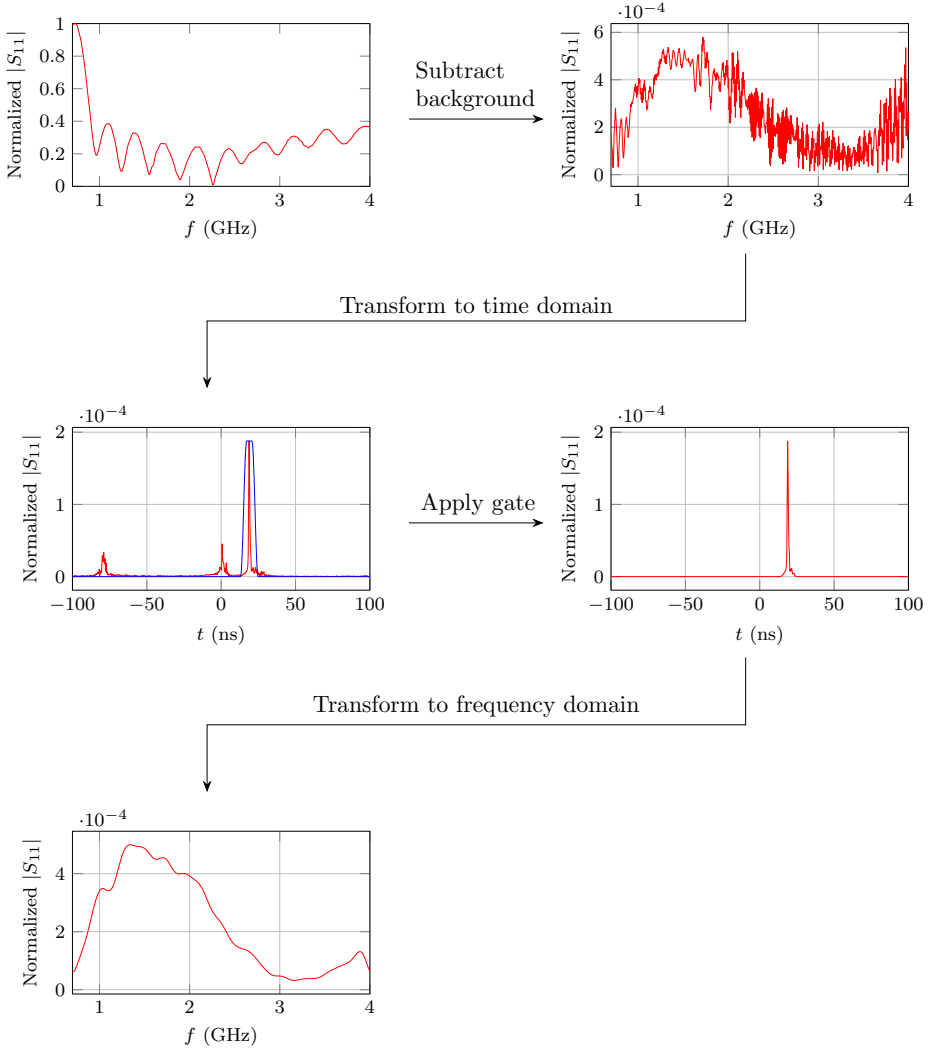
Figure 21: Anechoic chamber of the antenna laboratory at Lund University. Transmitting/receiving antenna in the center.

Tx   DUT   Rx
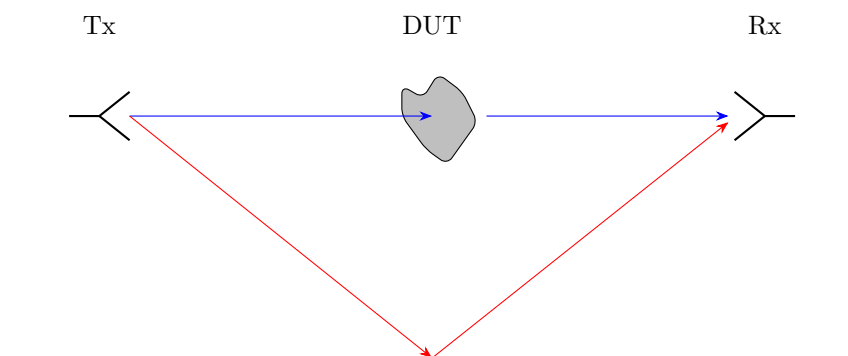
Figure 22: Two multipath components with unwanted path (red) having longer path length than the direct path (blue).

Figure 23: Example of background subtraction and time gating. The data is from a monostatic measurement of scattering by a metal sphere of radius 2.5 cm. The gate function shown in blue the third step is scaled for visualization purposes.

or too small propagation times. Typically, measurements are performed in the frequency domain so there is no direct access to the propagation times, but gating is easily done by Fourier analysis where the signal can be transformed to the time domain, processed, and transformed back to the frequency domain [78]. The application of the gate in the time domain changes the frequency content of the signal, causing sidelobes in the spectrum as the signal is transformed back to the frequency domain. There are many different window functions that can be selected as the gate to control these sidelobes [115]. An example of time gating as well as background subtraction of the raw data is shown in Figure 23 for real measurement data of monostatic scattering by a sphere. It is clear that the background subtraction is very effective, in particular due to reflections in the antenna being present in the raw data. However, the data can be improved by time gating and many unwanted scatterers are seen in the time domain plot. For time gating to be effective, the temporal resolution needs to be high enough to discriminate between different multipath components. The temporal resolution is directly related to an equivalent pulse width of the transmitter, which in turn is inversely proportional to the bandwidth. Time gating therefore puts a requirement on the bandwidth, which can be estimated if the spatial separation between scatterers in the setup is known.

5.2   Measurements in this Dissertation

Paper II, IV and V of this dissertation contain measurements with different setups, challenges and solutions. In this section, details of how the measurements were performed and why are provided. All instrument settings and details are not provided here as they are in the papers themselves. Instead, the decisions behind the measurement setups and instruments are explained.

5.2.1   Paper II: Monostatic RCS

For Paper II, the monostatic RCS of a water-based electromagnetic device was measured. This was done using a vector network analyzer (VNA) connected to a horn antenna, and in an anechoic chamber to reduce the influence of unwanted scattering. However, the chamber was set up for antenna measurements and contained a large rotation stage for the purpose of angular scanning. This was not needed for the RCS measurements, but it posed a problem as it was difficult to remove from the chamber, and was a significant scatterer compared to the DUT. The DUT was mounted on a structure made from expanded polystyrene, which typically scatters very little [78]. The measurement setup is shown in Figure 24 for measurement of a metal-coated sphere of radius 20 cm. Background subtraction using reference measurements without the DUT were necessary to remove many unwanted reflections, with reflections from the antenna being particularly important to reduce. Further reductions of unwanted reflections were necessary though, both due to the antenna and due to the rotation stage. For the rotation stage, absorbers could be placed to cover structures exhibiting particularly
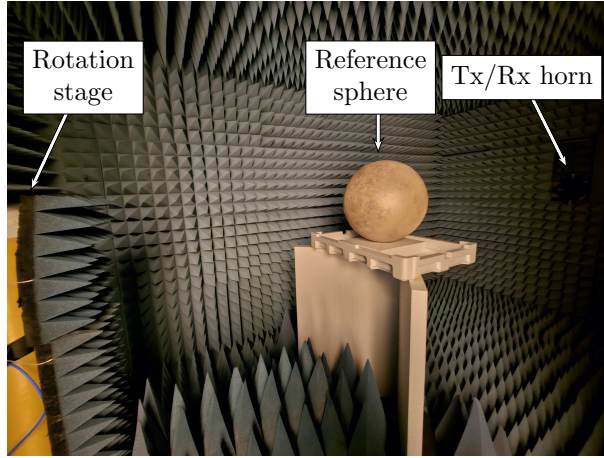
Figure 24: Measurement setup in anechoic chamber for a reference sphere. Absorbers as seen covering the rotation stage.

strong scattering like metallic corners. This had a significant effect, but did not fully eliminate the problem. Additional processing in the form of time gating was performed, which affected effects both due to the rotation stage and the antenna. This did require measurements in a larger frequency band, but since there was no mechanical scanning involved, measurement times were not large enough for this to pose any big issues.

Another issue which had to be addressed was that of noise. Measuring inside the anechoic chamber was an important part for this as it is a shielded environment, but the expected RCS was weak enough that further measures needed to be taken. One simple action was to increase the output power, which directly increases SNR. In addition to this, the bandwidth of the IF filter of the VNA was significantly reduced, and its selectivity increased, together with averaging over multiple measurements. These actions significantly increased the measurement time, but as previously discussed, this could be done to a large extent as no scanning was performed.

Finally, as RCS was the quantity to be measured it was crucial to perform an accurate calibration. Three different reference objects were used for this: one metal-coated sphere of radius 20 cm, one metallic sphere of radius 2.5 cm, and one metallic cylinder of height 8 cm and radius 2 cm. While the spheres had exact solutions for the RCS available, the RCS for the cylinder needed to be computed numerically, possibly introducing errors. However, as three different calibration objects were available, the cylinder measurements could be calibrated against a sphere to validate the numerical solution. The cylinder was eventually selected as the reference object, meaning that this intermediate step was used as indication that the final calibration could be trusted.
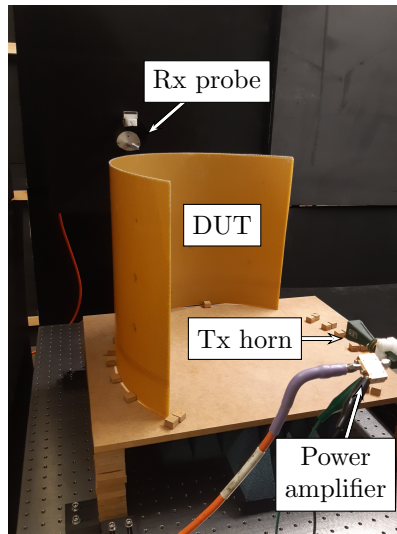
Figure 25: Setup for the mm-wave near-field scanning.

5.2.2   Paper IV: mm-Wave Near-Field Scanning

For Paper IV, near-field measurements were performed in a rectangular grid for use with the imaging algorithms described in section 4. This was done using a VNA connected to a Tx horn antenna and a mechanically scanned Rx open-ended waveguide probe. The measurement setup for a DUT mounted on a medium-density fiberboard table is shown in Figure 25. The measurements were performed on a metallic optical table, which meant that a very strong reflection in the table surface was present in the measured data, together with other unwanted scattering from holders and other surrounding objects. While absorbers could be placed in some locations, time gating was necessary to remove the effect of this reflection. Additionally, to increase the length of the reflection path and facilitate the time gating procedure, the Tx antenna, DUT and Rx probes were raised to a level significantly above the tabletop. To ensure that the time gating procedure would be effective, a large bandwidth of 10 GHz was used.

The measurements in this case were performed using mechanical scanning, and with high demands on precision in the positioning of the Rx probe. To ensure this precision, the mechanical positioning system was run with explicit stops at each measurement position, as opposed to measuring during the mechanical movement. The drawback of this is that acceleration and deceleration, as well as measurement time when the probe is stationary, makes the time for the full scan quite substantial. In the measurements, this time was roughly 7 h for 81×81 measurement points in a 300 mm × 300 mm plane. To boost the SNR without further increases to the measurement time (which would be a side-effect of changes to the IF bandwidth or averaging), an external power amplifier was used at the Tx antenna.
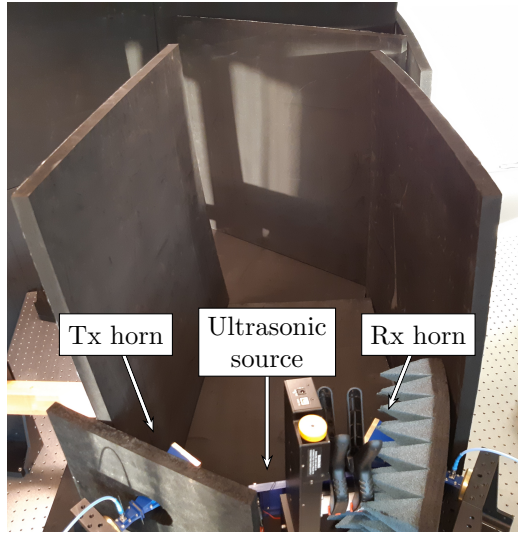
Figure 26: Setup for measurements of scattering by acoustic waves.

5.2.3 Paper V: Scattering by Acoustic Waves

For paper V, microwave scattering by an ultrasonic wave was measured. As this involved measuring a frequency shifted signal, the measurement was set up with a signal generator connected to a Tx antenna, and a separate spectrum analyzer connected to an Rx antenna. A different signal generator was needed for the ultrasonic source.

Since measurements were performed in air, the photoelastic interaction due to the ultrasonic wave was expected to be very weak. The Bragg diffraction mechanism described in section 2.5.1 had two crucial elements to enable measurements despite this difficulty. The first element was the clear scattering angle given by Bragg's law in (2.66), which could be selected by tuning the acoustic and electromagnetic wavelengths. As such, the scattering angle could be selected to place the Rx antenna outside the beam of the Tx antenna. The second, and most important element, was the frequency shift of scattered microwaves. By measuring at a frequency significantly separated from the Tx frequency, unwanted scattering would ideally not affect the measurements. This was clearly seen in the measurements as even the direct transmission between the horn gave a signal roughly 40 dB above the one scattered by ultrasound. Furthermore, this frequency shift provided a good way to verify that a measured signal was due to the ultrasonic wave as a shift in the ultrasonic frequency could immediately be seen to shift the measured microwave signal.

Despite the beneficial properties of the Bragg mechanism, unwanted scattering could still be problematic. No signal generator can provide a perfect single-frequency signal, and as the signal to be measured was very weak it was possible that the signal generator could produce significant enough levels at the frequency

shift of 40 kHz that was used. This would only be an issue if unwanted scattering was strong enough, and the main way this was reduced was by guiding the main beam away from the measurement region. Absorbers were used to enclose the measurement region, and care was taken to place them for specular reflections to guide the beam out of this region. This can be seen in Figure 26 where there is a path for waves to escape seen in the top of the figure.

Finally, due to the very low signal levels to be measured, noise reduction was crucial. The IF bandwidth of the signal generator was set to its minimum level of 10 Hz for this reason, and averaging over 10 measurements was also applied. These actions resulted in a noise floor below -130 dBm, which was sufficient to reliably measure the very weak scattering in air.

6   Contributions of Included Papers

As this dissertation is a compilation of papers, it is prudent to describe what their contributions are, and how they fit together in the bigger picture. The papers included in this dissertation can roughly be separated into two blocks: CEM software and NDT using mm-waves. However, there is still significant overlap between the two, especially with regards to integral equations which play an important role in both blocks.

6.1   Computational Electromagnetics Software

The first block is comprised of papers I–III and is about the development and use of the FE2MS software for electromagnetic scattering computations.

Paper I introduces the software which implements the FE-BI method combined with a multilevel ACA for improved performance. The paper has a particular focus on the development which was done with heavy use of open-source software, and aims to help readers who might want to work with open source by giving practical advice and insights. The FE-BI method is suitable for inhomogeneous, complex media and the software was developed to handle general bianisotropic media. The FE2MS software is itself open source, and is publicly available at https://www.github.com/nwingren/fe2ms. In the paper, there are also examples of how the software can be used, including details on accuracy and performance related to the commercial software Feko. However, all results are theoretical in the sense that they are either computed by computational software or the Mie series theoretical solution for scattering by spheres.

Paper II demonstrates that the FE2MS code can be used in realistic designs with complex geometry, and validates the results of the code against measured data. The paper presents a 3D-printed device which can be filled with water, and a siphon in the device causes given states to form as water is added. Depending on these states, the device reflects different microwave polarizations differently. While the device was primarily designed to act as a proof of concept for the use

of siphons, it is possible to imagine possible applications. By having a specific water volume trigger a sharp electromagnetic transition, it would be possible to remotely monitor water levels, or some property related to it. The design was simulated using the FE2MS software, and measurements were in good agreement with the simulated results. This demonstrates both that the software gives correct results for complicated geometries, and that it can be used in practical design work. While different materials were used in the siphon design, they were all isotropic, though the software can handle fully bianisotropic media.

Paper III uses the FE2MS software for computations involving a highly complex medium in a way that is unprecedented. The paper computes characteristic modes for structures involving nonreciprocity, which is something that has not been done previously. The application of the FE2MS software is for a rapidly rotating dielectric cylinder, which results in an effective medium which is inhomogeneous, bianisotropic and nonreciprocal. Conventional methods for computing characteristic modes are not easily adapted to this type of problem, but the FE-BI method is readily applied using a recently developed scattering formulation. The FE2MS software, in particular, is used due to its capability for bianisotropic media, which is not commonly found in commercial software.

6.2 Nondestructive Testing using mm-Waves

The second block is comprised of papers IV–V and is about using mm-waves to perform NDT of composite panels used in aerospace applications.

Paper IV uses methods from CEM to perform imaging of singly curved composite panels using mm-waves. This extends previous work on planar panels to this singly curved geometry, which finds several applications in aerodynamic structures. Significant modifications necessary to make the method work for the new geometry are presented. Additional details on theoretical concerns are considered in section 4.2 of this introduction. One point to notice is that, for the qualitative indications of discrete flaws investigated here, it was sufficient to use only electric currents instead of both electric and magnetic currents. This reduced the number of unknowns in the numerical problem by a factor of two. While mm-waves are promising for NDT, ultrasound is a commonly used method which works very well. For even better performance, one could ask if the two could be combined.

Paper V demonstrates how microwaves scattered by ultrasound in air can be clearly measured despite very low signal levels. While interaction between electromagnetic and acoustic waves is well-known, the literature is sparse when it comes to wavelengths of interest to NDT. In the paper we measure this interaction at wavelengths near those useful in NDT, but in air instead of the materials of interest. The scattering in air could be clearly measured to behave as predicted by theory, although at low signal levels. However, air is a medium with much weaker acousto-electromagnetic interaction than other media, and detection in air suggests that detection would be possible in most media. The main reason why

the detection could be made despite this difficulty was through the frequency shift of the scattered electromagnetic wave. This was done at an ultrasonic frequency of 40 kHz, which is fairly low compared to many industrial systems. An increase in the frequency shift, as well as the interaction strength itself could therefore be expected for a system used in NDT.

7   Conclusions

This dissertation has used both computational electromagnetics and measurements to investigate and evaluate electromagnetic scattering in its direct form and as an inverse problem. This is a large area to cover, and to draw any all-encompassing conclusions from my work is difficult. Nevertheless, some more general conclusions can be made where a topic has been covered by multiple papers with different approaches.

Both the FE2MS FE-BI code and the code used for imaging in Paper IV required substantial amounts of implementation work on my part. However, the starting points were quite different for the two. At the start of the development of the FE2MS code, there was no preexisting codebase to build upon. At that stage, I was very free in exploring various open-source packages which could be used to accelerate the development process. For the imaging code, on the other hand, a working code for planar imaging was already in place before I started working on extending it to singly curved imaging. In that case, there were very few opportunities where the integration of an open-source software package could have provided significant help. These two, somewhat opposed, situations tell us about the difficulty in integrating external software packages as a code matures. This can depend on the code architecture though, as it would have been fairly simple to change the optimization routine in the imaging code, but less so for the mesh handling. The reason is that the optimization was already an external open-source package, and the code around it was adapted to this. If more of the code architecture is designed for such modularity at an early stage, the challenge of integrating other code components might be smaller.

The benefits of simulation codes with direct access to the source code was also clear from the work shown in the dissertation. While commercial codes can be very capable, it is typically not possible to access all lower-level components, let alone the source code. The use of in-house codes like the FE2MS code allows for significant modifications in many cases. Before the work leading up to Paper III, the FE2MS code was only implemented with isotropic media in mind. When the interest for nonreciprocal media became clear, it was possible to change the implementation of FE forms for general bianisotropic media, and this could be done quickly with the help of FEniCSx. The algorithm computing characteristic modes could also be implemented with direct access to lower-level functions in the FE2MS code, making computations much faster than if only the high-level functions had been used. A hope is that the FE2MS code can be used in similar manners for other applications in the future, both within our research group, but

also in a wider context since the code is publicly available.

While much of the work performed for this dissertation focused on time-harmonic waves considered at single frequencies, a curious topic of frequency shifts became important in both Paper III and Paper V. In Paper III, the rotation of a cylinder affected its characteristic modes by shifting the resonance frequencies of certain modes, with the shift increasing with faster rotation. In Paper V, measurements of microwaves scattered by ultrasound was largely made possible through a frequency shift by the ultrasonic frequency. Both of these examples consider moving media in some form, and it is seen that interesting phenomena arise, which are not present in the stationary case. These phenomena are both due to fairly simple forms of movement, but illustrate why it is so interesting to pursue more complex ways of modulating media in time and space.

7.1   Future Work

There are many possible ways to further improve the FE2MS code presented in Paper I. One extension with much promise, which has been hinted towards in this introduction, would be the implementation of a fast direct solution method. A good reason for this is that the FE-BI system is typically ill-conditioned and needs an expensive preconditioner for iterative solvers to converge. This is computationally expensive, both in time and memory, and this issue is avoided if direct methods are used. Furthermore, such methods would be highly useful for problems with many right-hand sides as they only need to be solved once, in contrast to once per right-hand side for iterative solvers. Fast direct methods are well established for fully dense systems such as those in MoM, but less work has been done for the partly sparse, partly dense FE-BI system. Another improvement to the code which would increase its applicability would be to adapt it to distributed computing on clusters. While the code has some elements of parallel execution, the main drawback of the current approach is that there is no implementation for distributed memory. To be able to handle truly large problems, this would be necessary. Looking at the scaling of different parts of the FE-BI system, the BI part would likely be the part where this is necessary first, even with compression of the BI blocks. Some of the support in FEniCSx for distributed memory might be useful since some of its functionality, like mesh handling, are used in the BI part.

The water-based scatterer shown in Paper II was presented mainly as a proof of concept for the use of siphons for reconfigurability in water-based devices. It would be interesting if siphons, like the self-priming siphon used in our design, could be used in other devices with other applications. While our device would possibly enable some types of polarization-based remote measurements of whether a specific amount of water had been collected, there are likely other applications that could benefit from using siphons. Compared to other ways of controlling water for use in electromagnetic devices like pumps, siphons are mechanically simple, robust, and require no moving parts or external power. This

could make them interesting in, for example, environments where use of pumps would be difficult.

For the use of characteristic modes in problems exhibiting nonreciprocity shown in Paper III, the work presented here is in a very early stage. To our knowledge, this has not been attempted before, and as such there could be many ways in which to proceed. In the paper, the examples are mostly presented to demonstrate that it is in fact possible to compute modes for these problems, but less so to demonstrate particularly practical problems where characteristic modes might help. It would be good to identify such problems in future work. Since there is a large interest in devices with modulation in space and time, possibly with nonreciprocal behavior, the use of characteristic modes could be of interest. Especially the identification of modes which exhibit nonreciprocal behavior and modes which do not, as seen in Paper III, could be of interest when designing devices which should be explicitly nonreciprocal.

The mm-wave imaging algorithm for NDT presented in Paper IV could be improved upon in some different ways. One interesting development would be to use multi-frequency data in the reconstruction. The current algorithm uses only single-frequency data for that step, although multi-frequency data is collected in measurements for use in the time gating procedure. A hope would be that by using data for multiple frequencies, the number of spatial data points could be reduced. Experiments with multi-frequency data in the current algorithm have not produced good results, indicating that the problem formulation may need to change in that case. Another idea, which would follow the planar imaging algorithm, is to extend the algorithm from transmission- to reflection-based measurements. This was done for planar imaging using a ground plane and the theory of image currents, but the same method was not immediately applicable to imaging of singly curved surfaces. A more recent development which could be interesting to explore is that of large array-based measurement systems. With the arrival of 5G and more mm-wave systems to the market, such measurement systems have become more common. The largest bottleneck of the NDT method in Paper IV is the mechanical near-field scanning which took roughly 7 h for the measurements in the paper. With a one-dimensional array this time would be drastically reduced, and with a two-dimensional array it would, for all practical purposes, be eliminated.

With regards to Paper V and interaction between acoustic and electromagnetic waves, an interesting path for future work would be to investigate the interaction in some other medium than air, where the NDT application might be explored. For sufficiently high resolution in such an application, the wavelengths of both electromagnetic and acoustic waves may need to be smaller. Due to a likely higher propagation speed for acoustic waves in the medium, the ultrasonic frequency would then have to be significantly higher, requiring another type of transducer. There could also be some challenges for how to insert the waves into the medium, particularly for the ultrasonic waves. In many applications, they are guided into denser samples using water or gels at the interface, but the question is how that affects the microwave scattering.

Appendix A   Derivations

A.1   Weak Form for Media without Magnetoelectric Coupling

This derivation begins with the vector wave equation as written in (3.3). A weak form can be derived for this by multiplying (3.3) by a test function $\boldsymbol{W}_m$ and an integrating over Ω, giving

$$\int_\Omega \boldsymbol{W}_m \cdot \left[\nabla \times \left(\overline{\overline{\mu_\mathrm{r}}}^{-1} \cdot \nabla \times \boldsymbol{E} \right) - k_0^2 \overline{\overline{\varepsilon_\mathrm{r}}} \cdot \boldsymbol{E} \right] \mathrm{d}V = -\mathrm{j}k_0\eta_0 \int_\Omega \boldsymbol{W}_m \cdot \boldsymbol{J}\,\mathrm{d}V. \quad (\text{A.1})$$

The curl can be transferred to the test function by using the identity

$$\nabla \cdot (\boldsymbol{A} \times \boldsymbol{B}) = (\nabla \times \boldsymbol{A}) \cdot \boldsymbol{B} - (\nabla \times \boldsymbol{B}) \cdot \boldsymbol{A} \quad (\text{A.2})$$

giving

$$\int_\Omega \left[(\nabla \times \boldsymbol{W}_m) \cdot \left(\overline{\overline{\mu_\mathrm{r}}}^{-1} \cdot \nabla \times \boldsymbol{E} \right) - k_0^2 \boldsymbol{W}_m \cdot \overline{\overline{\varepsilon_\mathrm{r}}} \cdot \boldsymbol{E} \right] \mathrm{d}V$$
$$- \int_\Omega \nabla \cdot \left[\boldsymbol{W}_m \times \left(\overline{\overline{\mu_\mathrm{r}}}^{-1} \cdot \nabla \times \boldsymbol{E} \right) \right] \mathrm{d}V = -\mathrm{j}k_0\eta_0 \int_\Omega \boldsymbol{W}_m \cdot \boldsymbol{J}\,\mathrm{d}V. \quad (\text{A.3})$$

The second integral is now rewritten using the divergence theorem, giving the weak form as

$$\int_\Omega \left[(\nabla \times \boldsymbol{W}_m) \cdot \left(\overline{\overline{\mu_\mathrm{r}}}^{-1} \cdot \nabla \times \boldsymbol{E} \right) - k_0^2 \boldsymbol{W}_m \cdot \overline{\overline{\varepsilon_\mathrm{r}}} \cdot \boldsymbol{E} \right] \mathrm{d}V$$
$$+ \oint_{\partial\Omega} \boldsymbol{W}_m \cdot \left[\hat{\boldsymbol{n}} \times \left(\overline{\overline{\mu_\mathrm{r}}}^{-1} \cdot \nabla \times \boldsymbol{E} \right) \right] \mathrm{d}S = -\mathrm{j}k_0\eta_0 \int_\Omega \boldsymbol{W}_m \cdot \boldsymbol{J}\,\mathrm{d}V. \quad (\text{A.4})$$

If the boundary condition from (2.16) is used on the external boundary, i.e.

$$\hat{\boldsymbol{n}} \times \left(\overline{\overline{\mu_\mathrm{r}}}^{-1} \cdot \nabla \times \boldsymbol{E} \right) = -\mathrm{j}k_0 \hat{\boldsymbol{n}} \times \bar{\boldsymbol{H}}, \ \boldsymbol{r} \in \partial\Omega \quad (\text{A.5})$$

the surface integral in the weak form can be replaced. This gives a weak form for the interior FE problem for the FE-BI formulation as

$$\int_\Omega \left[(\nabla \times \boldsymbol{W}_m) \cdot \left(\overline{\overline{\mu_\mathrm{r}}}^{-1} \cdot \nabla \times \boldsymbol{E} \right) - k_0^2 \boldsymbol{W}_m \cdot \overline{\overline{\varepsilon_\mathrm{r}}} \cdot \boldsymbol{E} \right] \mathrm{d}V$$
$$+ \mathrm{j}k_0 \oint_{\partial\Omega} \hat{\boldsymbol{n}} \cdot \left(\boldsymbol{W}_m \times \bar{\boldsymbol{H}} \right) \mathrm{d}S = -\mathrm{j}k_0 \int_\Omega \boldsymbol{W}_m \cdot \bar{\boldsymbol{J}}\,\mathrm{d}V. \quad (\text{A.6})$$

A.2   Weak Form for Media with Magnetoelectric Coupling

This derivation begins with Maxwell's equations on the form in (3.5)–(3.6). These are combined in a similar way as for the case without magnetoelectric interaction, giving

$$
\nabla \times \left(\overline{\overline{\mu_r}}^{-1} \cdot \nabla \times \boldsymbol{E} \right) = -\mathrm{j}\omega\mu_0 \left[\frac{1}{\eta_0} \nabla \times \left(\overline{\overline{\mu_r}}^{-1} \cdot \overline{\overline{\zeta}} \cdot \boldsymbol{E} \right) + \boldsymbol{J} + \mathrm{j}\omega\varepsilon_0\overline{\overline{\varepsilon_r}} \cdot \boldsymbol{E} \right.
$$
$$
\left. - \varepsilon_0\eta_0\overline{\overline{\xi}} \cdot \left(\frac{1}{\mu_0}\overline{\overline{\mu_r}} \cdot \nabla \times \boldsymbol{E} + \mathrm{j}\omega\frac{1}{\eta_0}\overline{\overline{\mu_r}}^{-1} \cdot \overline{\overline{\zeta}} \cdot \boldsymbol{E} \right) \right]. \quad \text{(A.7)}
$$

Rearranging and rewriting gives the equation corresponding to the previous vector wave equation as.

$$
\nabla \times \left(\overline{\overline{\mu_r}}^{-1} \cdot \nabla \times \boldsymbol{E} \right) - k_0^2 \left(\overline{\overline{\varepsilon_r}} - \overline{\overline{\xi}} \cdot \overline{\overline{\mu_r}}^{-1} \cdot \overline{\overline{\zeta}} \right) \cdot \boldsymbol{E}
$$
$$
+ \mathrm{j}k_0 \left[\nabla \times \left(\overline{\overline{\mu_r}}^{-1} \cdot \overline{\overline{\zeta}} \cdot \boldsymbol{E} \right) - \overline{\overline{\xi}} \cdot \overline{\overline{\mu_r}}^{-1} \cdot \nabla \times \boldsymbol{E} \right] = -\mathrm{j}k_0\eta_0\boldsymbol{J}. \quad \text{(A.8)}
$$

Using the same steps as for media without magnetoelectric coupling, the weak form can also be derived. Multiplication by a test function $\boldsymbol{W}_m$ and integration over Ω gives

$$
\int_\Omega \boldsymbol{W}_m \cdot \left[\nabla \times \left(\overline{\overline{\mu_r}}^{-1} \cdot \nabla \times \boldsymbol{E} \right) \right] \mathrm{d}V + \mathrm{j}k_0 \int_\Omega \boldsymbol{W}_m \cdot \left[\nabla \times \left(\overline{\overline{\mu_r}}^{-1} \cdot \overline{\overline{\zeta}} \cdot \boldsymbol{E} \right) \right] \mathrm{d}V
$$
$$
- \mathrm{j}k_0 \int_\Omega \boldsymbol{W}_m \cdot \left(\overline{\overline{\xi}} \cdot \overline{\overline{\mu_r}}^{-1} \cdot \nabla \times \boldsymbol{E} \right) \mathrm{d}V - k_0^2 \int_\Omega \boldsymbol{W}_m \cdot \left(\overline{\overline{\varepsilon_r}} - \overline{\overline{\xi}} \cdot \overline{\overline{\mu_r}}^{-1} \cdot \overline{\overline{\zeta}} \right) \cdot \boldsymbol{E} \, \mathrm{d}V
$$
$$
= -\mathrm{j}k_0\eta_0 \int_\Omega \boldsymbol{W}_m \cdot \boldsymbol{J} \, \mathrm{d}V. \quad \text{(A.9)}
$$

The first integral is the same as for the problem without magnetoelectric coupling, and is rewritten in the same way as

$$
\int_\Omega \boldsymbol{W}_m \cdot \left[\nabla \times \left(\overline{\overline{\mu_r}}^{-1} \cdot \nabla \times \boldsymbol{E} \right) \right] \mathrm{d}V
$$
$$
= \int_\Omega (\nabla \times \boldsymbol{W}_m) \cdot \left(\overline{\overline{\mu_r}}^{-1} \cdot \nabla \times \boldsymbol{E} \right) \mathrm{d}V + \oint_{\partial\Omega} \boldsymbol{W}_m \cdot \left[\hat{\boldsymbol{n}} \times \left(\overline{\overline{\mu_r}}^{-1} \cdot \nabla \times \boldsymbol{E} \right) \right] \mathrm{d}S.
$$
$$
\text{(A.10)}
$$

The second integral is treated similarly as

$$
\int_\Omega \boldsymbol{W}_m \cdot \left[\nabla \times \left(\overline{\overline{\mu_r}}^{-1} \cdot \overline{\overline{\zeta}} \cdot \boldsymbol{E} \right) \right] \mathrm{d}V
$$
$$
= \int_\Omega (\nabla \times \boldsymbol{W}_m) \cdot \overline{\overline{\mu_r}}^{-1} \cdot \overline{\overline{\zeta}} \cdot \boldsymbol{E} \, \mathrm{d}V - \int_\Omega \nabla \cdot \left[\boldsymbol{W}_m \times \left(\overline{\overline{\mu_r}}^{-1} \cdot \overline{\overline{\zeta}} \cdot \boldsymbol{E} \right) \right] \mathrm{d}V
$$
$$
= \int_\Omega (\nabla \times \boldsymbol{W}_m) \cdot \overline{\overline{\mu_r}}^{-1} \cdot \overline{\overline{\zeta}} \cdot \boldsymbol{E} \, \mathrm{d}V - \oint_{\partial\Omega} \hat{\boldsymbol{n}} \cdot \left[\boldsymbol{W}_m \times \left(\overline{\overline{\mu_r}}^{-1} \cdot \overline{\overline{\zeta}} \cdot \boldsymbol{E} \right) \right] \mathrm{d}S \quad \text{(A.11)}
$$

where (A.2) and the divergence theorem were used. A weak form can be written as

$$
\int_{\Omega} (\nabla \times \boldsymbol{W}_m) \cdot \left(\overline{\overline{\mu_{\mathrm{r}}}}^{-1} \cdot \nabla \times \boldsymbol{E} \right) \mathrm{d}V - k_0^2 \int_{\Omega} \boldsymbol{W}_m \cdot \left(\overline{\overline{\varepsilon_{\mathrm{r}}}} - \overline{\overline{\xi}} \cdot \overline{\overline{\mu_{\mathrm{r}}}}^{-1} \cdot \overline{\overline{\zeta}} \right) \cdot \boldsymbol{E} \, \mathrm{d}V
$$

$$
+ \mathrm{j}k_0 \int_{\Omega} (\nabla \times \boldsymbol{W}_m) \cdot \overline{\overline{\mu_{\mathrm{r}}}}^{-1} \cdot \overline{\overline{\zeta}} \cdot \boldsymbol{E} \, \mathrm{d}V - \mathrm{j}k_0 \int_{\Omega} \boldsymbol{W}_m \cdot \left(\overline{\overline{\xi}} \cdot \overline{\overline{\mu_{\mathrm{r}}}}^{-1} \cdot \nabla \times \boldsymbol{E} \right) \mathrm{d}V
$$

$$
+ \oint_{\partial\Omega} \boldsymbol{W}_m \cdot \left[\hat{\boldsymbol{n}} \times \left(\overline{\overline{\mu_{\mathrm{r}}}}^{-1} \cdot \nabla \times \boldsymbol{E} \right) \right] \mathrm{d}S - \mathrm{j}k_0 \oint_{\partial\Omega} \hat{\boldsymbol{n}} \cdot \left[\boldsymbol{W}_m \times \left(\overline{\overline{\mu_{\mathrm{r}}}}^{-1} \cdot \overline{\overline{\zeta}} \cdot \boldsymbol{E} \right) \right] \mathrm{d}S
$$

$$
= -\mathrm{j}k_0 \eta_0 \int_{\Omega} \boldsymbol{W}_m \cdot \boldsymbol{J} \, \mathrm{d}V. \quad \text{(A.12)}
$$

As for the simpler case in A.1, the boundary condition from (2.16) is used on the external boundary to give a new weak form. In this case, the boundary condition appears explicitly only in one surface integral, but some more effort is required to include it in the second one. This second surface integral can be written as

$$
-\mathrm{j}k_0 \oint_{\partial\Omega} \boldsymbol{W}_m \cdot \left[\hat{\boldsymbol{n}} \times \left(\overline{\overline{\mu_{\mathrm{r}}}}^{-1} \cdot \overline{\overline{\zeta}} \cdot \boldsymbol{E} \right) \right] \mathrm{d}S. \quad \text{(A.13)}
$$

This can be rewritten using (3.5) written as

$$
-\mathrm{j}k_0 \overline{\overline{\mu_{\mathrm{r}}}}^{-1} \cdot \overline{\overline{\zeta}} \cdot \boldsymbol{E} = \overline{\overline{\mu_{\mathrm{r}}}}^{-1} \cdot \nabla \times \boldsymbol{E} + \mathrm{j}k_0 \bar{\boldsymbol{H}} \quad \text{(A.14)}
$$

giving the surface integral as

$$
\oint_{\partial\Omega} \boldsymbol{W}_m \cdot \left[\hat{\boldsymbol{n}} \times \left(\overline{\overline{\mu_{\mathrm{r}}}}^{-1} \cdot \nabla \times \boldsymbol{E} \right) + \mathrm{j}k_0 \hat{\boldsymbol{n}} \times \bar{\boldsymbol{H}} \right] \mathrm{d}S. \quad \text{(A.15)}
$$

This can be identified in the boundary condition, showing that the second surface integral is identically zero. Now the final weak form can be written as

$$
\int_{\Omega} (\nabla \times \boldsymbol{W}_m) \cdot \left(\overline{\overline{\mu_{\mathrm{r}}}}^{-1} \cdot \nabla \times \boldsymbol{E} \right) \mathrm{d}V - k_0^2 \int_{\Omega} \boldsymbol{W}_m \cdot \left(\overline{\overline{\varepsilon_{\mathrm{r}}}} - \overline{\overline{\xi}} \cdot \overline{\overline{\mu_{\mathrm{r}}}}^{-1} \cdot \overline{\overline{\zeta}} \right) \cdot \boldsymbol{E} \, \mathrm{d}V
$$

$$
+ \mathrm{j}k_0 \int_{\Omega} (\nabla \times \boldsymbol{W}_m) \cdot \overline{\overline{\mu_{\mathrm{r}}}}^{-1} \cdot \overline{\overline{\zeta}} \cdot \boldsymbol{E} \, \mathrm{d}V - \mathrm{j}k_0 \int_{\Omega} \boldsymbol{W}_m \cdot \left(\overline{\overline{\xi}} \cdot \overline{\overline{\mu_{\mathrm{r}}}}^{-1} \cdot \nabla \times \boldsymbol{E} \right) \mathrm{d}V
$$

$$
+ \mathrm{j}k_0 \oint_{\partial\Omega} \hat{\boldsymbol{n}} \cdot \left(\boldsymbol{W}_m \times \bar{\boldsymbol{H}} \right) \mathrm{d}S = -\mathrm{j}k_0 \int_{\Omega} \boldsymbol{W}_m \cdot \bar{\boldsymbol{J}} \, \mathrm{d}V. \quad \text{(A.16)}
$$

References

[1] Acconeer. Applications. https://www.acconeer.com/applications/. Accessed 7 Feb. 2024.

[2] S. S. Ahmed, A. Schiessl, F. Gumbmann, M. Tiebout, S. Methfessel, and L. Schmidt. Advanced microwave imaging. *IEEE Microwave Magazine*, **13**(6), pp. 26–43, 2012.

[3] M. S. Alnæs, A. Logg, K. B. Ølgaard, M. E. Rognes, and G. N. Wells. Unified form language: A domain-specific language for weak formulations of partial differential equations. *ACM Transactions on Mathematical Software*, **40**(2), 2014.

[4] Altair Engineering Inc. Electromagnetic Simulation for Connectivity, Compatibility, and Radar | Altair Feko. https://altair.com/feko. Accessed 2 Feb. 2024.

[5] P. R. Amestoy, I. S. Duff, J.-Y. L'Excellent, and J. Koster. A fully asynchronous multifrontal solver using distributed dynamic scheduling. *SIAM Journal on Matrix Analysis and Applications*, **23**(1), pp. 15–41, 2001.

[6] J. B. Andersen. History of communications/radio wave propagation from Marconi to MIMO. *IEEE Communications Magazine*, **55**(2), pp. 6–10, 2017.

[7] F. P. Andriulli, K. Cools, H. Bagci, F. Olyslager, A. Buffa, S. Christiansen, and E. Michielssen. A multiplicative calderon preconditioner for the electric field integral equation. *IEEE Transactions on Antennas and Propagation*, **56**(8), pp. 2398–2412, 2008.

[8] P. Arcioni, M. Bressan, and L. Perregrini. On the evaluation of the double surface integrals arising in the application of the boundary integral method to 3-D problems. *IEEE Transactions on Microwave Theory and Techniques*, **45**(3), pp. 436–439, 1997.

[9] Axis Communications. Radar in surveillance. White Paper, 2023. https://www.axis.com/dam/public/ae/b8/7d/radar-in-surveillance-en-US-407095.pdf. Accessed 7 Feb. 2024.

[10] I. Badia, B. Caudron, X. Antoine, and C. Geuzaine. A well-conditioned weak coupling of boundary element and high-order finite element methods for time-harmonic electromagnetic scattering by inhomogeneous objects. *SIAM Journal on Scientific Computing*, **44**(3), pp. B640–B667, 2022.

[11] C. A. Balanis. *Antenna Theory: analysis and design*. John Wiley & Sons, Inc., 2nd edition, 1997.

[12] L. Baldini and V. Chandrasekar. *100 Years of the International Union of Radio Science*, chapter 24: Commission F Contribution: Radio Wave Remote Sensing of the Earth, pp. 499–518. URSI Press, Gent, Belgium, 2021.

[13] I. A. Baratta, J. P. Dean, J. S. Dokken, M. Habera, J. S. Hale, C. N. Richardson, M. E. Rognes, M. W. Scroggs, N. Sime, and G. N. Wells. DOLFINx: The next generation FEniCS problem solving environment, 2023.

[14] J. Barnes and P. Hut. A hierarchical O(N log N) force-calculation algorithm. *Nature*, **324**(6096), pp. 446–449, 1986.

[15] M. Bebendorf and S. Kunis. Recompression techniques for adaptive cross approximation. *The Journal of Integral Equations and Applications*, **21**(3), pp. 331–357, 2009.

[16] M. Bebendorf. Approximation of boundary element matrices. *Numerische Mathematik*, **86**(4), pp. 565–589, 2000.

[17] M. Bebendorf. *Hierarchical Matrices*. Springer-Verlag, Berlin, Heidelberg, Germany, 2008.

[18] J. Bezanson, A. Edelman, S. Karpinski, and V. B. Shah. Julia: A fresh approach to numerical computing. *SIAM Review*, **59**(1), pp. 65–98, 2017.

[19] E. Bleszynski, M. Bleszynski, and T. Jaroszewicz. AIM: Adaptive integral method for solving large-scale electromagnetic scattering and radiation problems. *Radio Science*, **31**(5), pp. 1225–1251, 1996.

[20] W. H. Bragg and W. L. Bragg. The reflection of X-rays by crystals. *Proceedings of the Royal Society of London. Series A, Containing Papers of a Mathematical and Physical Character*, **88**(605), pp. 428–438, 1913.

[21] S. C. Brenner and L. R. Scott. *The Mathematical Theory of Finite Element Methods*. Springer Science+Business Media, New York, NY, USA, 3rd edition, 2008.

[22] L. Brillouin. Diffusion de la lumière et des rayons X par un corps transparent homogène - influence de l'agitation thermique. *Annales de Physique*, **9**(17), pp. 88–122, 1922.

[23] A. Buffa and S. Christiansen. A dual finite element complex on the barycentric refinement. *Mathematics of computation*, **76**(260), pp. 1743–1769, 2007.

[24] G. J. Burke and A. J. Poggio. Numerical electromagnetic code (NEC)-method of moments. NOSC Technical Document 116, Naval Ocean Systems Center, San Diego, CA, 1977.

[25] G. Burke, E. Miller, and A. Poggio. The numerical electromagnetics code (NEC) - a brief history. In *IEEE Antennas and Propagation Society Symposium, 2004.*, volume 3, pp. 2871–2874, 2004.

[26] M. Cabedo-Fabres, E. Antonino-Daviu, A. Valero-Nogueira, and M. F. Bataller. The theory of characteristic modes revisited: A contribution to the design of antennas for modern applications. *IEEE Antennas and Propagation Magazine*, **49**(5), pp. 52–68, 2007.

[27] C. Caloz and Z.-L. Deck-Léger. Spacetime metamaterials—part I: General concepts. *IEEE Transactions on Antennas and Propagation*, **68**(3), pp. 1569–1582, 2020.

[28] M. Capek, J. Lundgren, M. Gustafsson, K. Schab, and L. Jelinek. Characteristic mode decomposition using the scattering dyadic in arbitrary full-wave solvers. *IEEE Transactions on Antennas and Propagation*, **71**(1), pp. 830–839, 2023.

[29] M. Catedra, J. Cuevas, and L. Nuno. A scheme to analyze conducting plates of resonant size using the conjugate-gradient method and the fast Fourier transform. *IEEE Transactions on Antennas and Propagation*, **36**(12), pp. 1744–1752, 1988.

[30] M. Catedra, E. Gago, and L. Nuno. A numerical scheme to obtain the RCS of three-dimensional bodies of resonant size using the conjugate gradient method and the fast Fourier transform. *IEEE Transactions on Antennas and Propagation*, **37**(5), pp. 528–537, 1989.

[31] V. C. Chen, F. Li, S. . Ho, and H. Wechsler. Micro-doppler effect in radar: phenomenon, model, and simulation study. *IEEE Transactions on Aerospace and Electronic Systems*, **42**(1), pp. 2–21, 2006.

[32] W. C. Chew, M. S. Tong, and B. Hu. *Integral Equation Methods for Electromagnetic and Elastic Waves*, volume 12 of *Synthesis Lectures on Computational Electromagnetics*. Morgan & Claypool, 2008.

[33] R. Coifman, V. Rokhlin, and S. Wandzura. The fast multipole method for the wave equation: a pedestrian prescription. *IEEE Antennas and Propagation Magazine*, **35**(3), pp. 7–12, 1993.

[34] K. Cools, F. P. Andriulli, D. De Zutter, and E. Michielssen. Accurate and conforming mixed discretization of the MFIE. *IEEE Antennas and Wireless Propagation Letters*, **10**, pp. 528–531, 2011.

[35] D. B. Davidson. *Computational Electromagnetics for RF and Microwave Engineering*. Cambridge University Press, Cambridge, UK, 2 edition, 2011.

[36] T. A. Davis. Algorithm 832: UMFPACK V4.3—an unsymmetric-pattern multifrontal method. *ACM Transactions on Mathematical Software*, **30**(2), pp. 196–199, 2004.

[37] T. H. Demetrakopoulos and R. Mittra. Digital and optical reconstruction of images from suboptical diffraction patterns. *Applied Optics*, **13**(3), pp. 665–670, 1974.

[38] L. F. Demkowicz. *Mathematical Theory of Finite Elements*. Society for Industrial and Applied Mathematics, Philadelphia, PA, USA, 2024.

[39] M. G. Duffy. Quadrature over a pyramid or cube of integrands with a singularity at a vertex. *SIAM journal on Numerical Analysis*, **19**(6), pp. 1260–1262, 1982.

[40] T. Eibert and V. Hansen. On the calculation of potential integrals for linear source distributions on triangular domains. *IEEE Transactions on Antennas and Propagation*, **43**(12), pp. 1499–1502, 1995.

[41] A. Ericsson, D. Sjöberg, C. Larsson, and T. Martin. Scattering from a multilayered sphere - applications to electromagnetic absorbers on double curved surfaces. Technical Report LUTEDX/(TEAT-7249)/1-32/(2017), Electromagnetic Theory Department of Electrical and Information Technology Lund University Sweden, 2017.

[42] M. Fink. Multiwave imaging and super resolution. *Physics Today*, **63**(2), pp. 28, 2010.

[43] H. Gan and W. Chew. A discrete BCG-FFT algorithm for solving 3D inhomogeneous scatterer problems. *Journal of Electromagnetic Waves and Applications*, **9**(10), pp. 1339–1357, 1995.

[44] R. J. Garbacz. *A Generalized Expansion for Radiated and Scattered Fields*. PhD thesis, The Ohio State Univ., 1968.

[45] C. Geuzaine and J.-F. Remacle. Gmsh: A 3-D finite element mesh generator with built-in pre-and post-processing facilities. *International journal for numerical methods in engineering*, **79**(11), pp. 1309–1331, 2009.

[46] V. Girault and P.-A. Raviart. *Finite Element Methods for Navier-Stokes Equations*. Springer-Verlag, Berlin, Heidelberg, Germany, 1986.

[47] G. H. Golub and C. F. V. Loan. *Matrix Computations*. Johns Hopkins University Press, Baltimore, MD, USA, 3rd edition, 1996.

[48] R. Graglia. On the numerical integration of the linear shape functions times the 3-D Green's function or its gradient on a plane triangle. *IEEE Transactions on Antennas and Propagation*, **41**(10), pp. 1448–1455, 1993.

[49] J. Guan, S. Yan, and J. Jin. An accurate and efficient finite element-boundary integral method with GPU acceleration for 3-D electromagnetic analysis. *IEEE Transactions on Antennas and Propagation*, **62**(12), pp. 6325–6336, 2014.

[50] J. Guan, S. Yan, and J. Jin. A multi-solver scheme based on combined field integral equations for electromagnetic modeling of highly complex objects. *IEEE Transactions on Antennas and Propagation*, **65**(3), pp. 1236–1247, 2017.

[51] H. Guo, Y. Liu, J. Hu, and E. Michielssen. A butterfly-based direct integral-equation solver using hierarchical LU factorization for analyzing scattering from electrically large conducting objects. *IEEE Transactions on Antennas and Propagation*, **65**(9), pp. 4742–4750, 2017.

[52] M. Gustafsson, M. Sebesta, B. Bengtsson, S. Pettersson, P. Egelberg, and T. Lenart. High-resolution digital transmission microscopy—a Fourier holography approach. *Optics and Lasers in Engineering*, **41**(3), pp. 553–563, 2004.

[53] M. Gustafsson, L. Jelinek, K. Schab, and M. Capek. Unified theory of characteristic modes: Part I – Fundamentals. *IEEE Transactions on Antennas and Propagation*, **70**(12), pp. 11814–11824, 2022.

[54] M. Gustafsson, L. Jelinek, K. Schab, and M. Capek. Unified theory of characteristic modes: Part II – Tracking, losses, and FEM evaluation. *IEEE Transactions on Antennas and Propagation*, **70**(12), pp. 11814–11824, 2022.

[55] W. Hackbusch. *Hierarchical Matrices: Algorithms and Analysis.* Springer-Verlag, Berlin, Heidelberg, Germany, 2015.

[56] P. C. Hansen. *Discrete Inverse Problems : Insight and Algorithms.* Society for Industrial and Applied Mathematics, Philadelphia, PA, USA, 2010.

[57] R. F. Harrington and J. R. Mautz. Theory of characteristic modes for conducting bodies. *IEEE Transactions on Antennas and Propagation*, **19**(5), pp. 622–628, 1971.

[58] R. F. Harrington. *Time-Harmonic Electromagnetic Fields.* Wiley – IEEE Press, 2001.

[59] C. R. Harris, K. J. Millman, S. J. van der Walt, R. Gommers, P. Virtanen, D. Cournapeau, E. Wieser, J. Taylor, S. Berg, N. J. Smith, R. Kern, M. Picus, S. Hoyer, M. H. van Kerkwijk, M. Brett, A. Haldane, J. F. del Río, M. Wiebe, P. Peterson, P. Gérard-Marchant, K. Sheppard, T. Reddy, W. Weckesser, H. Abbasi, C. Gohlke, and T. E. Oliphant. Array programming with NumPy. *Nature*, **585**(7825), pp. 357–362, 2020.

[60] J. Helander, A. Ericsson, M. Gustafsson, T. Martin, D. Sjöberg, and C. Larsson. Compressive sensing techniques for mm-wave nondestructive testing of composite panels. *IEEE Transactions on Antennas and Propagation*, **65**(10), pp. 5523–5531, 2017.

[61] J. Helander, J. Lundgren, D. Sjöberg, C. Larsson, T. Martin, and M. Gustafsson. Reflection-based source inversion for sparse imaging of low-loss composite panels. *IEEE Transactions on Antennas and Propagation*, **68**(6), pp. 4860–4870, 2020.

[62] J. Helander. *Millimeter Wave Imaging and Phased Array Antennas for 5G and Aerospace Applications*. Doctoral thesis (compilation), Department of Electrical and Information Technology, Lund University, 2019.

[63] J. Helander, D. Tayli, and D. Sjöberg. Synthesis of large endfire antenna arrays using convex optimization. *IEEE Transactions on Antennas and Propagation*, **66**(2), pp. 712–720, 2018.

[64] A. D. Helfrick. *Electrical spectrum and network analyzers: a practical approach*. Academic Press, Inc., San Diego, CA, USA, 1991.

[65] L. Hernquist. Hierarchical N-body methods. *Computer Physics Communications*, **48**(1), pp. 107–115, 1988.

[66] L. Hörmander. *The Analysis of Linear Partial Differential Operators I: Distribution theory and Fourier analysis*. Springer-Verlag, Berlin, Heidelberg, Germany, 2nd edition, 1990.

[67] Infineon Technologies. Radar sensors for IoT. https://www.infineon.com/cms/en/product/sensor/radar-sensors/radar-sensors-for-iot/. Accessed 7 Feb. 2024.

[68] J. D. Jackson. *Classical Electrodynamics*. John Wiley & Sons, Inc., Hoboken, NJ, USA, 1999.

[69] W. Jakob, J. Rhinelander, and D. Moldovan. pybind11 – seamless operability between C++11 and Python, 2017. https://github.com/pybind/pybind11. Accessed 4 Mar. 2024.

[70] J.-M. Jin and V. Liepa. Application of hybrid finite element method to electromagnetic scattering from coated cylinders. *IEEE Transactions on Antennas and Propagation*, **36**(1), pp. 50–54, 1988.

[71] J.-M. Jin. *Theory and Computation of Electromagnetic Fields*. John Wiley & Sons, Ltd, Hoboken, NJ, USA, 2010.

[72] J.-M. Jin. *The finite element method in electromagnetics*. John Wiley & Sons, 2015.

[73] S. Kailasa and T. Betcke. AdaptOctree: Adaptive linear octrees in Python, 2021. https://github.com/Excalibur-SLE/AdaptOctree. Accessed 4 Mar. 2024.

[74] S. Kharkovsky and R. Zoughi. Microwave and millimeter wave nondestructive testing and evaluation - overview and recent advances. *IEEE Instrumentation Measurement Magazine*, **10**(2), pp. 26–38, 2007.

[75] M. A. Khayat, D. R. Wilton, and P. W. Fink. An improved transformation and optimized sampling scheme for the numerical evaluation of singular and near-singular potentials. *IEEE Antennas and Wireless Propagation Letters*, **7**, pp. 377–380, 2008.

[76] P.-S. Kildal and A. Kishk. EM modeling of surfaces with stop or go characteristics – artificial magnetic conductors and soft and hard surfaces. *Applied Computational Electromagnetics Society Journal*, **18**(1), pp. 32–40, 2003.

[77] W. R. Klein and B. D. Cook. Unified approach to ultrasonic light diffraction. *IEEE Transactions on Sonics and Ultrasonics*, **14**(3), pp. 123–134, 1967.

[78] E. F. Knott, J. F. Shaeffer, and M. T. Tuley. *Radar Cross Section*. SciTech Publishing, Inc., Raleigh, NC, USA, 2nd edition, 2004.

[79] A. Korpel. *Acousto-optics*. Optical engineering, 16. Marcel Dekker Inc, New York, NY, USA, 1st edition, 1988.

[80] G. Kristensson. *Scattering of electromagnetic waves by obstacles*. SciTech, Edison, NJ, USA, 2016.

[81] S. K. Lam, A. Pitrou, and S. Seibert. Numba: A LLVM-based Python JIT compiler. In *Proceedings of the Second Workshop on the LLVM Compiler Infrastructure in HPC*, LLVM '15, New York, NY, USA, 2015. Association for Computing Machinery.

[82] B. Lau, M. Capek, and A. M. Hassan. Characteristic modes: Progress, overview, and emerging topics. *IEEE Antennas and Propagation Magazine*, **64**(2), pp. 14–22, 2022.

[83] X. S. Li. An overview of SuperLU: Algorithms, implementation, and user interface. *ACM Transactions on Mathematical Software*, **31**(3), pp. 302–325, 2005.

[84] A. Logg, K. B. Ølgaard, M. Rognes, G. N. Wells, and M. S. Alnæs. FFCx: Next generation FEniCS form compiler, 2023. https://github.com/FEniCS/ffcx. Accessed 4 Mar. 2024.

[85] J. Lundgren, K. Schab, M. Capek, M. Gustafsson, and L. Jelinek. Iterative calculation of characteristic modes using arbitrary full-wave solvers. *IEEE Antennas and Wireless Propagation Letters*, **22**(4), pp. 799–803, 2023.

[86] S. N. Makarov. *Antenna and EM Modeling with MATLAB*. John Wiley and Sons, Inc., New York, NY, USA, 2002.

[87] Y. Mao, Y. Zhong, Q. Zhan, D. Wang, and Q. H. Liu. A simple way of applying the Calderón preconditioner to a finite-element boundary-integral method. *IEEE Transactions on Antennas and Propagation*, **71**(6), pp. 5510–5515, 2023.

[88] J. M. Marshall, A. M. Peterson, and A. A. Barnes. Combined radar-acoustic sounding system. *Applied Optics*, **11**(1), pp. 108–112, 1972.

[89] P. T. May, R. G. Strauch, K. P. Moran, and W. L. Ecklund. Temperature sounding by RASS with wind profiler radars: a preliminary study. *IEEE Transactions on Geoscience and Remote Sensing*, **28**(1), pp. 19–28, 1990.

[90] B. McDonald and A. Wexler. Finite-element solution of unbounded field problems. *IEEE Transactions on Microwave Theory and Techniques*, **20**(12), pp. 841–847, 1972.

[91] D. Meagher. Geometric modeling using octree encoding. *Computer Graphics and Image Processing*, **19**(2), pp. 129–147, 1982.

[92] K. Mei. Unimoment method of solving antenna and scattering problems. *IEEE Transactions on Antennas and Propagation*, **22**(6), pp. 760–766, 1974.

[93] E. Michielssen and A. Boag. A multilevel matrix decomposition algorithm for analyzing scattering from large structures. *IEEE Transactions on Antennas and Propagation*, **44**(8), pp. 1086–1093, 1996.

[94] G. Mie. Beiträge zur optik trüber medien, speziell kolloidaler metallösungen. *Annalen der Physik*, **330**(3), pp. 377–445, 1908.

[95] C. G. Montgomery, R. H. Dicke, and E. M. Purcell. *Principles of Microwave Circuits*. McGraw-Hill, New York, United States, 1948.

[96] M. Morgan and K. Mei. Finite-element computation of scattering by inhomogeneous penetrable bodies of revolution. *IEEE Transactions on Antennas and Propagation*, **27**(2), pp. 202–214, 1979.

[97] M. Morgan, C. Chen, S. Hill, and P. Barber. Finite element-boundary integral formulation for electromagnetic scattering. *Wave Motion*, **6**(1), pp. 91–103, 1984.

[98] N. K. Nikolova. *Introduction to Microwave Imaging*. EuMA High Frequency Technologies Series. Cambridge University Press, 2017.

[99] T. E. Oliphant. Python for scientific computing. *Computing in Science & Engineering*, **9**(3), pp. 10–20, 2007.

[100] Open Source Initiative. The 3-clause BSD license. https://opensource.org/license/bsd-3-clause/. Accessed 1 Feb. 2024.

[101] S. J. Orfanidis. *Diffraction – Plane-Wave Spectrum*, chapter 19, pp. 844 – 922. Electromagnetic Waves and Antennas. Rutgers University, 2016.

[102] K. Paulsen, D. Lynch, and J. Strahbehn. Three-dimensional finite, boundary, and hybrid element solutions of the maxwell equations for lossy dielectric media. *IEEE Transactions on Microwave Theory and Techniques*, **36**(4), pp. 682–693, 1988.

[103] K. Persson, M. Gustafsson, G. Kristensson, and B. Widenberg. Radome diagnostics—source reconstruction of phase objects with an equivalent currents approach. *IEEE Transactions on Antennas and Propagation*, **62**(4), pp. 2041–2051, 2014.

[104] T. Peters and J. Volakis. Application of a conjugate gradient FFT method to scattering from thin planar material plates. *IEEE Transactions on Antennas and Propagation*, **36**(4), pp. 518–526, 1988.

[105] A. G. Polimeridis and J. R. Mosig. Complete semi-analytical treatment of weakly singular integrals on planar triangles via the direct evaluation method. *International Journal for Numerical Methods in Engineering*, **83**(12), pp. 1625–1650, 2010.

[106] A. G. Polimeridis and J. R. Mosig. On the direct evaluation of surface integral equation impedance matrix elements involving point singularities. *IEEE Antennas and Wireless Propagation Letters*, **10**, pp. 599–602, 2011.

[107] A. G. Polimeridis, J. M. Tamayo, J. M. Rius, and J. R. Mosig. Fast and accurate computation of hypersingular integrals in Galerkin surface integral equation formulations via the direct evaluation method. *IEEE Transactions on Antennas and Propagation*, **59**(6), pp. 2329–2340, 2011.

[108] A. G. Polimeridis, F. Vipiana, J. R. Mosig, and D. R. Wilton. DIRECTFN: Fully numerical algorithms for high precision computation of singular integrals in Galerkin SIE methods. *IEEE Transactions on Antennas and Propagation*, **61**(6), pp. 3112–3122, 2013.

[109] A. G. Polimeridis and T. V. Yioultsis. On the direct evaluation of weakly singular integrals in Galerkin mixed potential integral equation formulations. *IEEE Transactions on Antennas and Propagation*, **56**(9), pp. 3011–3019, 2008.

[110] D. M. Pozar. *Microwave Engineering*. John Wiley & Sons, Inc., 3rd edition, 2005.

[111] J. L. A. Quijano and G. Vecchi. Field and source equivalence in source reconstruction on 3D surfaces. *Progress In Electromagnetics Research*, **103**, pp. 67–100, 2010.

[126] M. W. Scroggs, I. A. Baratta, C. N. Richardson, and G. N. Wells. Basix: a runtime finite element basis evaluation library. *Journal of Open Source Software*, **7**(73), pp. 3982, 2022.

[127] M. W. Scroggs, J. S. Dokken, C. N. Richardson, and G. N. Wells. Construction of arbitrary order finite element degree-of-freedom maps on polygonal and polyhedral cell meshes. *ACM Transactions on Mathematical Software*, **48**(2), 2022.

[128] M. W. Scroggs et al. DefElement: an encyclopedia of finite element definitions, 2024. https://defelement.com. Accessed 5 Jan. 2024.

[129] C. E. Shannon. A mathematical theory of communication. *The Bell System Technical Journal*, **27**(3), pp. 379–423, 1948.

[130] X.-Q. Sheng, J.-M. Jin, J. Song, C.-C. Lu, and W. C. Chew. On the formulation of hybrid finite-element and boundary-integral methods for 3-D scattering. *IEEE Transactions on Antennas and Propagation*, **46**(3), pp. 303–311, 1998.

[131] P. J. Shull. *Nondestructive evaluation: theory, techniques, and applications.* CRC press, Boca Raton, FL, USA, 2002.

[132] D. Sievenpiper, L. Zhang, R. Broas, N. Alexopolous, and E. Yablonovitch. High-impedance electromagnetic surfaces with a forbidden frequency band. *IEEE Transactions on Microwave Theory and Techniques*, **47**(11), pp. 2059–2074, 1999.

[133] P. Silvester and M.-S. Hsieh. Finite-element solution of 2-dimensional exterior-field problems. *Proceedings of the Institution of Electrical Engineers*, **118**(12), pp. 1743–1747, 1971.

[134] A. Sommerfeld. *Partial Differential Equations in Physics.* Academic Press, New York, NY, USA, 1949.

[135] J. Song, C.-C. Lu, and W. C. Chew. Multilevel fast multipole algorithm for electromagnetic scattering by large complex objects. *IEEE Transactions on Antennas and Propagation*, **45**(10), pp. 1488–1493, 1997.

[136] J. M. Song and W. C. Chew. Multilevel fast-multipole algorithm for solving combined field integral equations of electromagnetic scattering. *Microwave and Optical Technology Letters*, **10**(1), pp. 14–19, 1995.

[137] D. L. Sounas and A. Alù. Non-reciprocal photonics based on time modulation. *Nature Photonics*, **11**(12), pp. 774–783, 2017.

[138] R. Stallman. The GNU general public license v3.0, 2007. https://www.gnu.org/licenses/gpl-3.0.html. Accessed 1 Feb. 2024.

[139] R. H. Stolt. Migration by Fourier transform. *Geophysics*, **43**(1), pp. 23–48, 1978.

[140] Texas Instruments. mmWave radar sensors. https://www.ti.com/sensors/mmwave-radar/overview.html. Accessed 7 Feb. 2024.

[141] The Institute of Electrical and Electronics Engineers, Inc. IEEE standard for radar definitions. *IEEE Std 686-2017 (Revision of IEEE Std 686-2008)*, p. 33, 2017.

[142] The MathWorks, Inc. MATLAB performance - MATLAB & Simulink. https://www.mathworks.com/products/matlab/performance.html. Accessed 7 Feb. 2024.

[143] E. Tiesinga, P. J. Mohr, D. B. Newell, and B. N. Taylor. CODATA recommended values of the fundamental physical constants: 2018. *Journal of Physical and Chemical Reference Data*, **50**(3), pp. 033105, 09 2021.

[144] L. N. Trefethen and D. Bau. *Numerical Linear Algebra*. Society for Industrial and Applied Mathematics, Philadelphia, PA, 1997.

[145] J. Van Bladel. Electromagnetic fields in the presence of rotating bodies. *Proceedings of the IEEE*, **64**(3), pp. 301–318, 1976.

[146] J. Van Bladel. *Singular electromagnetic fields and sources*. Clarendon Press, Oxford, UK, 1991.

[147] J. G. Van Bladel. *Electromagnetic Fields*. John Wiley & Sons, Hoboken, NJ, USA, 2007.

[148] E. van den Berg and M. P. Friedlander. Probing the Pareto frontier for basis pursuit solutions. *SIAM Journal on Scientific Computing*, **31**(2), pp. 890–912, 2008.

[149] E. van den Berg and M. P. Friedlander. SPGL1: A solver for large-scale sparse reconstruction, 2019. https://friedlander.io/spgl1. Accessed 3 Mar. 2024.

[150] F. Vipiana, D. R. Wilton, and W. A. Johnson. Advanced numerical schemes for the accurate evaluation of 4-D reaction integrals in the method of moments. *IEEE Transactions on Antennas and Propagation*, **61**(11), pp. 5559–5566, 2013.

[151] C. R. Vogel. *Computational Methods for Inverse Problems*. Society for Industrial and Applied Mathematics, Philadelphia, PA, USA, 2002.

[152] J. L. Volakis and K. Sertel. *Integral equation methods for electromagnetics*. SciTech Publishing, Raleigh, NC, USA., 2012.

[153] J. L. Volakis, M. Shields, G. Manara, S. R. Rengarajan, and Y. Hao. *100 Years of the International Union of Radio Science*, chapter 28: URSI Commission B Centennial History Contribution, pp. 411–436. URSI Press, Gent, Belgium, 2021.

[154] M. N. Vouvakis, Seung-Cheol Lee, Kezhong Zhao, and Jin-Fa Lee. A symmetric FEM-IE formulation with a single-level IE-QR algorithm for solving electromagnetic radiation and scattering problems. *IEEE Transactions on Antennas and Propagation*, **52**(11), pp. 3060–3070, 2004.

[155] C. Waldschmidt, J. Hasch, and W. Menzel. Automotive radar — from first efforts to future systems. *IEEE Journal of Microwaves*, **1**(1), pp. 135–148, 2021.

[156] T. Wan, M. Z. Li, and L. F. Li. Direct solution of finite element-boundary integral system for electromagnetic analysis in half-space. *IEEE Transactions on Antennas and Propagation*, **68**(8), pp. 6461–6466, 2020.

[157] N. Wingren. Acousto-electromagnetic interaction in materials for aerospace composites. M.s. thesis, Dept. of Elect. and Inform. Technol., Lund Univ., Lund, Sweden, 2019.

[158] A. Yaghjian. Approximate formulas for the far field and gain of open-ended rectangular waveguide. *IEEE Transactions on Antennas and Propagation*, **32**(4), pp. 378–384, 1984.

[159] A. Yaghjian. An overview of near-field antenna measurements. *IEEE Transactions on Antennas and Propagation*, **34**(1), pp. 30–45, 1986.

[160] M. Yang, B. Wu, H. Gao, and X. Sheng. An effective $\mathcal{H}$-LU-based preconditioner for the FE-BI-MLFMA for 3-D scattering problems. *IEEE Antennas and Wireless Propagation Letters*, **18**(12), pp. 2766–2770, 2019.

[161] X. Yang, M. Jiang, L. Shen, P.-H. Jia, Z. Rong, Y. Chen, L. Lei, and J. Hu. A flexible FEM-BEM-DDM for EM scattering by multiscale anisotropic objects. *IEEE Transactions on Antennas and Propagation*, **69**(12), pp. 8562–8573, 2021.

[162] Z. Yang, X.-W. Yuan, X.-W. Huang, M.-L. Yang, and X.-Q. Sheng. Resistive sheet boundary condition-based nonconformal domain decomposition FE-BI-MLFMA for electromagnetic scattering from inhomogeneous objects with honeycomb structures. *IEEE Transactions on Antennas and Propagation*, **70**(10), pp. 9483–9496, 2022.

[163] P. Ylä-Oijala, S. P. Kiminki, K. Cools, F. P. Andriulli, and S. Järvenpää. Mixed discretization schemes for electromagnetic surface integral equations. *International Journal of Numerical Modelling: Electronic Networks, Devices and Fields*, **25**(5-6), pp. 525–540, 2012.

[164] S. Yrjölä, M. Matinmikko-Blue, and P. Ahokangas. *The Changing World of Mobile Communications*, chapter 2: The Evolution of Mobile Communications, pp. 13–44. Palgrave Macmillan, Cham, Switzerland, 2024.

[165] X. Yuan. Three-dimensional electromagnetic scattering from inhomogeneous objects by the hybrid moment and finite element method. *IEEE Transactions on Microwave Theory and Techniques*, **38**(8), pp. 1053–1058, 1990.

[166] X. Yuan, D. Lynch, and J. Strohbehn. Coupling of finite element and moment methods for electromagnetic scattering from inhomogeneous objects. *IEEE Transactions on Antennas and Propagation*, **38**(3), pp. 386–393, 1990.

[167] K. Zhao, M. Vouvakis, and J.-F. Lee. The adaptive cross approximation algorithm for accelerated method of moments computations of EMC problems. *IEEE Transactions on Electromagnetic Compatibility*, **47**(4), pp. 763–773, 2005.

[168] R. Zoughi. *Microwave Non-Destructive Testing and Evaluation*. Kluwer academic publishers, Dordrecht, The Netherlands, 2000.

[169] P. Zwamborn and P. M. van den Berg. Computation of electromagnetic fields inside strongly inhomogeneous objects by the weak-conjugate-gradient fast-Fourier-transform method. *Journal of the Optical Society of America A*, **11**(4), pp. 1414–1421, 1994.